TRIBOLOGICAL BEHAVIOR AND GAS-SURFACE INTERACTIONS OF HYDROGENATED CARBON FILMS

By

PAMELA LAURIE DICKRELL

A DISSERTATION PRESENTED TO THE GRADUATE SCHOOL
OF THE UNIVERSITY OF FLORIDA IN PARTIAL FULFILLMENT
OF THE REQUIREMENTS FOR THE DEGREE OF
DOCTOR OF PHILOSOPHY

UNIVERSITY OF FLORIDA

2005

Copyright 2005

by

Pamela Laurie Dickrell

This work is dedicated to Miss Sara Gabrielle Nannis for reminding me what is most important in life.

ACKNOWLEDGMENTS

This body of work has been completed with as much support and effort from people in my life as it has by my time with a pen and paper.

The first and foremost acknowledgement goes to my husband Dan. I thank him for always supporting that, while formally educated in science, 99% of my decisions in life are made with a blatant disregard to logic and are solely based on my heart. While he does not always understand why I do things, he has never kept me from being who I am or reaching for my goals. This girl could never ask for anything more. He may never know how to make a pie, but he has learned how to duck faster and laugh out loud when frustrated Sicilian women throw stuff across the house. I could not, would not, have written this without my best friend Dan. **Rock!**

My mom deserves all the credit for raising me. She never kept us from being who we were by both promoting and joining in the silliness of being kids. I have to thank her for giving so much to me and Monica by not showering us with things but rather by teaching us how to live. I know I would not have made it in school and life without her teaching me how to take care of myself. She has always encouraged me to think freely and argue my points, even when I was wrong. It was better to scrape my knee than to have my hand held, the scratches and bruises have built character along the way.

My sister Monica deserves thanks for being my voice all those times I was too shy to speak. I am grateful to have had her as my partner in crime growing up; our

adventures together are the most memorable events of childhood. My experiences with her have made me who I am today and I am looking forward to watching our families grow together. She has always been there for me and I will always do the same, no questions asked.

I thank my grandma for all the prayers and for passing on her happiness and love for life to the family. She has never hesitated to laugh out loud or do silly things to make us smile. The wagon wheel tradition will always remain strong.

Miss Sara Gabrielle Nannis deserves thanks for reminding me what is most important in life.

Katie and Daisy, I thank them for the four ears that have been open twenty-four hours a day to listen; man's best friends indeed.

There are a few friends whose both personal and professional support has made this work possible. I am grateful for the help of Jason Action, Dr. Thierry Blanchet (lab grandpa), Jerry Bourne, Dave (the oil can) Burris, Matthew Hamilton, Alison Rennie (Dunn), Dr. Irwin Singer, and Jason Steffens.

I appreciate the constructive input and words of wisdom both professionally and personally from the members of my committee: Dr. David Hahn, Dr. Tony Schmitz, Dr. John Ziegert, and Dr. Paul Holloway.

Particular thanks go to Dr. Ali Erdemir for all of his help in this work. The scope of this thesis would not have been possible without his ingenuity and research. The summer working together and the many conversations along the way have greatly shaped my professional and personal character.

Finally, recognition and gratitude goes out to my friend (first) and advisor (second), Wallace Gregory Sawyer. Thoughts: irrational impatience may actually work. Concerns: never write a book. Gripes: eat something, coffee and diet cokes do not a meal make. Grievances: do you actually think it would be more fun had I been a "yes" man? Professionally, I thank him for the fishing lessons, I shouldn't go hungry. Personally, I thank him for both the adventures and kicks in the ass when I needed each of them the most.

TABLE OF CONTENTS

page

ACKNOWLEDGMENTS iv

LIST OF TABLES x

LIST OF FIGURES xi

ABSTRACT xiv

CHAPTER

1 NEAR FRICTIONLESS CARBON (NFC): HYDROGENATED DIAMOND-LIKE CARBON 1

1.1 Introduction 1
1.2 Material Properties 3
1.3 Investigation Goals 5

2 GAS-SURFACE MODELING IN TRIBOLOGICAL CONTACTS 6

2.1 Tribological Configurations 6
2.2 Pin-on-Disk/Midpoint Reciprocation Modeling 7
2.3 Positional Reciprocation Model 13
2.4 Linear Rule of Mixtures 20

3 FRICTION MODELING AND DATA COMPARISON 22

3.1 Near Frictionless Carbon Self-Mated Experiments 22
3.2 Pin-on-Disk / Reciprocation Midpoint Model Fit 24
3.3 Positional Reciprocation Model Fit 28

4 MICRO-TRIBOMETER: EXPERIMENTAL APPARATUS AND UNCERTAINTY 33

4.1 Reciprocating Pin-on-Disk Microtribometer 33
4.2 Microtribometer Friction Coefficient Values 39
4.3 Propagation of Uncertainty in the Friction Coefficient 48
4.3.1 Law of Propagation of Uncertainty 48
4.3.2 μ: Friction Coefficient 51

4.3.3 Friction Coefficient Expansion....52
4.3.3.1 ϕ: Pitch misalignment angle....52
4.3.3.2 μ_f': Tribometer reported friction coefficient....53
4.3.3.3 β: Roll misalignment angle....53
4.3.4 Tribometer Read Forces....54
4.3.4.1 F_V: Tribometer read vertical force....54
4.3.4.2 F_{Hf}: Tribometer read forward sliding horizontal force....55
4.3.4.3 F_{Hr}: Tribometer read reverse sliding horizontal force....56
4.3.5 Force Expansion....57
4.3.5.1 V: Optical sensor voltage....57
4.3.5.2 C: Displacement – Voltage calibration constant....57
4.3.5.3 d, G: Mounting offset error and calibration slope constant....58
4.3.5.4 K: Flexure stiffness....61
4.3.6 Stiffness Expansion....62
4.3.6.1 Mg: Calibration force....62
4.3.6.2 δ: Calibration displacement....62

5 INITIAL ENVIRONMENTAL TRIBOLOGY OF NFC FILMS....68

5.1 Near Frictionless Carbon Run-In Testing....69
5.2 Sample Pair and Humidity Variation Experiments....72
5.3 Water Vapor Ramp....75

6 WATER VAPOR PRESSURE AND SUBSTRATE TEMPERATURE EFFECTS .78

6.1 Water Vapor and Surface Temperature Experiments....78
6.2 Gas-Surface Modeling: Adsorption and Desorption Rates....84

7 CONCLUDING REMARKS....91

APPENDIX

A LANGMUIR MODEL DERIVATION....93

B HENRY'S LAW....95

C ELOVICH EQUATION....97

D LINEAR APPEARANCE OF CURVES....100

E INFLUENCE OF PITCH ANGLE ON UNCERTAINTY....102

F RUN-IN BOND ENERGY....104

G PRELIMINARY LOW CONTACT PRESSURE EXPERIMENTS....106

H NFC-NFC DRY ARGON....108

I GLASS-NFC DRY ARGON 113

J NFC-NFC HUMID ARGON 118

K LANGMUIR ADSORPTION AND DESORPTION INTEGRATION 122

LIST OF REFERENCES 123

BIOGRAPHICAL SKETCH 126

LIST OF TABLES

Table		page
2-1	Recursive model parameters	7
2-2	Fractional coverage expressions	10
2-3	Difference in coverage expressions	10
2-4	Positional fractional coverage expressions	16
2-5	Positional difference in coverage expressions	17
2-6	Positional model variable definitions	18
4-1	Nomenclature for microtribometer measurement analysis	40
4-2	Measured values used in the calculation of uncertainty	50
4-3	Uncertainty in measured values.	51
6-1	Gas-surface modeling nomenclature	85

LIST OF FIGURES

Figure page

1-1 View into NFC magnetron deposition chamber and TEM cross section view of deposited NFC coating 3

1-2 Outline of compositions of bulk NFC films and the interface between self-mated NFC coatings in a tribological contact 5

2-1 Rotating pin-on-disk configuration for tribological testing 8

2-2 Reciprocating pin-on-flat configuration for tribological testing. 14

2-3 Positional reciprocation schematic 15

2-4 Pin-on-disk and reciprocating model comparison. 21

3-1 NFC self mated dry nitrogen data 24

3-2 a) Pin-on-disk/reciprocating midpoint model (eqn 2.11) fit to average Heimberg et al. data (Figure 3-1). b) Fraction removed (1-λ) parameter as a function of sliding speed for model fit. 25

3-3 a) Pin-on-disk/reciprocating midpoint model (eqn 2.11) fit to constant velocity/dwell data. b) Fraction removed (1-λ) parameter as a function of dwell time for model fit. 26

3-4 Positional model comparisons to friction coefficient data for a) cycle 19/20 at multiple sliding speeds. b) data from multiple cycles at a 30 μm/s sliding speed ...28

3-5 Removal ratio as a function of friction coefficient 31

4-1 Environmental control, contact region and operational parameters of microtribometer. 33

4-2 Gaseous environment and counterface surface temperature control 35

4-3 Schematic of tribometer test assembly and manufacturer defined axes of motion ..36

4-4 Example of positional data collected from CSM nanotribometer for a reciprocating test on vertically aligned nanotubes showing the loop of friction coefficient or frictional force versus wear track position. 38

4-5 Potential misalignment angles in positioning counterface stub into reciprocating stage....41

4-6 The effect of the misalignment angle β on the ratio of the tribometer reported forward and reverse friction coefficient values....46

4-7 Equation derived frictional loop for pin and counterface pair with friction coefficient μ=0.12 and misalignment roll angle β=5°....47

4-8 Propagation of uncertainty hierarchy....50

4-9 Operating ranges and calibration curves for optical sensors....58

4-10 Schematic analysis to find the mounting offset error ($d_{V,H}$) and slope constant ($G_{V,H}$)....59

4-11 Lines of constant uncertainty in the friction coefficient....64

4-12 Lines of constant uncertainty in friction coefficient over the friction coefficient....65

4-13 Relative contributions to the variance in the friction coefficient....66

5-1 Surface scans of uncoated pin sample and coated flat sample....68

5-2 Initial run-in of two unworn self-mated NFC samples in a dry argon environment....69

5-3 Environment exposure dwell experiments....71

5-4 Test conditions for the three matrix series....73

5-5 Surface scans of pin samples after a) self mated NFC tests in dry argon, b) glass pin against a NFC coated counterface in dry argon, and c) self mated NFC tests in humid argon....74

5-6 Variation of friction coefficient of self mated NFC pair to a prescribed change in relative humidity of an argon environment....76

6-1 Experimental matrix for variations of chamber vapor pressure and NFC temperature....79

6-2 Steady state friction coefficient values as a function of counterface surface temperature for a) 123 Pa, b) 1233 Pa, c) 2837 Pa and d) 4933 Pa of water vapor pressure....80

6-3 Counterface roll angle β as a function of surface temperature for the experiments from Figure 6-2....83

6-4 Experimental results of friction coefficient (μ) and surface coverage (θ) as a function of counterface surface temperature and water vapor pressure. 84

6-5 Model fit of eqn 6.4 to experimental data with a) a universally fit value for τ_0 and E_a, and b) a universally fit value of τ_0 and a variable fit of E_a. 88

6-6 Model fit of eqn 6.4 to experimental data with a set value of τ_0=1E-13 sec for a) a universally fit value of E_a, and b) a variable fit of E_a. 89

Abstract of Dissertation Presented to the Graduate School
of the University of Florida in Partial Fulfillment of the
Requirements for the Degree of Doctor of Philosophy

TRIBOLOGICAL BEHAVIOR AND GAS-SURFACE INTERACTIONS OF HYDROGENATED CARBON FILMS

By

Pamela Laurie Dickrell

August 2005

Chair: Wallace Gregory Sawyer
Major Department: Mechanical and Aerospace Engineering

Diamond-like carbon films are used as tribological coatings for surfaces of devices that see relative motion. One class of highly hydrogenated diamond-like carbon coatings, termed near frictionless carbon (NFC), have experimentally shown extremely low friction coefficients and wear rates when used in a dry or inert environment. The tribological properties of NFC films are influenced by the surrounding environment and this is thought to be due to gaseous species interaction on the NFC coating surfaces.

This body of work develops models of gas-surface interactions in tribological contacts. Model predictions of friction coefficient are compared to experimental data from self mated NFC contacts to investigate if frictional trends are due to balancing rates of surface adsorption and removal of environmental species. An uncertainty analysis is performed on the low contact pressure tribometer used for environmental testing of the NFC films. Tribological experiments with variations in normal load, sliding speed, track length, environmental water vapor concentration and counterface temperature are run on

NFC films using the low contact pressure tribometer. Gas surface adsorption and desorption modeling is used to examine frictional trends seen with imposed variations in water vapor pressure and temperature. This modeling is used to confirm surface adsorption and removal of water vapor as contributing factors to the environmental performance of NFC films as solid lubricant coatings.

CHAPTER 1
NEAR FRICTIONLESS CARBON (NFC): HYDROGENATED DIAMOND-LIKE CARBON

1.1. Introduction

Diamond-like carbon (DLC) films are of tribological interest due to their low friction, low wear rate, high hardness, and chemical inertness [1, 2]. These films can potentially be used in a wide range of applications, such as bearings, cutting tools, submersible parts, and biomedical applications [3-6]. One class of diamond-like carbon coatings termed near frictionless carbon (NFC) that was developed at Argonne National Laboratory has been shown to sustain superlow coefficients of friction (μ <0.003) and wear rates (K <3^{-10} mm^3/Nm) in self-mated contacts [3]. The tribological behavior of these films is sensitive to the environment, only realizing their low coefficient of friction and wear rate in inert, dry, or vacuum environments [3, 7-10]. It would be useful to understand in what functional environmental regimes the low friction and wear characteristics of NFC films were realized. In addition, it would be beneficial to understand why NFC films have different tribological characteristics in various environments. This information would allow the pool of potential applications for these coatings to be narrowed and specific useful applications for NFC to be realized.

Because NFC films have different tribological characteristics in various environments, it has been theorized that gas-surface interactions between the NFC coating and environmental species are the cause for variation in the friction coefficient

and wear rate of the films [8-10]. Environment/surface interaction models have been created by other research groups in an attempt to describe friction coefficient variations in tribological experiments. To the author's knowledge, the first modeling of this in tribology is the work of Rowe [11], who used the Langmuir adsorption model [12] to describe the wear in boundary lubrication. Gas/surface interactions were reported in 1957 by Bowden and Rowe [13] to describe the lubrication of molybdenum in hydrogen disulfide gases, but were not modeled. Blanchet and Sawyer [14] included both deposition and removal rates in a model developed to study transitions from adequate to inadequate lubrication in vapor phase lubrication; this model was based on balancing the rates of layer formation and removal but was not fractional (friction was predicted to be either low or high in the adequate or inadequate regime respectively). A time-dependent fractional coverage model, without removal, was proposed by Zaidi *et al.* [15] to describe gas interactions with carbon surfaces. The interaction kinetics used followed the work of Elovich [16]. Models that predict steady-state friction coefficients for pin-on-disk contacts and combined rolling and sliding contacts [17] were developed by applying the competitive rate model of Blanchet *et al.* [18] with Langmuir fractional surface adsorption [12] and fractional removal [19].

Some testing on the gas-surface interactions of NFC films has already been performed. Heimberg *et al.* [9] hypothesized that velocity dependence of the friction coefficients of NFC films was due to a gas-surface interaction that had longer times to affect the film at slower sliding speeds. This hypothesis was further supported by experiments that varied exposure time under constant sliding speeds using periods of dwell at the reversal locations. These tests showed a clear dependence on exposure time

as opposed to velocity. In addition, Heimberg et al. modeled the transient portion of gas-surface interactions using an Elovich model for adsorption, but did not achieve steady state modeling for friction coefficient [9].

1.2. Material Properties

Near frictionless carbon films are a thin film, amorphous type of diamond-like-carbon, composed of a mix of carbon and hydrogen. They are made by a room temperature plasma-enhanced chemical vapor deposition process, performed in a magnetron sputtering system [20]. A target substrate material is sputter cleaned in an Ar plasma for 30 minutes by applying a 1200-1700 V bias [3,20]. Next, a 50-70 nm thick Si bond layer is applied by sputter coating from a Si target [3,20]. Then mixes of CH_4, C_2H_2, C_2H_4, or C_2H_6, and H_2 gases are introduced into the deposition chamber, depending on the desired ratio of H:C in the film [7]. The specific NFC films investigated in this study use 25% CH_4 and 75% H_2 for chamber flow ratios during coating. This results in a film that is approximately 60% carbon and 40% hydrogen atomically. The final films are 1-1.5 μm thick [8].

images courtesy of Dr. Ali Erdemir, Argonne National Laboratory

Figure 1-1 View into NFC magnetron deposition chamber and TEM cross section view of deposited NFC coating.

Indentation tests were performed by other researchers using a Vickers indentation on a Fisherscope H100 dynamic micro-hardness tester with a maximum load of 4.2 mN [3]. In over 30 indentation tests the film was found to have a hardness of 7.66 GPa and elastic modulus of 47.2 GPa. It was also found that as the hydrogen content of the films increase, both the hardness and modulus decrease [3]. In addition, in self mated pin-on-disk tests in a dry nitrogen environment it was found as the hydrogen content of the NFC films increased the steady state friction and wear rate decreased [3]. Raman spectroscopy has been used to determine these NFC films are approximately 60% sp^3 in composition, with most of the sp^3 bonds being hydrogen terminated [21].

It has been proposed that since NFC films are chemically inert they exact very little adhesive force while sliding against other materials [7]. The films used in this study have high hydrogen content and it has been theorized that free hydrogen in these films can terminate carbon bonds at the surface [8]. Hydrogen may attach to and passivate dangling surface bonds of carbon atoms in such materials and reduce the friction coefficient; when the hydrogen is removed the dangling carbon bonds are reactivated and friction coefficient rises [7]. It has also been proposed that in a self mated NFC pair, the hydrogen terminated surfaces slide freely across one another in an inert environment [8]. When a gaseous species is added to the environment the friction coefficient in NFC self-mated contacts rises [10], suggesting a gas-surface interaction where environmental species may disrupt the hydrogen termination of the NFC pair and lead to a rise in friction coefficient. In contrast, hydrogen-free diamond-like carbon films show lower friction coefficients in humid air than in inert or vacuum conditions [22], further

suggesting this hydrogen at the surface plays a strong role in the frictional performance of self-mated NFC films.

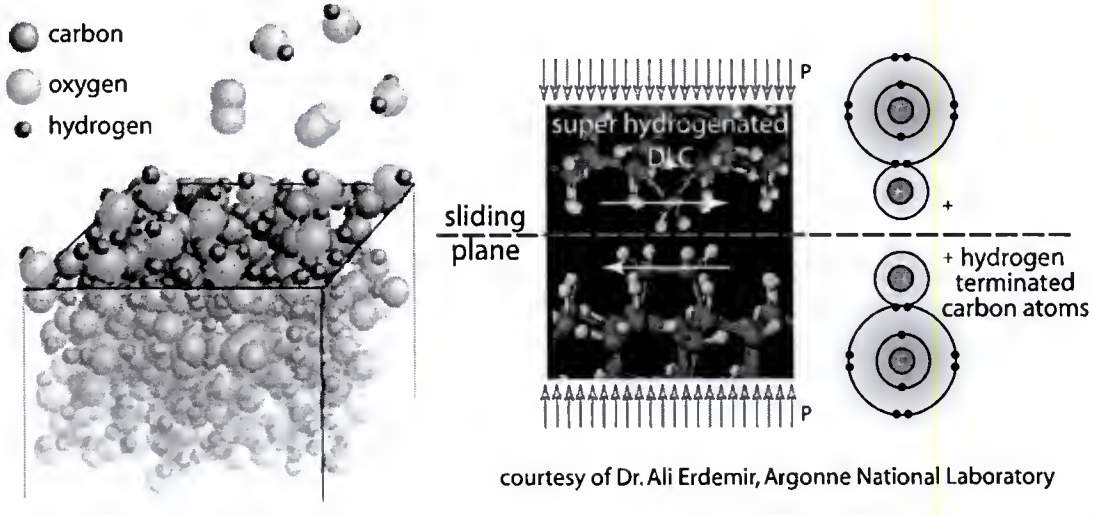

Figure 1-2 Outline of compositions of bulk NFC films and the interface between self-mated NFC coatings in a tribological contact.

1.3. Investigation Goals

This body of work aims to:

1) Develop closed form models for surface coverage in tribological contacts based on competitive rates of gas-surface adsorption and periodic adsorbate removal through the tribological contact. (Chapter 2)
2) Use developed surface-coverage modeling to make predictive statements of transient and steady state frictional performance and compare these predictions to other investigators' experimental friction results on NFC films. (Chapter 3)
3) Perform an uncertainty analysis on a commercially available low contact pressure tribometer used in this study for NFC frictional testing. (Chapter 4)
4) Execute a series of tribological experiments on NFC films using the low contact pressure tribometer to look at the environmental dependence of the frictional performance of NFC coatings, initial surface layers on the coatings, and isolate which environmental species is controlling the frictional performance of NFC. (Chapter 5)
5) Based on the results in Chapter 5 execute a series of experiments varying both concentrations of the isolated influential environmental species and substrate temperature to investigate frictional trends within combinations of these two parameters. The frictional trends seen in variations of species concentration and temperature will be modeled using a first-order gas surface model to further determine if surface adsorption and desoprtion is controlling friction coefficient trends in NFC films. (Chapter 6)

CHAPTER 2
GAS-SURFACE MODELING IN TRIBOLOGICAL CONTACTS

2.1. Tribological Configurations

Two common configurations for tribological testing of friction coefficient are the rotating pin on disk and reciprocating pin on flat contacts. In both of these there is a pin specimen that can be flat or radiused that is loaded against a (usually) flat counterface. There is relative motion between the pin and flat sample; in the pin on disk case, the disk is usually rotated and the pin held stationary to make a circular wear track path, and in the reciprocating case either the pin or flat is moved in a forward and reverse motion to make a linear wear track path. This work models the evolution of environmental species adsorption on a counterface during a tribological contact. The parameters that will be used in model derivation are listed in Table 2-1.

Table 2-1 Recursive model parameters.

α	adsorption fraction
subscript *c*	cycle
subscript *f*	forward direction
subscript *in*	entrance of pin contact
L	track length
λ	removal ratio $(\theta_{out}/\theta_{in})$
μ_1	friction coefficient of covered surface
μ_0	friction coefficient of nascent surface
n	cycle number
ν	deposition constant
subscript *out*	exit of of pin contact
P	partial pressure
$1-\theta$	nascent surface area fraction
θ	covered surface area fraction
subscript *r*	reverse direction
t	time between pin events
T	time since test inception
V	velocity

There are a few assumptions being used in the modeling for surface coverage and friction coefficient predictions. First, there is no surface wear taking place; instead there is a covering by environmental species and partial removal of this coverage through the pin contact. The coverage fraction (θ) remains between 0 (completely nascent surface) and 1 (fully covered surface). Modeling also assumes a constant sliding velocity.

2.2. Pin-on-Disk / Midpoint Reciprocation Model

A schematic of the rotating pin-on-disk configuration for surface species modeling is shown in Figure 2-1.

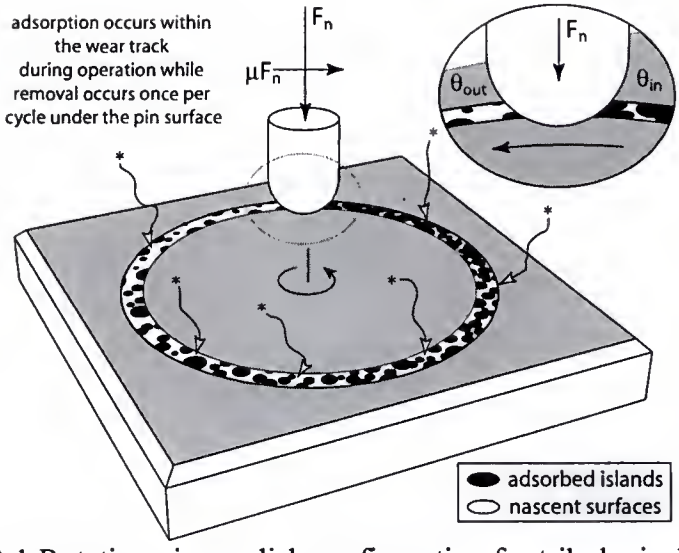

Figure 2-1 Rotating pin-on-disk configuration for tribological testing.

Modeling of the pin-on-disk configuration assumes some initial surface fractional coverage (θ_0) of an adsorbed species. At time equals zero, or the initiation of an experiment, this term is the fractional coverage that enters into the initial pin contact. The fractional coverage that then leaves the contact (θ_{out}) is assumed to be less than the entering fractional coverage for two reasons: 1) adsorption of gaseous species is assumed to be negligible under the pin contact, and 2) removal of adsorbed species is assumed to occur under the pin contact as a combination of mechanical removal and thermal desorption as a result of frictional heating. After the surface element leaves contact, it is exposed to the gaseous environment, and adsorption occurs on the nascent portion on the surface during the time it takes for the surface element to return to contact. The subsequent entering fractional coverage θ_{in} varies from cycle to cycle until the system reaches equilibrium.

The model addressed in the body of this investigation follows the works of Langmuir [12] and Blanchet and Sawyer [18] for the adsorption and removal of fractional films, respectively. Model equation derivation of the Langmuir expression is included in

Appendix A. There are other commonly used gas-surface adsorption models in the literature. The model derivation and fit to experimental data are performed and discussed in Appendix B and C for two other common gas-surface models: Henry's Law and the Elovich Model. For the body of this work, following Langmuir, the adsorption of a gas species occurs on the fraction of the surface that is not covered ($1 - \theta_{out}$) in the time from when the surface exits the pin contact to when it enters the pin contact on the next revolution. The adsorption ratio, α, is the fraction of the uncovered surface coming out of the pin contact that becomes covered by an adsorbed species between cycles. If the time between contacts, temperature, and gaseous environment remains constant, the adsorption ratio α will not change between cycles, although the fractional coverage will. Following Blanchet and Sawyer [18], the removal ratio (λ) is the ratio of the fraction of the surface covered at the exit of the pin contact to that at the entrance. This fractional removal of the adsorbed species occurs differentially through the pin contact and is ensured to be between 0 and 1. An expression for the average fractional coverage under the pin is used to make friction coefficient predictions. This model is recursive, and application of the equations gives a fractional coverage sequence for the first few cycles, as shown in table 2-2.

Table 2-2 Fractional coverage expressions.

θ_{0in}	$=\theta_0$	$=\theta_0$
θ_{0out}	$=\lambda\theta_0$	$=\lambda\theta_0$
θ_{1in}	$=\theta_{0out}+(1-\theta_{0out})\alpha$	$=\lambda\theta_0+\alpha-\lambda\alpha\theta_0$
θ_{1out}	$=\lambda\theta_{1in}$	$=\lambda(\lambda\theta_0+\alpha-\lambda\alpha\theta_0)$
θ_{2in}	$=\theta_{1out}+(1-\theta_{1out})\alpha$	$=\lambda^2\theta_0+\lambda\alpha-2\lambda^2\alpha\theta_0+\alpha-\lambda\alpha^2+\lambda^2\alpha^2\theta_0$
θ_{2out}	$=\lambda\theta_{2in}$	$=\lambda\left(\lambda^2\theta_0+\lambda\alpha-2\lambda^2\alpha\theta_0+\alpha-\lambda\alpha^2+\lambda^2\alpha^2\theta_0\right)$
θ_{3in}	$=\theta_{2out}+(1-\theta_{2out})\alpha$	$=\lambda^3\theta_0+\lambda^2\alpha-3\lambda^3\alpha\theta_0+\lambda\alpha-2\lambda^2\alpha^2+3\lambda^3\alpha^2\theta_0+\alpha-\lambda\alpha^2+\lambda^2\alpha^3-\lambda^3\alpha^3\theta_0$
θ_{3out}	$=\lambda\theta_{3in}$	$=\lambda\left(\lambda^3\theta_0+\lambda^2\alpha-3\lambda^3\alpha\theta_0+\lambda\alpha-2\lambda^2\alpha^2+3\lambda^3\alpha^2\theta_0+\alpha-\lambda\alpha^2+\lambda^2\alpha^3-\lambda^3\alpha^3\theta_0\right)$

No pattern quickly emerges from this sequence. However, the pattern emerges if one looks at the difference between the entering fractional coverage for each cycle and that of the previous cycle. In table 2-3, N is the cycle number, and the difference in fractional coverage is defined as $\Delta\theta_N=\theta_N-\theta_{(N-1)}$.

Table 2-3 Difference in coverage expressions.

$\Delta\theta_1=\lambda\theta_0+\alpha-\lambda\alpha\theta_0-\theta_0$
$\Delta\theta_2=\lambda(1-\alpha)(\lambda\theta_0+\alpha-\lambda\alpha\theta_0-\theta_0)$
$\Delta\theta_3=\lambda^2(1-\alpha)^2(\lambda\theta_0+\alpha-\lambda\alpha\theta_0-\theta_0)$
$\Delta\theta_4=\lambda^3(1-\alpha)^3(\lambda\theta_0+\alpha-\lambda\alpha\theta_0-\theta_0)$
$\Delta\theta_5=\lambda^4(1-\alpha)^4(\lambda\theta_0+\alpha-\lambda\alpha\theta_0-\theta_0)$
$\Delta\theta_N=\lambda^{(N-1)}(1-\alpha)^{(N-1)}(\lambda\theta_0+\alpha-\lambda\alpha\theta_0-\theta_0)$

Thus, the equation for the coverage going into the pin contact at any cycle *n* is the initial coverage plus the sum of the differences up to cycle *n*, as shown in eqn. 2.1.

$$\theta_{n,in}=\theta_0+\left(\sum_{N=1}^{n}\lambda^{(N-1)}(1-\alpha)^{(N-1)}\right)(\lambda\theta_0+\alpha-\lambda\alpha\theta_0-\theta_0) \qquad \text{eqn 2.1}$$

Quite fortuitously this series has a closed-form expression, given in eqn 2.2.

$$\sum_{N=1}^{n}\lambda^{(N-1)}(1-\alpha)^{(N-1)}=\frac{1-(\lambda(1-\alpha))^n}{1-\lambda+\alpha\lambda} \qquad \text{eqn 2.2}$$

The cycle-dependent entering fractional coverage at any cycle *n* can then be compactly written as given in eqn. 2.3.

$$\theta_{in} = \theta_0 \left(\lambda(1-\alpha)\right)^n + \alpha\left(\frac{1-\lambda^n(1-\alpha)^n}{1-\lambda(1-\alpha)}\right) \qquad \text{eqn 2.3}$$

The steady-state solution for the entering fractional coverage can be determined by taking the limit of this function as the number of cycles approaches infinity, given by eqn 2.4.

$$\theta_{ss,in} = \frac{\alpha}{1-(1-\alpha)\lambda} \qquad \text{eqn 2.4}$$

This expression agrees with steady-state expressions developed previously by Sawyer and Blanchet [17]. The adsorption ratio α can be found from the Langmuir solution for vapor adsorption, which states that the rate of adsorption is a product of the adsorption coefficient (v), the gas pressure (P), and the nascent surface area fraction $(1-\theta)$.

$$\frac{d\theta}{dt} = \nu P(1-\theta) \qquad \text{eqn 2.5}$$

From this, the change in fractional coverage for any cycle is given by eqn 2.6, where t_c is the time the element is exposed to the environment between exiting the contact and re-entry. The adsorption fraction is then given by eqn 2.7.

$$\theta_{n,in} = 1-(1-\theta_{n-1,out})e^{(-\nu P t_c)} \qquad \text{eqn 2.6}$$

$$\alpha = 1-e^{(-\nu P t_c)} \qquad \text{eqn 2.7}$$

The derivation of the adsorption fraction from the Langmuir model can be seen in Appendix A. Substituting this expression for α into eqn 2.3 and simplifying gives eqn 2.8, which is a cycle-dependent solution for the entering fractional coverage.

$$\theta_{in} = \theta_0\left(\lambda^n\left(e^{-n\nu P t_c}\right)\right) + \left(1-e^{-\nu P t_c}\right)\left(\frac{1-\lambda^n\left(e^{-n\nu P t_c}\right)}{1-\lambda\left(e^{-\nu P t_c}\right)}\right) \qquad \text{eqn 2.8}$$

The exposure time for one cycle (t_c) can be expressed as a track length (L) divided by the sliding speed (V), t_c = L/V, and the number of cycles can be expressed as the product of the sliding speed (V) and the cumulative run time (T) divided by the track length (L), n=VT/L. The fractional coverage of the surface entering the contact as a function of run time, track length and velocity (parameters normally measured during tribological experiments) is given by eqn 2.9.

$$\theta_{in} = \theta_0\left(\lambda^{\left(\frac{VT}{L}\right)}\left(e^{-\left(\frac{VT}{L}\right)\left(\frac{\nu PL}{V}\right)}\right)\right)+\left(1-e^{-\left(\frac{\nu PL}{V}\right)}\right)\left(\frac{1-\lambda^{\left(\frac{VT}{L}\right)}\left(e^{-\left(\frac{VT}{L}\right)\left(\frac{\nu PL}{V}\right)}\right)}{1-\lambda\left(e^{-\left(\frac{\nu PL}{V}\right)}\right)}\right) \qquad \text{eqn 2.9}$$

The relationship between the entering fractional coverage (θ_{in}) and the average fractional coverage ($\bar{\theta}$) under the pin can be derived from the fractional removal equations developed by Blanchet and Sawyer [18], as shown in eqn 2.10.

$$\bar{\theta} = \theta_{in}\frac{(1-\lambda)}{-\ln(\lambda)} \qquad \text{eqn 2.10}$$

The average fractional coverage under the pin contact at any cumulative run time is found by substituting eqn 2.9 into eqn 2.10, which is done in eqn 2.11.

$$\bar{\theta} = \frac{(1-\lambda)}{-\ln(\lambda)}\left(\theta_0\lambda^{\left(\frac{VT}{L}\right)}e^{-\left(\frac{VT}{L}\right)\left(\frac{\nu PL}{V}\right)}+\left(1-e^{-\left(\frac{\nu PL}{V}\right)}\right)\left(\frac{1-\lambda^{\left(\frac{VT}{L}\right)}\left(e^{-\left(\frac{VT}{L}\right)\left(\frac{\nu PL}{V}\right)}\right)}{1-\lambda\left(e^{-\left(\frac{\nu PL}{V}\right)}\right)}\right)\right) \qquad \text{eqn 2.11}$$

Two nondimensional groups can be defined: normalized time $T^* = VT/L$, and normalized deposition $D^* = \nu PL/V$. Substituting these two nondimensional groups into

eqn 2.11 gives a dimensionless form of average fractional coverage under the contact in eqn 2.12.

$$\bar{\theta} = \theta_0 \left(\frac{(1-\lambda)}{-\ln(\lambda)} \right) \left(\lambda^{T^*} \left(e^{-T^* D^*} \right) \right) + \left(\frac{(1-\lambda)}{-\ln(\lambda)} \right) \left(1 - e^{-D^*} \right) \left(\frac{1 - \lambda^{T^*} \left(e^{-T^* D^*} \right)}{1 - \lambda \left(e^{-D^*} \right)} \right) \qquad \text{eqn 2.12}$$

The model derived by examining a rotating pin-on-disk configuration can be used to predict fractional coverage values for any point around the circular wear path of a pin-on-disk contact because all the points around the track experience the same amount of exposure time to the environment between pin contacts. For this reason the model can also be used to predict coverage values for the midpoint of a reciprocating pin-on-flat contact because the midpoint of reciprocation sees the same amount of environmental exposure times between pin contacts.

The correlation of model predicted surface coverage to predicted friction coefficient is done in section 2.4. This can then be used for comparison to experimental friction results.

2.3. Positional Reciprocation Model

In a reciprocating configuration the amount of time a given spot will be exposed to the environment will depend on both the sliding velocity and the location along the track. The schematic of the reciprocating configuration is shown in Figure 2-2.

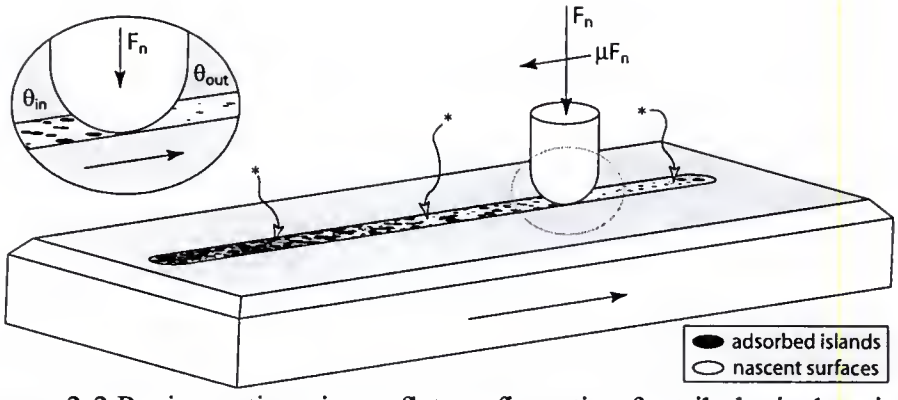

Figure 2-2 Reciprocating pin-on-flat configuration for tribological testing.

In reciprocating tribometry, every location on the wear track comes in and out of contact with the pin moving either forward (subscript f) or reverse (subscript r); it makes no difference whether the pin or the counterface is moving for the purposes of modeling, which uses a counterface-attached coordinate system for the derivation. The amount of time a particular location is exposed to the environment is a function of its location, the overall path length, and sliding speed of the pin, which is assumed to be constant along the track length. The increase in coverage at a particular location is a function of the surface area fraction (θ) when the pin last exposed the counterface at that position and the amount of time ($t_{(f,r)}$) that the location was exposed to the environment before the pin returned. One item to note is the distinction between the forward (t_f) and reverse (t_r) exposure times. For any given position along the wear track there exists unique values for t_f and t_r, only at the midpoint does $t_f = t_r$. The total cycle time (t_c) is defined as the sum of the forward and reverse portions of the cycle motion, $t_c = t_f + t_r$. Speed dependence of the coefficient of friction is attributed to a change in exposure time between contacts, the faster the sliding speed the less time between pin contacts (lower

values of $t_{(f,r)}$). Figure 2-3 shows the schematic used for this position and time-dependent reciprocating modeling.

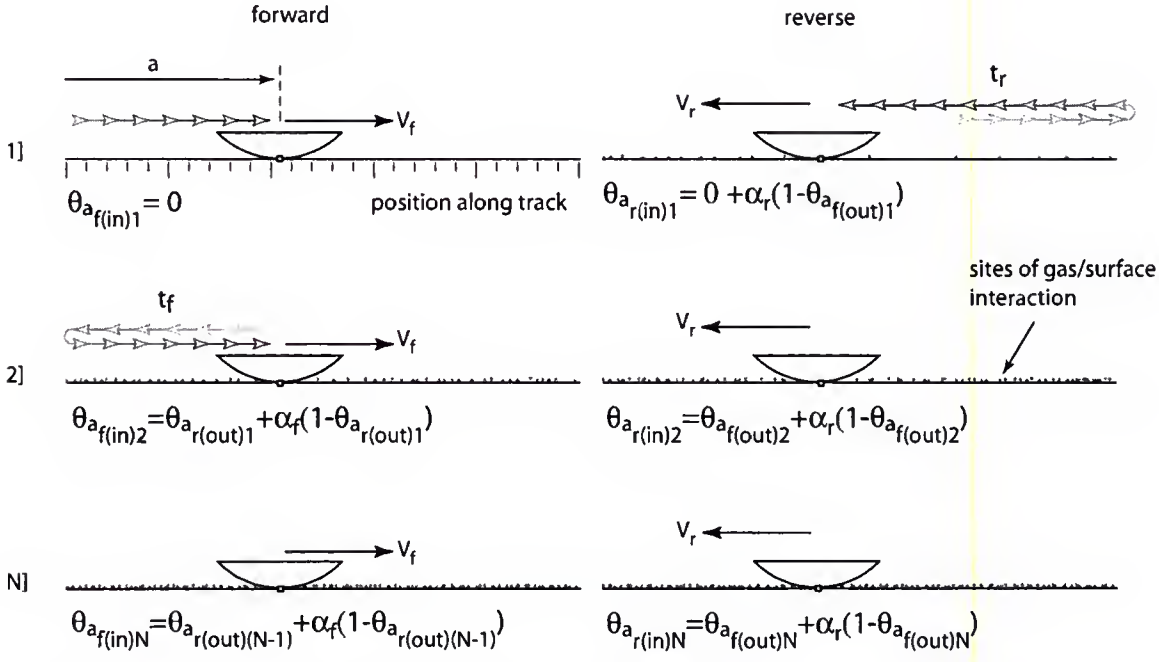

Figure 2-3 Positional reciprocation schematic.

The modeling initiates with each position along the track having $\theta = 0$ coverage for the first forward pass. On the first reverse pass the pin has traveled to the end of the wear track and back to the position of interest. During this time the reverse adsorption fraction (α_r) acts on the nascent portion of the surface from the previous pass $\left(1-\theta_{f_{out}}\right)$, giving an entering fractional coverage ($\theta_{r_{in}}$) of the form $\theta_{(r,f)_{in}} = \theta_{(f,r)_{out}} + (1-\theta_{(f,r)_{out}})\alpha_{(r,f)}$. Table 2-4 shows the evolution of the coverage equations derived for the position dependent modeling.

Table 2-4 Positional fractional coverage expressions.

1	f	in	$\theta_{f1in} = 0$	$\rightarrow$	0
		out	$\theta_{f1out} = \lambda\left(\theta_{f1in}\right)$	$\rightarrow$	0
	r	in	$\theta_{r1in} = \theta_{f1out} + \alpha_r\left(1-\theta_{f1out}\right)$	$\rightarrow$	α_r
		out	$\theta_{r1out} = \lambda\left(\theta_{r1in}\right)$	$\rightarrow$	$\lambda\alpha_r$
2	f	in	$\theta_{f2in} = \theta_{r1out} + \alpha_f\left(1-\theta_{r1out}\right)$	$\rightarrow$	$\lambda\alpha_r + \alpha_f\left(1-\lambda\alpha_r\right)$
		out	$\theta_{f2out} = \lambda\left(\theta_{f2in}\right)$	$\rightarrow$	$\lambda\left(\lambda\alpha_r + \alpha_f\left(1-\lambda\alpha_r\right)\right)$
	r	in	$\theta_{r2in} = \theta_{f2out} + \alpha_r\left(1-\theta_{f2out}\right)$	$\rightarrow$	$\lambda\left(\lambda\alpha_r + \alpha_f\left(1-\lambda\alpha_r\right)\right) + \alpha_r\left(1-\lambda\left(\lambda\alpha_r + \alpha_f\left(1-\lambda\alpha_r\right)\right)\right)$
		out	$\theta_{r2out} = \lambda\left(\theta_{r2in}\right)$	$\rightarrow$	$\lambda\left(\begin{array}{c}\lambda\left(\lambda\alpha_r + \alpha_f\left(1-\lambda\alpha_r\right)\right) + \\ \alpha_r\left(1-\lambda\left(\lambda\alpha_r + \alpha_f\left(1-\lambda\alpha_r\right)\right)\right)\end{array}\right)$

This process continues, forward-reverse-forward-reverse ..., as illustrated in Figure 2-3. The change in fractional coverage that occurs when the pin rides over a particular location ($\theta_{(f,r)_{in}} - \theta_{(f,r)_{out}}$) follows a model for the fractional removal of films as in the rotating section, of the form $\theta_{(f,r)_{out}} = \lambda\theta_{(f,r)_{in}}$, where λ is a removal ratio between $\lambda = 0$ (complete removal) and $\lambda = 1$ (no removal).

For consecutive forward and reverse passes the difference in entering fractional coverage is given in Table 2-5 for the first 4 cycles. The change in entering fractional coverage is defined as $\Delta\theta_N = \theta_{N+1} - \theta_N$ for any cycle N, where the subscript N is understood to mean N_{in}.

Table 2-5 Positional difference in coverage expressions.

forward	reverse
$\Delta\theta_{f1} = \left(\alpha_r\lambda + \alpha_f - \alpha_f\alpha_r\lambda\right)$	$\Delta\theta_{r1} = \lambda\left(1-\alpha_r\right)\Delta\theta_{f1}$
$\Delta\theta_{f2} = \lambda^2\left(1-\alpha_f\right)\left(1-\alpha_r\right)\Delta\theta_{f1}$	$\Delta\theta_{r2} = \lambda^3\left(1-\alpha_f\right)\left(1-\alpha_r\right)^2\Delta\theta_{f1}$
$\Delta\theta_{f3} = \lambda^4\left(1-\alpha_f\right)^2\left(1-\alpha_r\right)^2\Delta\theta_{f1}$	$\Delta\theta_{r3} = \lambda^5\left(1-\alpha_f\right)^2\left(1-\alpha_r\right)^3\Delta\theta_{f1}$
$\Delta\theta_{f4} = \lambda^6\left(1-\alpha_f\right)^3\left(1-\alpha_r\right)^3\Delta\theta_{f1}$	$\Delta\theta_{r4} = \lambda^7\left(1-\alpha_f\right)^3\left(1-\alpha_r\right)^4\Delta\theta_{f1}$
$\Delta\theta_{fN} = \lambda^{(2N-2)}\left(1-\alpha_f\right)^{(N-1)}\left(1-\alpha_r\right)^{(N-1)}\Delta\theta_{f1}$	$\Delta\theta_{rN} = \lambda^{(2N-1)}\left(1-\alpha_f\right)^{(N-1)}\left(1-\alpha_r\right)^{N}\Delta\theta_{f1}$

The patterns for the differences in entering fractional coverage for forward and reverse passes in terms of cycle number, removal ratio λ and the forward and reverse adsorption fractions α_f and α_r are given in eqns 2.13 and 2.14 respectively:

$$\Delta\theta_{fN} = \lambda^{(2N-2)}\left(1-\alpha_f\right)^{(N-1)}\left(1-\alpha_r\right)^{(N-1)}\left(\alpha_r\lambda + \alpha_f - \alpha_f\alpha_r\lambda\right) \qquad \text{eqn 2.13}$$

$$\Delta\theta_{rN} = \lambda^{(2N-1)}\left(1-\alpha_f\right)^{(N-1)}\left(1-\alpha_r\right)^{N}\left(\alpha_r\lambda + \alpha_f - \alpha_f\alpha_r\lambda\right) \qquad \text{eqn 2.14}$$

The fractional coverage entering the pin contact for forward or reverse travel for any cycle (n) is the coverage entering the first cycle in that direction plus the sum of the differences in fractional coverage up to that cycle (n), as given by eqn 2.15.

$$\theta_{(f,r)n} = \theta_{(f,r)1} + \sum_{N=1}^{n}\Delta\theta_{(f,r)N} \qquad \text{eqn 2.15}$$

Fortunately, there are closed-form solutions to the summations in eqn. 2.15, and the entering coverage for any cycle with the pin moving either forward or reverse is given in eqns 2.16 and 2.17, respectively.

$$\theta_{fn} = \frac{c\left(1-g^{(n-1)}\right)}{1-g} \qquad \text{eqn 2.16}$$

$$\theta_m = \frac{b - cdg^{(n-1)}}{1-g} \qquad \text{eqn 2.17}$$

The variables (c, g, b, and d) are given in Table 2-6.

Table 2-6 Expressions for the variables (c, g, b, and d) used in eqns. 2.16 and 2.17. All variables are expressed in terms of the forward or reverse adsorption coefficient (α_f, α_r) and the removal ratio (λ).

c	$\lambda\alpha_r(1-\alpha_f)+\alpha_f$	$\lambda\left(1-e^{-\nu Pt_r}\right)e^{-\nu Pt_f}+\left(1-e^{-\nu Pt_f}\right)$
g	$(1-\alpha_f)(1-\alpha_r)\lambda^2$	$e^{-\nu Pt_f}e^{-\nu Pt_r}\lambda^2$
b	$\lambda\alpha_f(1-\alpha_r)+\alpha_r$	$\lambda\left(1-e^{-\nu Pt_f}\right)e^{-\nu Pt_r}+\left(1-e^{-\nu Pt_r}\right)$
d	$\lambda(1-\alpha_r)$	$\lambda e^{-\nu Pt_r}$

The adsorption fractions can be expressed in a Langmuir form similar to the previous model section as given by eqns 2.18 and 2.19 for the forward and reverse cases, respectively.

$$\alpha_f = 1 - e^{-\nu Pt_f} \qquad \text{eqn 2.18}$$

$$\alpha_r = 1 - e^{-\nu Pt_r} \qquad \text{eqn 2.19}$$

The adsorption fractions are a function of the deposition constant (ν), the partial pressure of the gas (P), and the exposure time in the forward or reverse directions (t_f, t_r). The only difference between the forward and reverse adsorption coefficients concerns the exposure time in the direction of travel t_f and t_r. Each position along the track has a unique value for t_f and t_r. Only at the midpoint of the track does t_f equal t_r. The coefficients ν and P are constants for a gaseous environment that is compositionally and thermally steady. Eqns 2.20 and 2.21 give the closed-form

expressions in a form similar to the position-dependent steady-state equations for reciprocating motion published in [23], where $t_c = t_f + t_r$.

$$\theta_{fn} = \left[1-(1-\lambda)e^{-\nu P t_f} - \lambda e^{-\nu P t_c}\right]\frac{\left[1-\left(\lambda^2 e^{-\nu P t_c}\right)^{(n-1)}\right]}{\left[1-\lambda^2 e^{-\nu P t_c}\right]} \qquad \text{eqn 2.20}$$

$$\theta_{rn} = \left[1-(1-\lambda)e^{-\nu P t_r} - \lambda e^{-\nu P t_c}\right] - \frac{\left[\lambda e^{-\nu P t_r} - e^{-\nu P t_c}\left(1-\lambda+\lambda^2 e^{-\nu P t_r}\right)\right]\left[\lambda^2 e^{-\nu P t_c}\right]^{(n-1)}}{\left[1-\lambda^2 e^{-\nu P t_c}\right]} \qquad \text{eqn 2.21}$$

The first check for the validity of eqns 2.20 and 2.21, which are spatially dependent (through t_f and t_r values) and time dependent (through the cycle number, n), was to evaluate the limit of these functions as $n \to \infty$ and compare this with the previously developed steady-state expressions, which were created by balancing the deposition and removal rates at steady state. As expected, eqns 2.20 and 2.21 are identical to the steady-state equations published earlier [23]. The second check was that this model matched the time-dependent model in eqn 2.8 developed in the pin-on-disk/reciprocation midpoint section at the midpoint of the track (when $t_f = t_r$). The final verification step was to take the limit of the model as $n \to \infty$ when $t_f = t_r$ and compare this to the steady-state coverage expression in eqn 2.4, derived using the pin-on-disk model. In all of these cases, the model was able to be expressed in an equivalent form to the previously developed models. To predict friction coefficients at specific pin locations, the average fractional coverage within the contact, $\overline{\theta}$, is calculated according eqn 2.10

2.4. Linear Rule of Mixtures

In the tribological experiments that are going to be used for comparison to this modeling the friction coefficient is the only value that can be used as an indication of surface coverage of environmental species. To correlate model predicted coverage, θ, to friction coefficient, μ, this work uses a linear rule-of-mixtures. The friction coefficient μ can be estimated by eqn 2.22, where μ_0 is the friction coefficient of the nascent surface, and μ_1 is the friction coefficient of the surface covered with adsorbed contaminants.

$$\mu = \mu_0 + \bar{\theta}\left(\mu_1 - \mu_0\right) \qquad \text{eqn 2.22}$$

A linear rule of mixtures is one of multiple approaches for predicting the influence of surface coverage on friction. There is no clearly defined correct relationship for how the surface coverage influences friction coefficient in these tribological contacts. While the influence of species coverage on friction coefficient may not follow a simple linear relationship, this work is going to use eqn 2.22 as a first approach to correlate read friction coefficient to surface coverage.

Figure 2-4 examines the comparative progression of the pin-on-disk/midpoint reciprocation model (Figure 2-4a) and the positional-dependent model (Figure 2-4b) from transient to steady state friction coefficient predictions. This is performed for a standard set of experimental conditions that will be examined in Chapter 3 of this work.

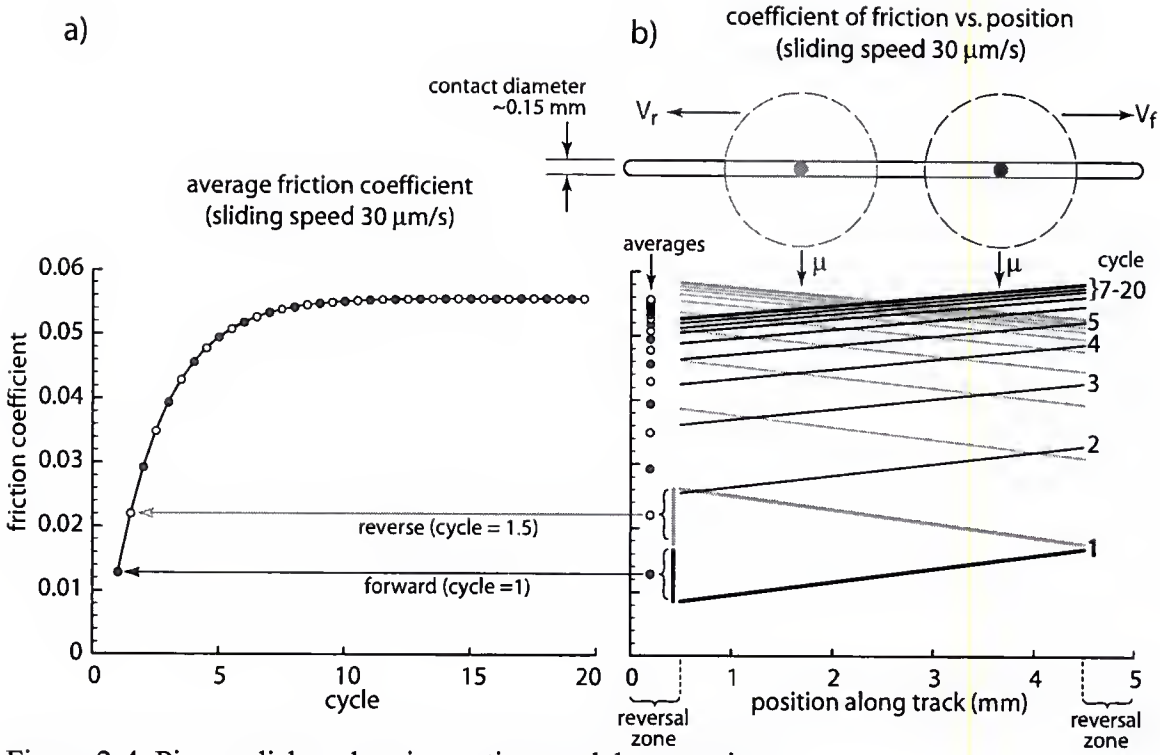

Figure 2-4 Pin-on-disk and reciprocating model comparison.

These model predictions for friction coefficient as a function of tribological testing conditions and environmental species can now be compared to other investigators' experimental results on self-mated NFC films in tribological contacts. This should give some indication if gas-surface interactions are playing a dominant role on the frictional behavior of these films.

CHAPTER 3
FRICTION MODELING AND DATA COMPARISON

3.1. Near-Frictionless Carbon Self-Mated Experiments

Other investigators, Heimberg et al., investigated the frictional behavior of NFC coatings [9]. Their samples consisted of a NFC coated 12.7-mm diameter steel sphere with a constant dead weight load of 9.8 N against a NFC coated H13 steel flat over a 5mm track length. All tests were run in nominally dry nitrogen (relative humidity and oxygen concentration of less than 1%). Their experimental apparatus was a reciprocating tribometer from which time dependent friction data was read. Position dependent (along reciprocating path) data was interpolated from the time dependent data. Details on their experiments and apparatus are covered in their publication [9].

Two sets of experiments run by Heimberg et al. were of interest to the modeling derived in this study. The first set of interest was a single series of tests in which sliding speed was varied from 0.01 to 5mm/s. Time-dependent data was collected over this series of experiments that varied the sliding speed systematically from high to low (the exposure time from short to long). At sliding speeds of 1-5 mm/s, this coating had a friction coefficient of $\mu = 0.007$, which is assumed to correspond to the friction coefficient of the nearly clean or nascent surface μ_0. At sliding speeds of 10 μm/s, this coating had a friction coefficient near $\mu = 0.12$, which was assumed to correspond to the friction coefficient of a nearly saturated or covered surface μ_1. The published friction

data from these tests was the average friction coefficient on each pass, which is assumed to be a reasonable approximation for the pin-on-disk/reciprocating midpoint model. This set of tests consisted of a single wear track that was run-in at 1mm/s until low friction ($\mu = 0.007$) was realized. Then, in the same track the speed was alternated between 1000 cycles of high speed (1 mm/s) sliding and 20 cycles of a lower speed (0.01-0.513 mm/s), systematically decreasing the lower sliding speed from high to low. During the portions of high speed sliding the exposure time between pin contacts is minimized and the amount of pin "wiping" is maximized. It is assumed for modeling the coverage (θ) during high speed sliding goes to zero and the friction coefficient goes to that of a fully nascent surface. The pin-on-disk/reciprocating midpoint model contains four parameters that were allowed to vary during the optimization routine that was employed against this data. These parameters are a deposition term νP, a removal ratio λ, and friction coefficients for the nascent and covered surfaces, μ_0 and μ_1 respectively. It was assumed that νP, μ_0 and μ_1 are constant for each data set run in the same continuous environment. The removal ratio λ was allowed to vary as a function of speed. Data from the sliding speed experiments of Heimberg et al. is shown in Figure 3-1.

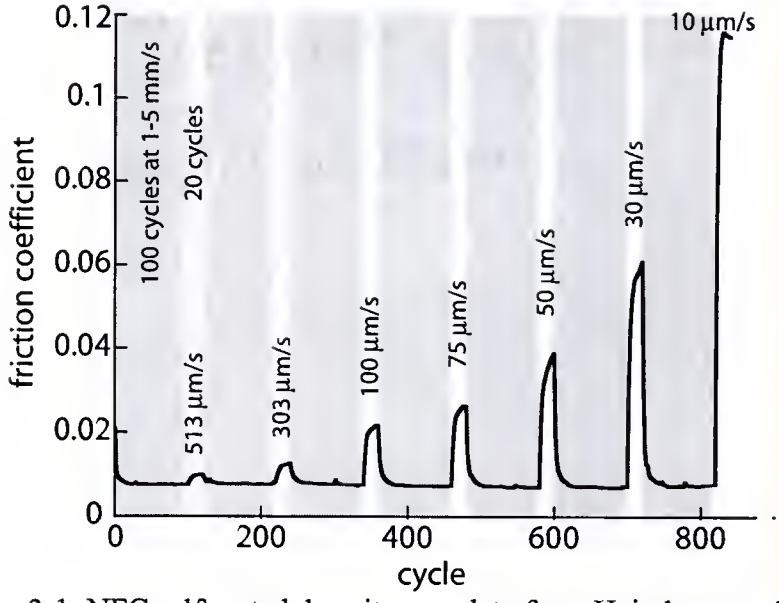

Figure 3-1 NFC self mated dry nitrogen data from Heimberg et al. [9].

Heimberg *et al.* also investigated the superlow friction behavior holding the sliding speed constant at 1 mm/s but varying the time between successive passes of the pin between 5 s and 162 s. This was to eliminate sliding speed and isolate exposure time between pin contacts as the variable in the friction coefficient performance. This data is also used for comparison to the pin-on-disk/reciprocation midpoint model. During these same experiments, time dependent data was taken along the reciprocation cycle. From this data, position dependent friction coefficient data was calculated for each cycle that average data was reported for in Figure 3-1. This position data was used for comparison with the positional reciprocating model equations (eqns 2.20 and 2.21).

3.2. Pin-on-Disk / Reciprocation Midpoint Model Fit

The pin-on-disk/reciprocating midpoint model fit (eqn 2.11) to the collected data (Figure 3-1) is shown in Figure 3-2a. This model fit gives a deposition term vP=0.00059 s^{-1}, a nascent surface friction coefficient $\mu_0 = 0.0075$, and a covered surface friction

coefficient $\mu_1 = 0.126$. The fraction removed $(1-\lambda)$ systematically increases with increasing sliding speed and decreasing friction coefficient (Figure 3-2b).

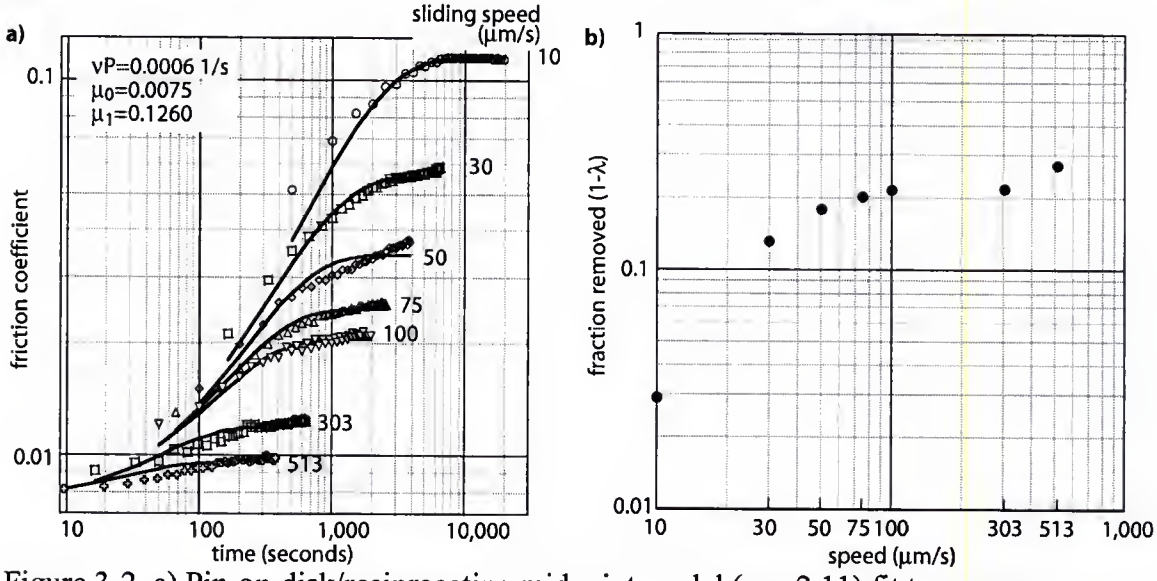

Figure 3-2 a) Pin-on-disk/reciprocating midpoint model (eqn 2.11) fit to average Heimberg et al. data (Figure 3-1). b) Fraction removed (1-λ) parameter as a function of sliding speed for model fit.

Model fits to the data in Figure 3-2 are also performed using two additional gas-surface adsorption models. Model derivation, fits to the data and discussion using both Henry's Law and the Elovich adsorption model expressions are included in Appendix B and C.

The fit of the pin-on-disk/reciprocating midpoint model (eqn 2.11) to the constant speed and dwell tests performed by Heimberg et al. is shown in Figure 3-3a. This model fit gives a deposition term vP=0.00067 s^{-1}, a nascent surface friction coefficient $\mu_0 = 0.0057$, and a covered surface friction coefficient $\mu_1 = 0.136$. The removal fraction $(1-\lambda)$ systematically increased with decreasing dwell times and decreasing friction coefficient (Figure 3-3b).

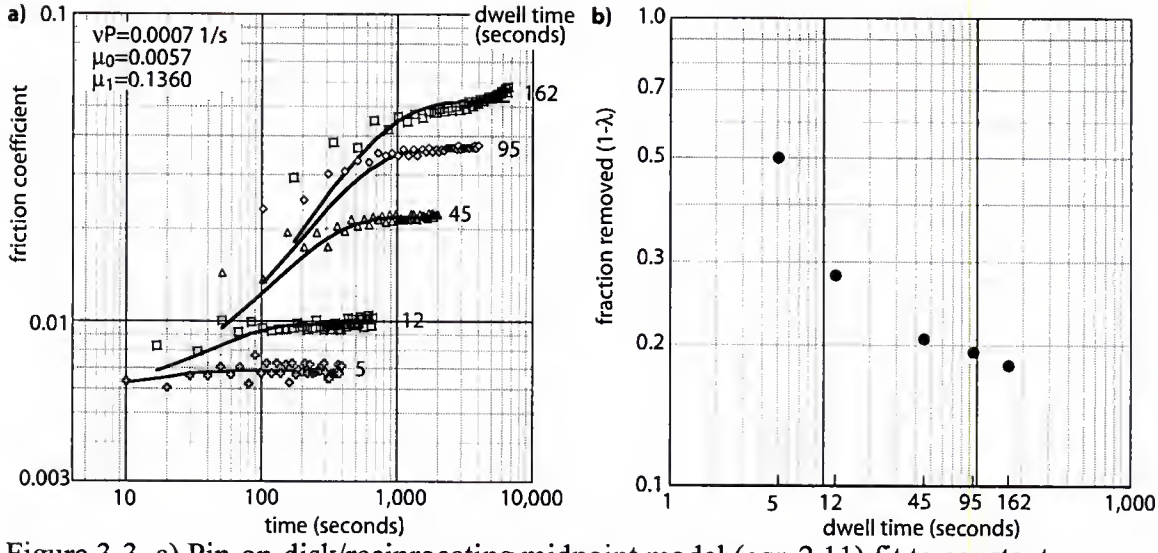

Figure 3-3 a) Pin-on-disk/reciprocating midpoint model (eqn 2.11) fit to constant velocity/dwell data. b) Fraction removed (1-λ) parameter as a function of dwell time for model fit.

The fit of pin-on-disk/reciprocation midpoint model to the average friction and dwell data is excellent; however, it does raise some interesting questions. Namely, why would the removal fraction change with sliding speed and dwell time? There is no suitable hypothesis for increasing removal fraction with increasing sliding speed and decreasing dwell times. Although, in both cases the fraction removed is increasing with decreasing exposure time, which suggests that the exposure time dependence of the removal fraction may be compensating for something missing in the deposition model. A couple of hypotheses can be offered. One hypothesis is that desorption of the contaminant species is occurring under the pin contact. As derived by Langmuir [12], the desorption rate increases monotonically with increasing surface temperature, and to the first order the dependence is to the square root of temperature. The low Peclet number suggests that stationary heat transfer analysis is appropriate, and, therefore, the temperature rise under the contact at any contaminated sites will be proportional to the sliding speed to the first power. However, fits to the constant speed tests showed

systematic variations that do not support this hypothesis. Another hypothesis is that the surface topography is changing during these experiments and this change is altering the removal rate. In both data sets the later experiments were less efficient at removing the contaminants than the earlier ones. This change in surface topography might also be enhancing the deposition rates, however, fits holding the removal ratio constant and allowing the deposition terms to vary did not fit the data well. Finally, since the later tests were also higher friction it may be that the removal fraction has a dependence on friction coefficient.

The parameters that were fit for these two data sets all gave remarkably reasonable results. The friction coefficients μ_0 and μ_1 were close to what were predicted prior to fitting and were similar for the two tests. The removal fraction $(1-\lambda)$ varied from nearly zero to 50%, which is also quite reasonable. It is somewhat curious that the time constant for the adsorption rate found by fitting eqn 2.11 to the data is between 1600 and 1800 seconds. This seems high for an adsorption process although dry nitrogen can have very little water and it may not be an adsorption process causing the increase in friction; rather, some other gas surface interaction.

3.3. Positional Reciprocation Model Fit

Time dependent data was taken along the reciprocation cycle for the experiments in Figures 3-1 and 3-2. Position dependent friction coefficient data was calculated from this time data and the positional reciprocating model equations (eqns 2.20 and 2.21) were fit to it. The model curves and data along the reciprocating length for cycle 19/20 under multiple sliding speeds is shown in Figure 3-4a (this condition was assumed to be nearly steady state). Figure 3-4b shows the model curves and data for multiple cycles during a single sliding speed. The model curves in Figure 3-4 use the parameters (νP, λ, μ_0 and μ_1) determined from the midpoint modeling (Figure 3-2), and no further curve fitting was performed. The data at the first and last 0.5 mm of track length were discarded due to the reversal zones. The grey dots in Figure 3-4 correspond to the crossing points in the model, where the coefficient of friction was the same in the forward and reverse motion directions for a specific cycle; at steady state this is at the midpoint.

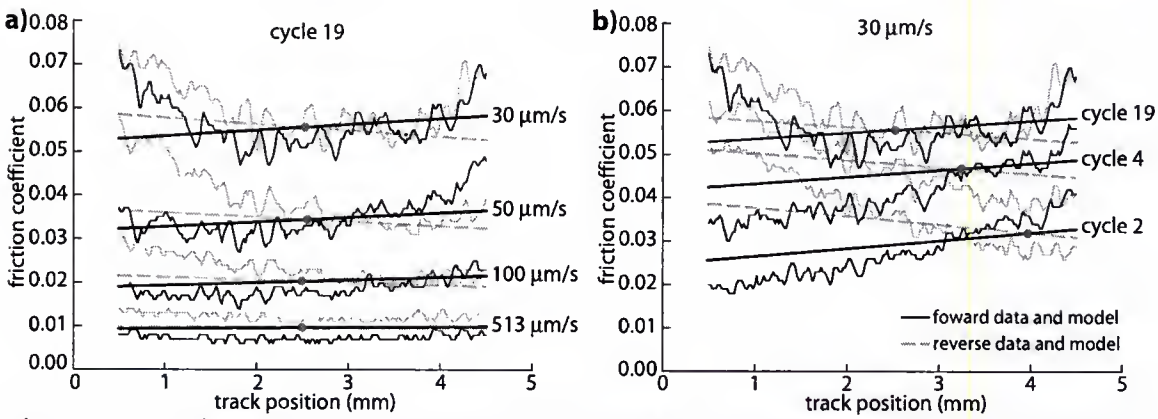

Figure 3-4 Positional model comparisons to friction coefficient data for a) cycle 19/20 at multiple sliding speeds. b) data from multiple cycles at a 30 µm/s sliding speed.

The positional reciprocating friction behavior provides a more detailed picture of the competitive rates of Langmuir adsorption and fractional removal, which can be tested

against NFC *vs.* NFC data. There are similarities between the model curves and the data. The first is that the model tracks the midpoint coefficient of friction data well. Secondly, the crossing point of the coefficient of friction between the forward and reverse directions of motion for a given cycle occurs in similar locations along the track in both the model and data. In Figure 3-4a the crossing points are located at approximately the midpoint track, when the model has reached steady state for multiple sliding speeds. As shown in Figure 3-4b, the crossing point for a single sliding speed progresses from the extremity of the wear track toward the midpoint as the coefficient of friction progresses towards steady state.

In the low friction regime $(\mu < 0.05)$ both the model and the data show close to linear variations in friction coefficient versus track position, with higher friction coefficient being found at the end of a cycle and lower friction coefficient at the beginning. Additionally, friction coefficients at a position on the track after the crossing point during forward motion are higher than the values at the same position after the turn around, during reverse motion. This difference in friction coefficient is due to the fact that for a specific track position past the midpoint, the exposure time between pin contacts is longer in the forward than in the reverse direction of travel, and the removal ratio is less than unity. Longer exposure time to the environment allows more adsorption/interaction to occur, resulting in a higher fractional coverage and friction coefficient. The linear variation of the model curves is surprising given that the surface coverage expressions have exponential dependencies; a description of the linear appearance of the model curves is included in Appendix D.

The monotonic rise in experimental curves in the low $(\mu < 0.05)$ friction regime may be due to surface chemical or physical effects, in addition to fractional coverage. These effects may include defect formation, defect annealing, and film formation, some of which have been identified in atomic-scale friction studies [24, 25]. There are also some differences between the model curves and data. A striking difference is the trend in the data for the friction coefficient to be higher at both the beginning and end of a cycle at higher friction levels $(\mu > 0.05)$. For these cases the model fails to describe the spatially-resolved friction data. The friction coefficient near the turn-around points is higher than in the middle of the track, independent of direction of travel.

The friction coefficient is not proportional to surface coverage, as it was in the superlow friction regime. This behavior in the high friction regime may be due to third bodies. Investigators have reported that transfer films are formed during sliding against DLC coatings in this friction regime [26, 27] and with NFC coatings against non-NFC coated counterfaces run in dry N_2 [28]. In contrast, transfer films have not been detected with NFC *vs.* NFC coatings in the superlow friction regime [3, 9]. The generation of transfer films at the higher friction coefficients indicates that gas-surface interactions promote detachment of material at the sliding interface. A gas could disrupt the passivating bonds at the nascent surface or produce surface films that detach intact. The likely gas culprit is H_2O, known to raise the friction coefficient of hydrogenated carbon coatings [10, 29]. *In situ* tribometry has recently provided direct evidence that sliding against DLC coatings in humid air produces thicker transfer films and higher friction coefficients than in dry air [27]. Thus, moisture likely promotes particle detachment, which requires extra energy and raises the friction coefficient.

Finally, although the model does not describe the higher friction behavior, one of the fit parameters in the model suggests why the friction behavior changed. As seen in Figure 3-2b, the fraction removed for each pass $(1-\lambda)$ approaches 0 for the slower sliding speeds, when the friction coefficient rises the most. The midpoint model curves and data for both the multiple sliding speeds (Figure 3-2) and dwell experiments (Figure 3-3) leading to higher friction have been re-examined. Instead of looking at the fraction removed $(1-\lambda)$ as a function of sliding speed, the removal ratio (λ) as a function of steady-state friction coefficient was examined. No additional model fits were performed. Figure 3-5 shows that as the friction coefficient climbed toward 0.12, $(1-\lambda)$ approached a value of 0.

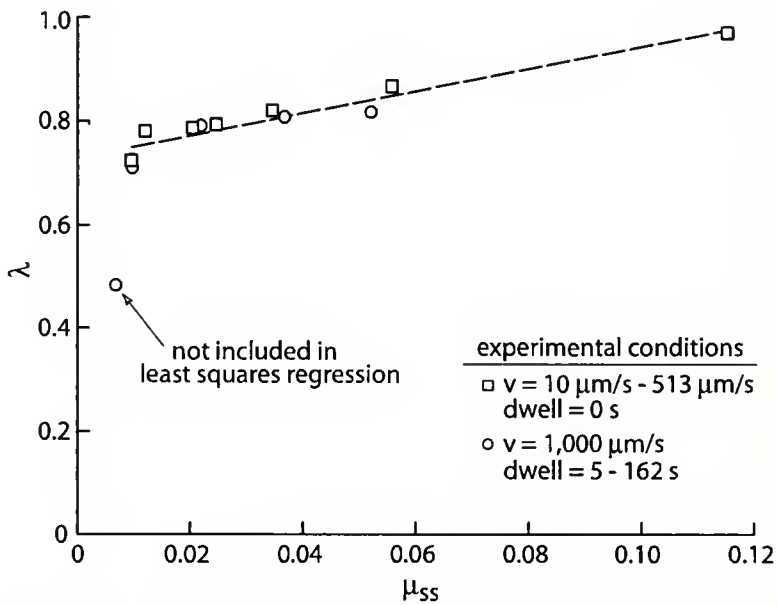

Figure 3-5 Removal ratio as a function of friction coefficient.

This suggests that as the friction coefficient increases, it becomes harder to continuously remove the product of the gas-surface interaction by wiping. One consequence would be that removal would become discontinuous, for example, by

coating fracture. However, surface analytical studies will be necessary to determine the actual physical changes that accompany the transition from the superlow to the higher friction (0.05 and up) regime.

One item of note in the Heimberg *et al.* experiments is the environment they used for all tests was nominally dry nitrogen. Their testing did not isolate which environmental species in the nitrogen may be leading to a rise in friction coefficient with increasing surface exposure time. Based on other investigators work [22] the two likely candidates in the chamber are water vapor and oxygen. In an effort to determine the culpable environmental species it would be beneficial to isolate and control levels of the potentially influential species in the chamber during tribological testing. This investigation aims to achieve such environmental experimentation on NFC films using a controlled environmental chamber and a low contact pressure tribometer. The experimental apparatus used for environmentally controlled experiments is analyzed in Chapter 4 of this work.

CHAPTER 4
MICRO-TRIBOMETER: EXPERIMENTAL APPARATUS AND UNCERTAINTY

4.1. Reciprocating Pin-on-Disk Microtribometer

The tribometer shown in Figure 4-1 is a commercially available instrument for testing the frictional properties of samples in reciprocating motion.

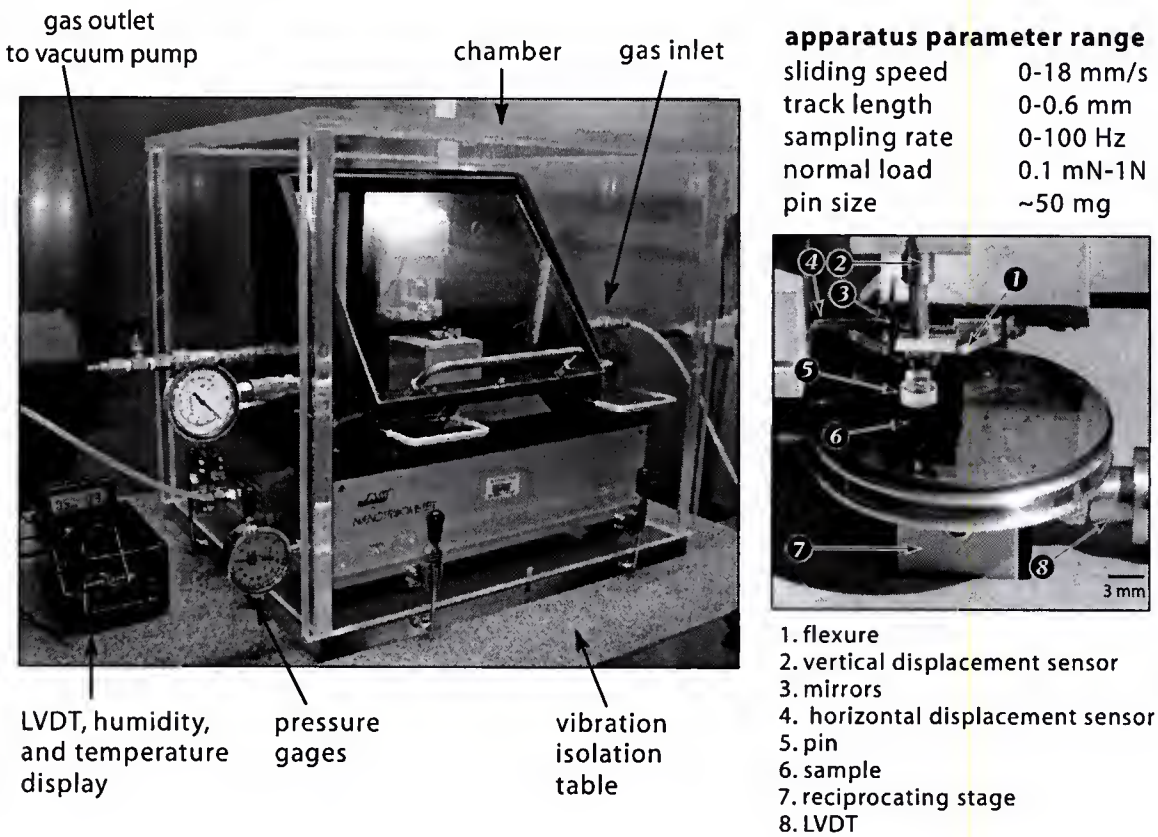

Figure 4-1 Environmental control, contact region and operational parameters of microtribometer.

This apparatus uses stepper motors for gross loading and positioning and piezo-electric actuators for fine loading, positioning and reciprocating motion. A dual flexure both applies normal load and reacts frictional forces between the pin and counterface

samples. Mirrors are mounted on this flexure in the horizontal and vertical directions. Optical light intensity sensors are positioned at a distance from the mirrors to read the magnitude of deflection of the flexure in the machine defined frictional and normal load directions. A pin sample is mounted on the end of the flexure using cyanoacrylate. The counterface is mounted on a microscopy stub which is fixed into the linear reciprocating stage. The tribometer was user outfitted with a linear variable displacement transducer (LVDT) to record relative reciprocating track position. Environmental control is achieved through a user designed acrylic chamber and the whole assembly is located on an active vibration isolation table. The tribometer operating parameter ranges of interest include a linear sliding speed up to 18 mm/sec, track length up to 0.6 mm, sampling rate up to 100 Hz, and a machine applied normal load range from 0.5 mN to 1N. This range of applied normal loads is achieved by having three different types of dual flexures, with varying stiffness values. Low range normal loading (0.5-100 mN) is achieved with a glass flexure, middle range loading (50 mN-300 mN) is achieved with a stainless steel flexure, and high range loading (200 mN-1N) is achieved with a thicker stainless steel flexure. Chamber gaseous species and counterface surface temperature control is outlined in Figure 4-2.

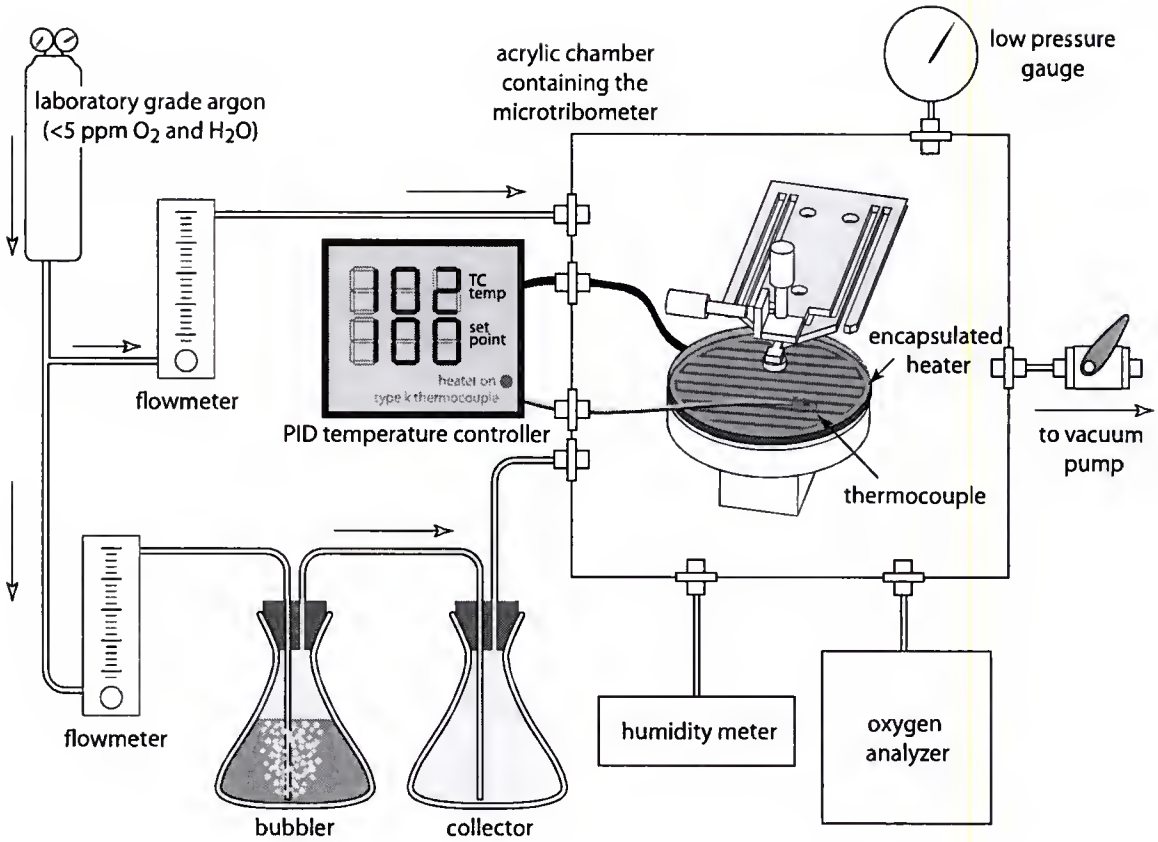

Figure 4-2 Gaseous environment and counterface surface temperature control.

All experiments in this study were run in an argon gas environment with varying amounts of water vapor added to the chamber. To achieve this laboratory grade argon as delivered from the manufacturer (<5 ppm O_2 and H_2O) is either delivered to the chamber as is or is bubbled through water to achieve varying amounts of water vapor while maintaining <20 ppm O_2 during tests. The chamber is outfitted with a 5 ppm resolution humidity meter and a 2 ppm resolution oxygen analyzer. There is also a rough vacuum pump attached to the chamber to promote rapid environment changes. For temperature testing the counterface substrate surface temperature is controlled through an encapsulated flexible heater mounted to the back side of the substrate and an adhesive thermocouple attached to the counterface surface. The working regions of the tribometer

can be examined in a schematic of the tribometer with the manufacturer designated axes of motion as shown in Figure 4-3.

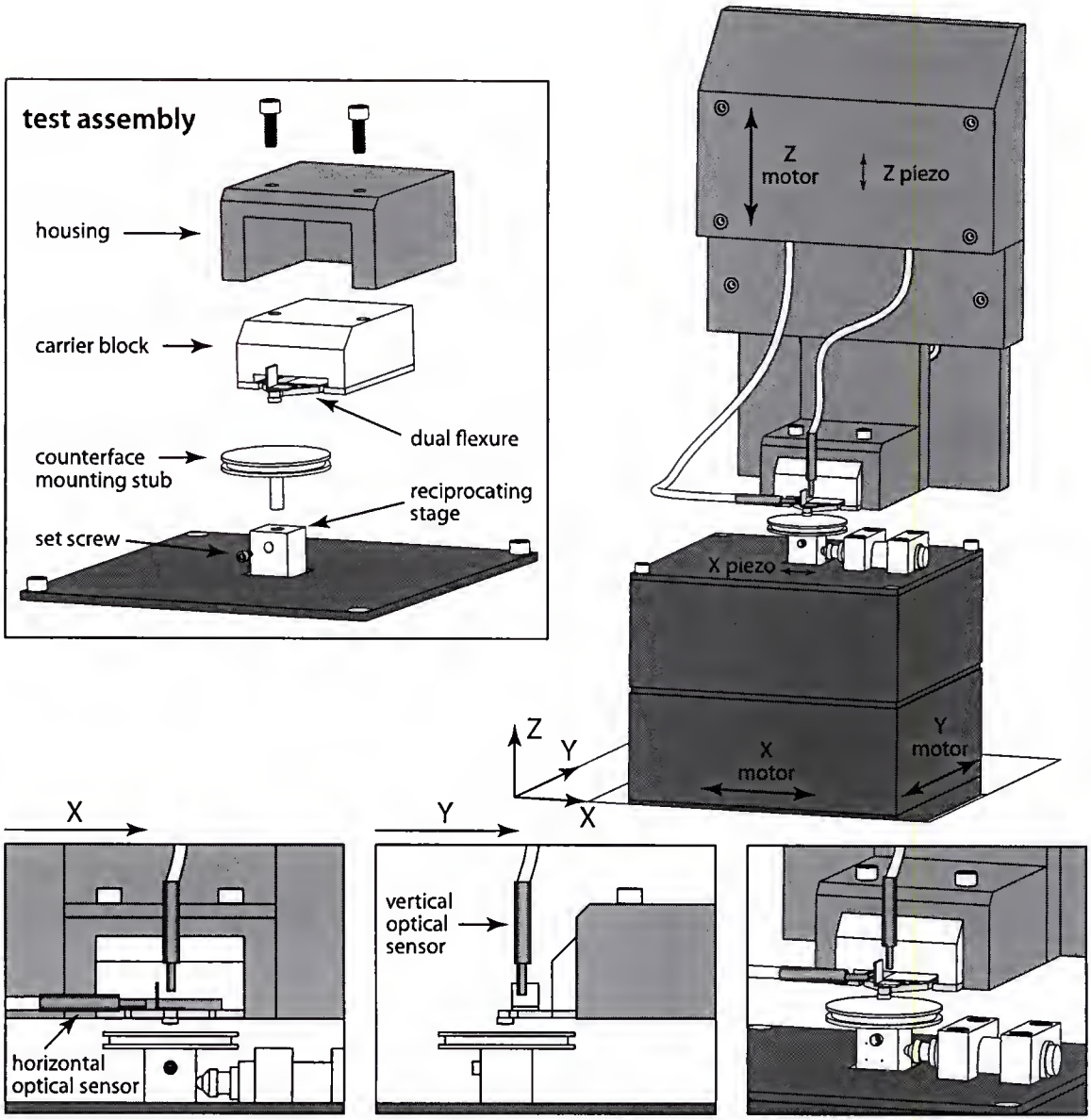

Figure 4-3 Schematic of tribometer test assembly and manufacturer defined axes of motion.

Each flexure comes from the manufacturer pre-mounted on a carrier block. The first step in using the apparatus is to mount that carrier block and dual flexure assembly into the flexure housing, using the machined faces of the carrier bock and housing as the mating surfaces and two screws for attachment. The positions of the optical sensors are

then adjusted so the unloaded starting distance between each optical sensor and mirror is in the middle of the operating voltage range of the optical sensor. The pre-mounted counterface sample and microscopy stub are then inserted into the reciprocating stage assembly and tightened in place using a set screw. The pin is located relative to the counterface through a software interface which actuates stepper motors in the X, Y and Z directions. The entire linear reciprocating stage is located on a platform that moves in the X and Y directions for sample positioning. Gross flexure housing assembly motion in the Z direction is achieved with a separate motor. Once the desired X and Y starting position of the pin is located the user enters test parameters into the software, including the desired Z direction approach speed and a value of minimum applied vertical load that defines pin contact on the counterface. The test is started and the software begins by automating the Z motion of the flexure housing assembly with the Z stepper motor until it is close to the desired vertical applied load, at which point the final Z motion is achieved through the Z axis piezo. After the vertical load is applied reciprocating motion is controlled by the X piezo. The reciprocating motion of the tribometer produces a frictional loop when the machine forward (μ_f') and reverse (μ_r') friction coefficient values are examined as a function of reciprocation track position. The forward and reverse reciprocating motion, along with the reversal locations makes a frictional loop for each cycle of sliding. An example of the positional friction coefficient data from the tribometer is shown in Figure 4-4.

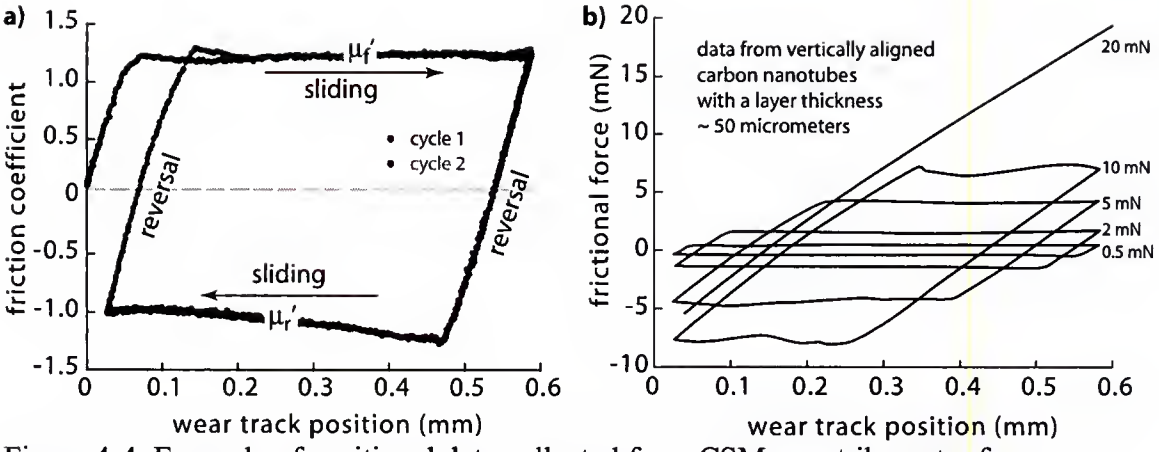

Figure 4-4 Example of positional data collected from CSM nanotribometer for a reciprocating test on vertically aligned nanotubes showing the loop of friction coefficient or frictional force versus wear track position.

Under certain loading and sliding speed conditions the free sliding portion of the frictional loop can become small (Figure 4-4b) or ever non-existent (20 mN load). During these portions the pin and base sample are stuck to one another and are moving together, without relative free sliding between the two samples. Only data during the free sliding portion of the frictional loop is used to report friction coefficient recorded during this investigation. The reversal location portion of the frictional loops is discarded. The frictional loop starts with the pin sample vertically loaded against the counterface at the beginning of cycle 1. The counterface begins to move in the arbitrarily designated forward direction. The pin and counterface samples stay in the same point of contact, experiencing no relative motion, until the counterface has moved far enough to build up sufficient strain in the flexure to break free. Once this happens there is free relative sliding between the pin and counterface in the forward direction until the end of the reciprocation track is reached. At this point the X piezo motion reverses to move in the opposite direction. Again, during reversal there is no relative motion between the pin and the counterface until the cantilever bends far enough in the opposite direction to break free and have free sliding reverse motion. This loop of free sliding and reversal continues

for all the reciprocation cycles of an experiment. A point to note in Figure 4-4a is the magnitude of the forward and reverse tribometer measured friction coefficient values is not equal. This discrepancy will be described by examining the method the machine uses to calculate the friction coefficient.

4.2. Microtribometer Friction Coefficient Values

The coefficient of friction defined by the microtribometer is the ratio of the measured force in the horizontal (X axis) direction to the applied load in the vertical (Z axis) direction. Misalignments between these tribometer measurement axes and the actual directions of the frictional and normal forces will lead to a discrepancy between the measured and actual friction coefficient values. This discrepancy between the forward and reverse reported friction coefficient values and the surface friction coefficient will be investigated by examining the design and method of signal measurements in the tribometer. Table 4-1 is a list of nomenclature that will be used in examining the influence of the tribometer design on the measured friction coefficient value.

Table 4-1 Nomenclature for microtribometer measurement analysis.

symbol	units	definition
μ	*	friction coefficient between pin and counterface
μ'	*	friction coefficient reported by tribometer
F	mN	force
subscript H	n/a	horizontal (along tribometer X axis)
subscript V	n/a	vertical (along tribometer Z axis)
subscript f	n/a	forward direction of sliding
subscript r	n/a	reverse direction of sliding
β	radians	misalignment roll angle
ϕ	radians	misalignment pitch angle
V	V	voltage read by optical sensor
C	um/V	sensor displacement-voltage calibration constant
K	mN/um	flexure stiffness
d	um	sensor-mirror offset error
G	1/um	flexure slope-displacement constant
$Mg_{1000\mu m}$	mN	stiffness calibration force
$V_{1000\mu m}$	V	stiffness calibration voltage

Since the counterface sample is user aligned and uses a set screw for attachment there are potential misalignments between the counterface orientation and the tribometer measured horizontal and vertical axes. The effect of two misalignment angles, β and ϕ, will be examined. Figure 4-5 defines these two misalignment angles and their resulting coordinate system rotations.

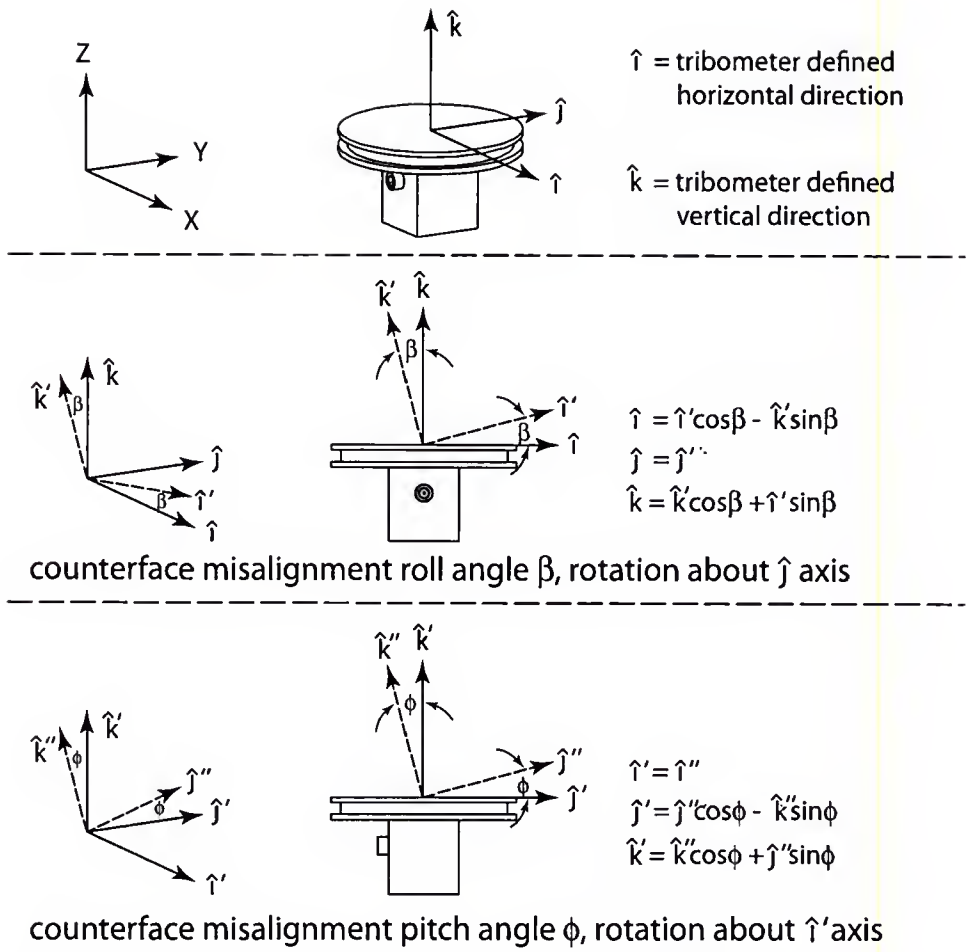

Figure 4-5 Potential misalignment angles in positioning counterface stub into reciprocating stage.

The counterface sample starts aligned with the tribometer measurements axis. Unit vectors located on the counterface, $\hat{i}$, $\hat{j}$,and $\hat{k}$ are respectively parallel to the X (horizontal), Y, and Z (vertical) measurement axes of the tribometer. In positioning the counterface stub into the reciprocating stage a first possible rotation error, the roll angle, β, about the $\hat{j}$ axis may occur, resulting in new counterface defined coordinates $\hat{i}'$, $\hat{j}'$ and $\hat{k}'$. A second possible rotation error, the pitch angle, ϕ, about the $\hat{i}'$ axis results in the final counterface orientation coordinate system, $\hat{i}''$, $\hat{j}''$ and $\hat{k}''$. The equations relating the actual counterface sample coordinate directions ($\hat{i}''$, $\hat{j}''$ and $\hat{k}''$) and the

tribometer measured coordinate directions ($\hat{i}$, $\hat{j}$,and $\hat{k}$) are shown in Figure 4-5. The force vectors tangent to the counterface surface in the forward and reverse directions are the vectors along the positive and negative $\hat{i}''$ direction.

$$\vec{F}_{\text{tangent}f} = \mu F_n \hat{i}'', \vec{F}_{\text{tangent}r} = -\mu F_n \hat{i}'' \qquad \text{eqns 4.1,4.2}$$

The force vectors normal to the counterface surface in the forward and reverse sliding directions are in the $\hat{k}''$ direction.

$$\vec{F}_{\text{normal}f} = F_n \hat{k}'', \vec{F}_{\text{normal}r} = F_n \hat{k}'' \qquad \text{eqns 4.3,4.4}$$

The total force vectors for each direction of sliding are the sums of the vectors acting tangent and normal and to the misaligned counterface surface.

$$\vec{F}_f = F_n \hat{k}'' + \mu F_n \hat{i}'' \qquad \text{eqn 4.5}$$

$$\vec{F}_r = F_n \hat{k}'' - \mu F_n \hat{i}'' \qquad \text{eqn 4.6}$$

Using the relations established in Figure 4-5 the counterface defined force vectors can then be related back through the pitch angle ϕ to get expressions in the $\hat{i}'$, $\hat{j}'$ and $\hat{k}'$ directions.

$$\vec{F}_f = F_n \cos\phi \hat{k}' - F_n \sin\phi \hat{k}' + \mu F_n \hat{i}' \qquad \text{eqn 4.7}$$

$$\vec{F}_r = F_n \cos\phi \hat{k}' - F_n \sin\phi \hat{k}' - \mu F_n \hat{i}' \qquad \text{eqn 4.8}$$

The forward and reverse force vectors can then be related back through the roll angle β to get an expression for the surface force vector in the $\hat{i}'$, $\hat{j}'$ and $\hat{k}'$ (tribometer read) directions.

$$\vec{F}_f = F_n \cos\beta\cos\phi\hat{k} - F_n \sin\beta\cos\phi\hat{i} - F_n \sin\phi\hat{j} + \mu F_n \cos\beta\hat{i} + \mu F_n \sin\beta\hat{k} \qquad \text{eqn 4.9}$$

$$\vec{F}_r = F_n \cos\beta\cos\phi\hat{k} - F_n \sin\beta\cos\phi\hat{i} - F_n \sin\phi\hat{j} - \mu F_n \cos\beta\hat{i} - \mu F_n \sin\beta\hat{k} \qquad \text{eqn 4.10}$$

The horizontal force read (F_H) and vertical force applied (F_V) by the tribometer can now be expressed in terms of the coefficient of friction (μ), the applied force normal to the counterface surface (F_n), and the two sample misalignment angles (β, ϕ).

The horizontal force components read by the tribometer are those in the $\hat{i}$ direction and the vertical force components are those in the $\hat{k}$ direction. Forward sliding expressions are shown in equations 4.11 and 4.12, reverse sliding expressions in equations 4.13 and 4.14.

$$F_{Hf} = \mu F_{nf} \cos\beta - F_{nf} \sin\beta\cos\phi \qquad \text{eqn 4.11}$$

$$F_{Vf} = \mu F_{nf} \sin\beta + F_{nf} \cos\beta\cos\phi \qquad \text{eqn 4.12}$$

$$F_{Hr} = -\mu F_{nr} \cos\beta - F_{nr} \sin\beta\cos\phi \qquad \text{eqn 4.13}$$

$$F_{Vr} = -\mu F_{nr} \sin\beta + F_{nr} \cos\beta\cos\phi \qquad \text{eqn 4.14}$$

The friction coefficients reported by the tribometer when moving in the forward (μ_f') and reverse (μ_r') directions are defined as the ratio of the horizontal to vertical forces.

$$\mu_f' = \frac{F_{Hf}}{F_{Vf}}, \mu_r' = \frac{F_{Hr}}{F_{Vr}} \qquad \text{eqns 4.15,4.16}$$

This results in expressions for the vertical force applied (F_V) by the tribometer in each sliding direction.

$$F_{Vf} = \frac{F_{Hf}}{\mu_f'}, F_{Vr} = \frac{F_{Hr}}{\mu_r'} \qquad \text{eqns 4.17,4.18}$$

The tribometer has active feedback control of the vertical force it applies, so the applied force in the forward and reverse sliding directions can be equated (F_{Vf}=F_{Vr}=F_V).

Equating the vertical applied force expressions in the forward (eqn 4.12) and reverse (eqn 4.14) directions results in a relation between the actual surface applied normal forces in the forward and reverse directions.

$$F_{nr} = F_{nf}\frac{(\cos\phi\cos\beta + \mu\sin\beta)}{(\cos\phi\cos\beta - \mu\sin\beta)} \qquad \text{eqn 4.19}$$

Using expressions from eqns 4.11-4.14, the horizontal force read by the tribometer when sliding in the forward and reverse directions (F_{Hf}, F_{Hr}) can be expressed in terms of the vertical force applied by the tribometer (F_V) the coefficient of friction at the surface (μ) and the misalignment angles (β, ϕ).

$$F_{Hf} = F_V\frac{(\mu\cos\beta - \cos\phi\sin\beta)}{(\cos\phi\cos\beta + \mu\sin\beta)}, F_{Hr} = -F_V\frac{(\mu\cos\beta + \cos\phi\sin\beta)}{(\cos\phi\cos\beta - \mu\sin\beta)} \qquad \text{eqns 4.20,4.21}$$

Using relations in eqns 4.15-4.21 the tribometer read friction coefficients in the forward (μ_f') and reverse (μ_r') directions can be expressed in terms of the actual coefficient of friction (μ) and the misalignment angles (β, ϕ).

$$\mu_f' = \frac{(\mu\cos\beta - \cos\phi\sin\beta)}{(\cos\phi\cos\beta + \mu\sin\beta)}, \mu_r' = \frac{(\mu\cos\beta + \cos\phi\sin\beta)}{(\mu\sin\beta - \cos\phi\cos\beta)} \qquad \text{eqns 4.22,4.23}$$

From eqns 4.22 and 4.23 expressions for the actual coefficient of friction (μ) in terms of the tribometer read forward (μ_f') and reverse (μ_r') values and the misalignment angles (β, ϕ) can be found.

$$\mu = \cos\phi\frac{(\mu_f'\cos\beta + \sin\beta)}{(\cos\beta - \mu_f'\sin\beta)}, \mu = -\cos\phi\frac{(\mu_r'\cos\beta + \sin\beta)}{(\cos\beta - \mu_r'\sin\beta)} \qquad \text{eqns 4.24,4.25}$$

For a frictionally isotropic material the relations for the friction coefficient (μ) in eqns 4.24 and 4.25 can be equated.

$$\cos\phi\frac{\left(\mu_f^{'}\cos\beta+\sin\beta\right)}{\left(\cos\beta-\mu_f^{'}\sin\beta\right)}=-\cos\phi\frac{\left(\mu_r^{'}\cos\beta+\sin\beta\right)}{\left(\cos\beta-\mu_r^{'}\sin\beta\right)} \qquad \text{eqn 4.26}$$

The pitch angle, ϕ, is cancelled by the equating of μ. This is not a surprising result since the pitch angle ϕ is in a direction insensitive to the measured horizontal force. This leaves an expression for the roll angle, β, in terms of the forward and reverse tribometer reported friction coefficients. It is expected that the misalignment angles of the counterface samples will be relatively small and for this reason small angle approximations are used to further simplify eqn 4.26.

$$\frac{\left(\mu_f^{'}+\beta\right)}{\left(1-\mu_f^{'}\beta\right)}=-\frac{\left(\mu_r^{'}+\beta\right)}{\left(1-\mu_r^{'}\beta\right)} \qquad \text{eqn 4.27}$$

$$\beta^2\left(\mu_f^{'}+\mu_r^{'}\right)+2\beta\left(\mu_f^{'}\mu_r^{'}-1\right)-\left(\mu_f^{'}+\mu_r^{'}\right)=0 \qquad \text{eqn 4.28}$$

The roll angle (β) is expected to very small and the values of μ_f' and μ_r' are usually fractions. For this reason the higher order terms of $\beta^2\mu$ are dropped from eqn 4.28.

$$2\mu_f^{'}\mu_r^{'}\beta-2\beta-\mu_f^{'}-\mu_r^{'}=0 \qquad \text{eqn 4.29}$$

This results in an expression for the misalignment angle (β) in terms of the tribometer reported forward and reverse friction coefficients (μ_f', μ_r').

$$\beta=\frac{\left(\mu_f^{'}+\mu_r^{'}\right)}{2\left(\mu_f^{'}\mu_r^{'}-1\right)} \qquad \text{eqn 4.30}$$

Which can also be expressed in terms of the tribometer applied normal load (F_V) and the forward and reverse horizontal read forces (F_{Hf}, F_{Hr}).

$$\beta = \frac{F_V\left(F_{Hf} + F_{Hr}\right)}{2\left(F_{Hf}F_{Hr} - F_V^2\right)} \qquad \text{eqn 4.31}$$

The effect of the misalignment angle β on the forward and reverse tribometer read friction coefficients as expressed in eqn 4.31 is shown in Figure 4-6 by examining lines of constant misalignment angle β.

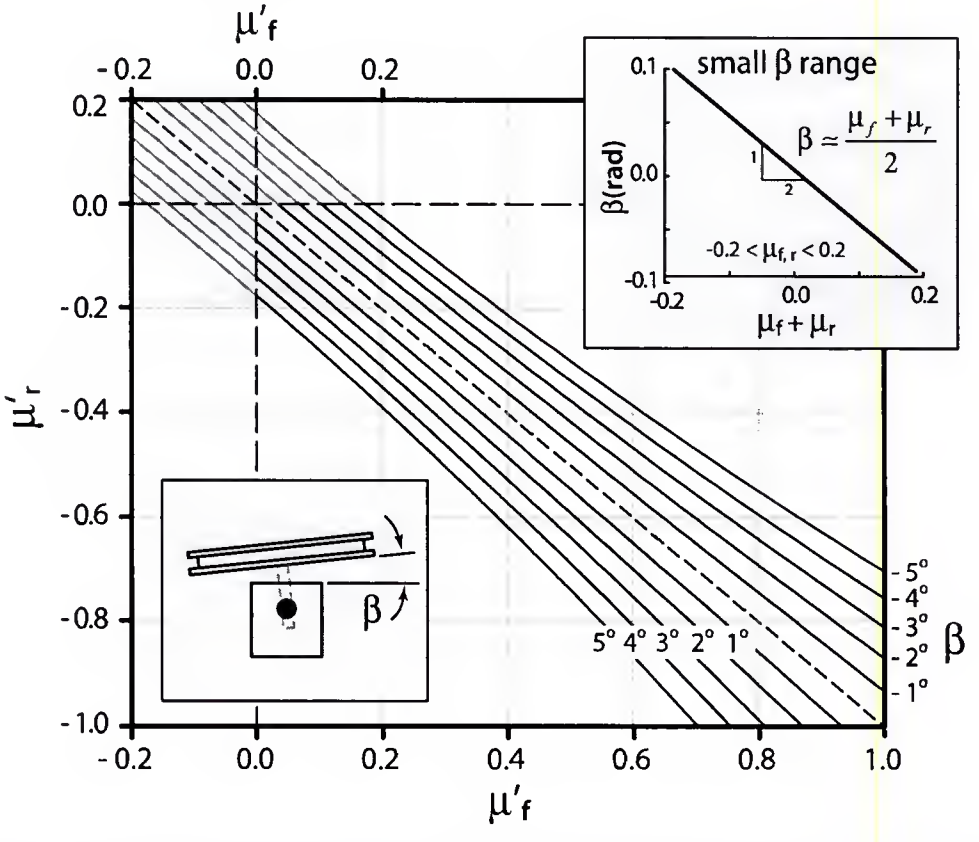

Figure 4-6 The effect of the misalignment angle β on the ratio of the tribometer reported forward and reverse friction coefficient values.

The insert in Figure 4-6 shows that for small values of forward and reverse friction coefficient ($|\mu_f', \mu_r'| < 0.2$), the misalignment angle becomes the average of the two reported friction coefficient values. This analysis allow for the misalignment roll angle, β, to be solved given the forward and reverse friction coefficients reported from the

microtribometer. The bias error in the friction coefficient due to β is corrected for in the equations developed for the friction coefficient, μ.

An equation derived frictional loop can now be examined to see the influence of the misalignment angle β on the relative magnitudes of the forward, μ_f', and reverse, μ_r', tribometer read friction coefficients. Figure 4-7 is a frictional loop generated from eqns 4.22 and 4.23 with β=5° and a flexure with a high stiffness value (same flexure as used for all of the experiments in this study).

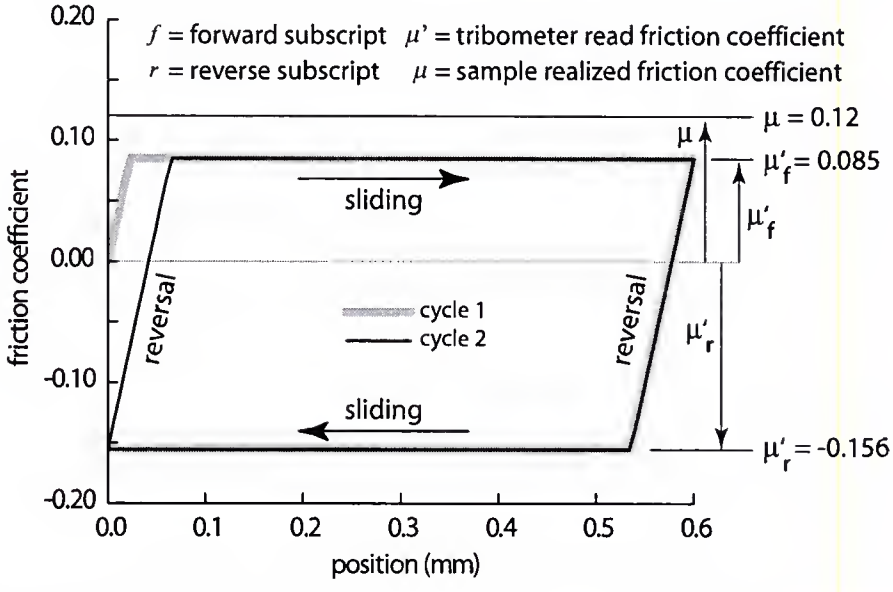

Figure 4-7 Equation derived frictional loop for pin and counterface pair with friction coefficient μ=0.12 and misalignment roll angle β=5°.

The slopes of the reversal portions of this frictional loop are due to the stiffness of the flexure used. All else held constant, the stiffer the flexure, the greater the slope and the smaller the amount of the frictional loop is due to reversal motions. This general trend makes sense since the stiffer the flexure, the less strain needs to be built up before there will be free sliding between the pin and counterface sample. The relative magnitudes of the forward and reverse tribometer reported friction coefficient values are

a function of the misalignment roll angle, β. The larger the value of β, the larger the difference between the magnitudes of μ_f' and μ_r'.

4.3. Propagation of Uncertainty in the Friction Coefficient

The friction coefficient (μ) as defined in eqn 4.24 is calculated from the tribometer read forward (μ_f') and reverse (μ_r') values and the misalignment angles (β, ϕ). Values for these parameters have to be determined to report a value for the friction coefficient.

4.3.1. Law of Propagation of Uncertainty

When measuring a quantity it should be recognized that there is no exact measurement. Therefore, when reporting measurement values both the measured value and the uncertainty in that value should be stated. A method for the evaluation of the uncertainty in measurements is outlined in [30,31]. This method defines a systematic procedure to incorporate uncertainties in all the measured values in a function to find the overall combined standard uncertainty of that function value. The general expression to determine the variance (combined standard uncertainty squared) of any function $G(x,y,z)$ is expressed in eqn 4.32 [30,31].

$$u^2_{cG(x,y,z)} = \left(\frac{\partial G}{\partial x}\right)^2 (u_x)^2 + \left(\frac{\partial G}{\partial y}\right)^2 (u_y)^2 + \left(\frac{\partial G}{\partial z}\right)^2 (u_z)^2 \qquad \text{eqn 4.32}$$

This expression assumes no covariance between the measured values in the function. To use this method, a value for the uncertainty in the measured value of each parameter ($u_{x,y,z}$) in the function of interest has to be determined. There are two categories of methods for evaluating the uncertainty in a measured value; a Type A

classification includes uncertainties *"evaluated by statistical methods"* and a Type B includes uncertainty values *"evaluated by other means"* [30,31]. In this microtribometer analysis a Type B evaluation for the uncertainty in measured values will be performed. The *"other means"* used to quantify the uncertainty of each measured value is outlined for each measured parameter in this investigation.

The uncertainties of these measured values will be combined according to eqn 4.32 to find a total combined uncertainty in the friction coefficient based on the microtribometer measurement design. This approach has been successfully used by other investigators to evaluate the uncertainty of measurements made in tribological experiments [32,33].

In this combination of uncertainties the expression for the coefficient of friction at the surface (μ) will be broken down to examine how the measured values of the tribometer contribute to a quantification of the uncertainty in the friction coefficient. Figure 4-8 outlines a hierarchy of the contributions to the uncertainty in the coefficient of friction. A standard uncertainty is evaluated at each level of the hierarchy. Equation numbers used in relating parameters between levels are indicated in parentheses next to each corresponding branch. The chapter subsections of the text deriving the standard uncertainty relations between levels are indicated to the right of the hierarchy level.

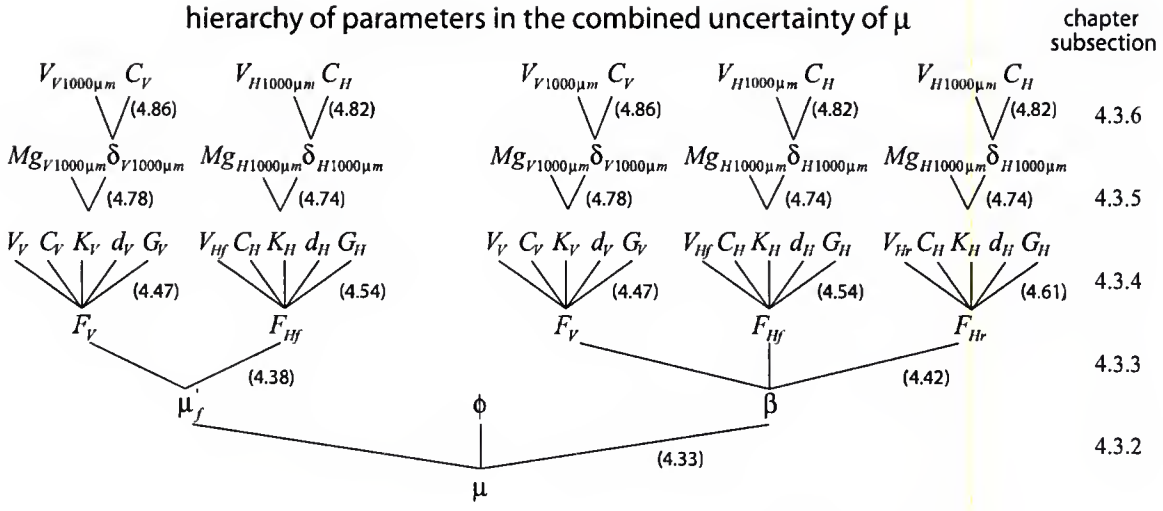

Figure 4-8 Propagation of uncertainty hierarchy.

Terminating branches on the hierarchy are measured values. Quantities and sources for those measured values are outlined in Table 4-2. Uncertainty values and sources are outlined in Table 4-3.

Table 4-2 Measured values used in the calculation of uncertainty.

symbol	value	units	source of value
ϕ	0.035	radians	user placement misalignment pitch angle
V_{Hf}	varies	V	forward horizontal flexure displacement
V_{Hr}	varies	V	reverse horizontal flexure displacement
V_V	varies	V	user prescribed applied vertical force
C_H	1249.89	um/V	distribution on supplied CSM curve
C_V	1282.63	um/V	distribution on supplied CSM curve
K_H	3.7381	mN/um	ST-027 CSM calibration certificate
K_V	2.1235	mN/um	ST-027 CSM calibration certificate
d_H	0	um	machining misalignment
d_V	0	um	machining misalignment
G_H	0	1/um	FEA analysis of flexure
G_V	-3.71E-5	1/um	FEA analysis of flexure
$Mg_{H1000\mu m}$	3738.1	mN	load for 1000μm displacement
$Mg_{V1000\mu m}$	2123.5	mN	load for 1000μm displacement
$V_{H1000\mu m}$	0.7756	V	1000μm displacement sensor voltage
$V_{V1000\mu m}$	0.7958	V	1000μm displacement sensor voltage

Table 4-3 Uncertainty in the measured values.

symbol	value	units	source of uncertainty value
$u(\phi)$	0.035	radians	best visual alignment
$u(V_{Hf})$	0.0005	V	16 bit data acquisition card
$u(V_{Hr})$	0.0005	V	16 bit data acquisition card
$u(V_V)$	0.0005	V	16 bit data acquisition card
$u(C_H)$	0.384	um/V	standard deviation of distribution
$u(C_V)$	0.408	um/V	standard deviation of distribution
$u(K_H)$	0.0026	mN/um	propagation uncertainties on eqn 4.74
$u(K_V)$	0.0015	mN/um	propagation uncertainties on eqn 4.78
$u(d_H)$	50	um	machining misalignment
$u(d_V)$	50	um	machining misalignment
$u(G_H)$	0	1/um	standard deviation of FEA analysis
$u(G_V)$	1.84E-6	1/um	standard deviation of FEA analysis
$u(Mg_{H1000\mu m})$	0.001	mN	laboratory grade scale
$u(Mg_{V1000\mu m})$	0.001	mN	laboratory grade scale
$u(V_{H1000\mu m})$	0.0005	V	16 bit data acquisition card
$u(V_{V1000\mu m})$	0.0005	V	16 bit data acquisition card

The propagation of uncertainties starts at these terminating branch measured values. At each branching location a standard uncertainty is then determined on the functional relationships (equations next to each branch in Figure 4-8). These uncertainties are propagated through each level of the hierarchy resulting in a final combined standard uncertainty in the friction coefficient. The functional relationships corresponding to each branch in the uncertainty hierarchy will now be developed based on the measurement design of the microtribometer.

4.3.2. μ: Friction Coefficient

The friction coefficient (μ) was defined in eqn 4.24.

$$\mu = \cos(\phi)\frac{\left(\mu_f' \cos\beta + \sin\beta\right)}{\left(\cos\beta - \mu_f' \sin\beta\right)} \qquad \text{eqn 4.33}$$

The variance in μ can be found according to eqn 4.32, using the law of propagation of uncertainty.

$$u_c^2(\mu) = u^2(\phi)\left(\frac{\partial\mu}{\partial\phi}\right)^2 + u^2(\beta)\left(\frac{\partial\mu}{\partial\beta}\right)^2 + u^2(\mu_f')\left(\frac{\partial\mu}{\partial\mu_f'}\right)^2 \qquad \text{eqn 4.34}$$

The partial derivatives with respect to each variable in eqn 4.33 are expressed in eqns 4.35-4.37.

$$\frac{\partial\mu}{\partial\phi} = \sin\phi\frac{\left(\mu_f'\cos\beta + \sin\beta\right)}{\left(\mu_f'\sin\beta - \cos\beta\right)} \qquad \text{eqn 4.35}$$

$$\frac{\partial\mu}{\partial\beta} = \cos\phi\frac{\left(\mu_f'^2 + 1\right)}{\left(\cos\beta - \mu_f'\sin\beta\right)^2} \qquad \text{eqn 4.36}$$

$$\frac{\partial\mu}{\partial\mu_f'} = \cos\phi\frac{1}{\left(\cos\beta - \mu_f'\sin\beta\right)^2} \qquad \text{eqn 4.37}$$

The expression for the coefficient of friction, μ, is a function of the tribometer reported forward sliding friction coefficient (μ_f') and the misalignment angles (β and ϕ). The uncertainty in each of those values is evaluated using the same application of the law of propagation of uncertainty to their formulaic expressions.

4.3.3: Friction Coefficient Expansion

4.3.3.1 ϕ: Pitch misalignment angle

The value of the inclination angle ϕ is unknown and since it acts perpendicular to the direction of sliding it cannot be solved for from the tribometer reported forward and reverse friction coefficient values (μ_f', μ_r'). An estimate of the value of the inclination

angle ϕ and the uncertainty of the inclination angle, $u(\phi)$, has to be made. A reasonable value for potential visual misalignment when placing a one inch disk sample into a set screw is assumed to be around 0.035 radians. For this reason a value of 0.035 radians is used for both ϕ and $u(\phi)$. The influence of varying the value of ϕ on the value of the uncertainty in the friction coefficient is addressed in Appendix E, but for this analysis a value of 0.035 radians is used for all calculations.

4.3.3.2 (μ_f'): Tribometer reported friction coefficient

The tribometer reported forward sliding friction coefficient is determined from the ratio of the horizontal and vertical forces read by the tribometer.

$$\mu_f' = \frac{F_{Hf}}{F_V} \qquad \text{eqn 4.38}$$

The variance in μ_f' can be found using eqn 4.39.

$$u_c^2\left(\mu_f'\right) = u^2\left(F_{Hf}\right)\left(\frac{\partial \mu_f'}{\partial F_{Hf}}\right)^2 + u^2\left(F_V\right)\left(\frac{\partial \mu_f'}{\partial F_V}\right)^2 \qquad \text{eqn 4.39}$$

The evaluated partial derivatives in eqn 4.39 are expressed in eqns 4.40 and 4.41.

$$\frac{\partial \mu_f'}{\partial F_{Hf}} = \frac{1}{F_V}, \frac{\partial \mu_f'}{\partial F_V} = -\frac{F_{Hf}}{F_V^2} \qquad \text{eqns 4.40,4.41}$$

4.3.3.3 (β): Roll misalignment angle

The sample roll misalignment angle β was established in eqn 4.31 to be a function of the forward and reverse horizontal forces (F_{Hf}, F_{Hr}) and vertical force (F_V) read by the tribometer.

$$\beta = \frac{F_V\left(F_{Hf} + F_{Hr}\right)}{2\left(F_{Hf}F_{Hr} - F_V^2\right)} \qquad \text{eqn 4.42}$$

The variance in β can be found using eqn 4.43.

$$u_c^2(\beta) = u^2\left(F_{Hf}\right)\left(\frac{\partial\beta}{\partial F_{Hf}}\right)^2 + u^2\left(F_{Hr}\right)\left(\frac{\partial\beta}{\partial F_{Hr}}\right)^2 + u^2\left(F_V\right)\left(\frac{\partial\beta}{\partial F_V}\right)^2 \qquad \text{eqn 4.43}$$

The evaluated partial derivatives in eqn 4.43 are expressed in eqns 4.44-4.46.

$$\frac{\partial\beta}{\partial F_{Hf}} = -\frac{F_V\left(F_V^2 + F_{Hr}^2\right)}{2} \qquad \text{eqn 4.44}$$

$$\frac{\partial\beta}{\partial F_{Hr}} = -\frac{F_V\left(F_V^2 + F_{Hf}^2\right)}{2\left(F_V^2 - F_{Hf}F_{Hr}\right)^2} \qquad \text{eqn 4.45}$$

$$\frac{\partial\beta}{\partial F_V} = \frac{\left(F_{Hf} + F_{Hr}\right)\left(F_{Hf}F_{Hr} + F_V^2\right)}{2\left(F_V^2 - F_{Hf}F_{Hr}\right)^2} \qquad \text{eqn 4.46}$$

Both the expression for the tribometer reported forward sliding friction coefficient (μ_f') and the roll misalignment angle (β) are functions of the forward and reverse horizontal forces (F_{Hf}, F_{Hr}) and vertical force (F_V) read by the tribometer. The uncertainty in each of those values is evaluated using the same application of the law of propagation of uncertainty to their formulaic expressions.

4.3.4. Tribometer Read Forces

4.3.4.1 (F_V): Tribometer read vertical force

The tribometer read vertical force (F_V) is a function of the vertical optical sensor voltage (V_V), the vertical displacement-voltage sensor constant (C_V), the vertical flexure stiffness (K_V), the vertical sensor-mirror mounting offset (d_V), and the vertical cantilever

slope constant (G_V). The derivation of this functional relationship will be later established through the definitions of the constants in Figure 4-10 and eqns 4.68-4.73.

$$F_V = \frac{V_V C_V K_V}{(1 - d_V G_V)} \qquad \text{eqn 4.47}$$

The variance in F_V can be found using eqn 4.48.

$$u_c^2(F_V) = u^2(V_V)\left(\frac{\partial F_V}{\partial V_V}\right)^2 + u^2(C_V)\left(\frac{\partial F_V}{\partial C_V}\right)^2 + u^2(K_V)\left(\frac{\partial F_V}{\partial K_V}\right)^2$$

$$+u^2(d_V)\left(\frac{\partial F_V}{\partial d_V}\right)^2 + u^2(G_V)\left(\frac{\partial F_V}{\partial G_V}\right)^2 \qquad \text{eqn 4.48}$$

The evaluated partial derivatives in eqn 4.48 are expressed in eqns 4.49-4.53.

$$\frac{\partial F_V}{\partial V_V} = \frac{C_V K_V}{(1 - d_V G_V)}, \frac{\partial F_V}{\partial C_V} = \frac{V_V K_V}{(1 - d_V G_V)}, \frac{\partial F_V}{\partial K_V} = \frac{V_V C_V}{(1 - d_V G_V)} \qquad \text{eqns 4.49-4.51}$$

$$\frac{\partial F_V}{\partial d_V} = \frac{V_V C_V K_V G_V}{(1 - d_V G_V)^2}, \frac{\partial F_V}{\partial G_V} = \frac{V_V C_V K_V d_V}{(1 - d_V G_V)^2} \qquad \text{eqns 4.52,4.53}$$

4.3.4.2 (F_{Hf}): Tribometer read forward sliding horizontal force

The tribometer read horizontal force when sliding in the forward direction (F_{Hf}) is a function of the horizontal forward sliding optical sensor voltage (V_{Hf}), the horizontal displacement-voltage sensor constant (C_H), the horizontal flexure stiffness (K_H), the horizontal sensor-mirror mounting offset (d_H), and the horizontal cantilever slope constant (G_H).

$$F_{Hf} = \frac{V_{Hf} C_H K_H}{(1 - d_H G_H)} \qquad \text{eqn 4.54}$$

The variance in F_{Hf} can be found using eqn 4.55.

$$u_c^2(F_{Hf}) = u^2(V_{Hf})\left(\frac{\partial F_{Hf}}{\partial V_{Hf}}\right)^2 + u^2(C_H)\left(\frac{\partial F_{Hf}}{\partial C_H}\right)^2 + u^2(K_H)\left(\frac{\partial F_{Hf}}{\partial K_H}\right)^2$$

$$+u^2(d_H)\left(\frac{\partial F_{Hf}}{\partial d_H}\right)^2 + u^2(G_H)\left(\frac{\partial F_{Hf}}{\partial G_H}\right)^2 \qquad \text{eqn 4.55}$$

The evaluated partial derivatives in eqn 4.55 are expressed in eqns 4.56-4.60.

$$\frac{\partial F_{Hf}}{\partial V_{Hf}} = \frac{C_H K_H}{(1-d_H G_H)}, \frac{\partial F_{Hf}}{\partial C_H} = \frac{V_{Hf} K_H}{(1-d_H G_H)}, \frac{\partial F_{Hf}}{\partial K_H} = \frac{V_{Hf} C_H}{(1-d_H G_H)} \qquad \text{eqns 4.56-4.58}$$

$$\frac{\partial F_{Hf}}{\partial d_H} = \frac{V_{Hf} C_H K_H G_H}{(1-d_H G_H)^2}, \frac{\partial F_{Hf}}{\partial G_H} = \frac{V_{Hf} C_H K_H d_H}{(1-d_H G_H)^2} \qquad \text{eqns 4.59,4.60}$$

4.3.4.3 (F_{Hr}): Tribometer read reverse sliding horizontal force

The tribometer read horizontal force when sliding in the reverse direction (F_{Hr}) is a function of the horizontal reverse sliding optical sensor voltage (V_{Hr}), the horizontal displacement-voltage sensor constant (C_H), the horizontal flexure stiffness (K_H), the horizontal sensor-mirror mounting offset (d_H), and the horizontal cantilever slope constant (G_H).

$$F_{Hr} = \frac{V_{Hr} C_H K_H}{(1-d_H G_H)} \qquad \text{eqn 4.61}$$

The variance in F_{Hr} can be found using eqn 4.62.

$$u_c^2(F_{Hr}) = u^2(V_{Hr})\left(\frac{\partial F_{Hr}}{\partial V_{Hr}}\right)^2 + u^2(C_H)\left(\frac{\partial F_{Hr}}{\partial C_H}\right)^2 + u^2(K_H)\left(\frac{\partial F_{Hr}}{\partial K_H}\right)^2$$

$$+u^2(d_H)\left(\frac{\partial F_{Hr}}{\partial d_H}\right)^2 + u^2(G_H)\left(\frac{\partial F_{Hr}}{\partial G_H}\right)^2 \qquad \text{eqn 4.62}$$

The evaluated partial derivatives in eqn 4.62 are expressed in eqns 4.63-4.67.

$$\frac{\partial F_{Hr}}{\partial V_{Hr}} = \frac{C_H K_H}{(1 - d_H G_H)}, \frac{\partial F_{Hr}}{\partial C_H} = \frac{V_{Hr} K_H}{(1 - d_H G_H)}, \frac{\partial F_{Hr}}{\partial K_H} = \frac{V_{Hr} C_H}{(1 - d_H G_H)} \quad \text{eqns 4.63-4.65}$$

$$\frac{\partial F_{Hr}}{\partial d_H} = \frac{V_{Hr} C_H K_H G_H}{(1 - d_H G_H)^2}, \frac{\partial F_{Hr}}{\partial G_H} = \frac{V_{Hr} C_H K_H d_H}{(1 - d_H G_H)^2} \quad \text{eqns 4.66,4.67}$$

4.3.5 Force Expansion

4.3.5.1 (V): Optical sensor voltage

The magnitude of the voltage read by the optical sensors in the horizontal (V_H) and vertical (V_V) directions are functions of the applied normal load and reacted frictional forces. The uncertainty in the values of the optical sensor voltages, $u(V_H)$ and $u(V_V)$, is bounded by the resolution of the tribometer data acquisition card. The tribometer uses a 16 bit data acquisition card (DT322). At a 10 V range this results in a minimum increment of 0.15 mV on the voltage signal. The uncertainty in the voltage in each direction is taken as approximately three times this number; $u(V_H) = u(V_V) \sim 0.5$ mV.

4.3.5.2 (C): Displacement-Voltage calibration constant

The horizontal and vertical optical sensor displacement-voltage calibration constants, C_H, and C_V, are determined from manufacturer supplied voltage-displacement curves. The optical sensors are designed to be used over two different distance ranges. The low range (0-100 μm displacement) is used for a higher signal sensitivity in the low displacement (low force range on each flexure). The high range (0-1000 μm displacement) is used to cover the full range of displacement of the flexures (highest force range on each flexure). All tests in this study were executed with the optical

sensors in the high displacement range. A schematic of the distance operating ranges and the supplied calibration constant curves is shown in Figure 4-9. The values for the horizontal and vertical voltage-displacement calibration constants were determined from the 300 μm to 900 μm portions of the manufacturer supplied calibration curves. Values for C_H and C_V were estimated from a normal distribution of values around this range of the calibration curves and the uncertainty values, $u(C_H)$ and $u(C_V)$, from the standard deviation of that distribution.

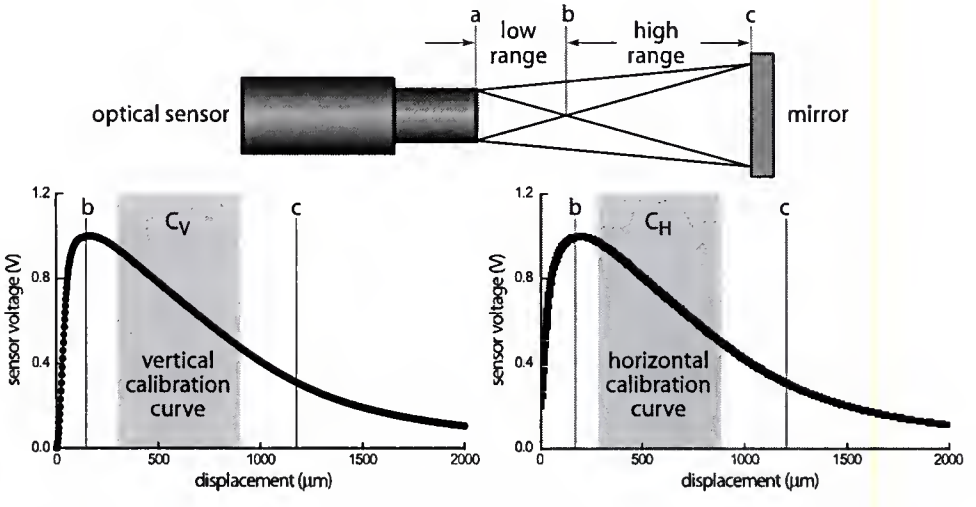

Figure 4-9 Operating ranges and calibration curves for optical sensors.

4.3.5.3 (d, G): Mounting offset error and calibration slope constant

In addition to the optical sensor voltage ($V_{V,H}$) and the displacement-voltage sensor constant ($C_{V,H}$), the tribometer read vertical and horizontal forces ($F_{V,H}$) are influenced by the sensor-mirror mounting offset error ($d_{V,H}$), and the cantilever slope constant ($G_{V,H}$). Figure 4-10 shows a schematic of the influence of the mounting offset error ($d_{V,H}$) and the derivation of the slope constant ($G_{V,H}$).

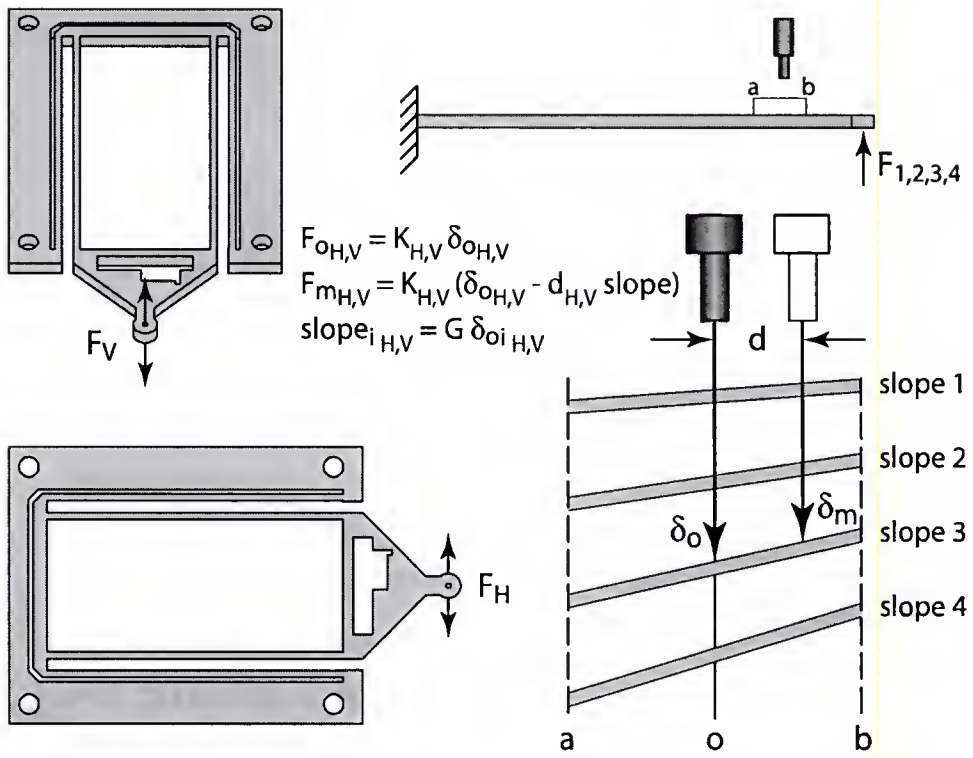

Figure 4-10 Schematic analysis to find the mounting offset error ($d_{V,H}$) and slope constant ($G_{V,H}$).

The relations outlined in Figure 4-10 are used to derive eqns 4.47, 4.54, and 4.61. Following the schematic in Figure 4-10, the force that would be measured by the optical sensor ($F_{oV,H}$) if the mounting offset error were zero is the stiffness of the cantilever times the deflection at that point.

$$F_{oV,H} = K_{V,H}\delta_{oH,V} \qquad \text{eqn 4.68}$$

If the mirror and optical sensor are misaligned by $d_{V,H}$ the measured force (F_m) becomes a function of the zero offset deflection the offset error and the cantilever slope under that deflection.

$$F_{mV,H} = K_{V,H}\left(\delta_{oH,V} - d_{H,V}slope\right) \qquad \text{eqn 4.69}$$

The sensor-mirror mounting offset error, $d_{V,H}$, value is set to zero. This is done because the tribometer is designed to try to have the mirror and optical sensors align in

the same centralized location each time the carrier block is mounted into the housing. The uncertainty in the sensor mirror offset $u_c(d_{V,H})$ is given a value of 50 μm based on machining tolerances believed to be used in the manufacturing of the carrier block and housing [34].

Finite element analysis was performed on the flexure used in these experiments to investigate the influence of applied load on the slope of the flexure at the mirror. In a similar manner to the schematic in Figure 4-10, the end of each flexure was given a fixed boundary condition. Four different simulated loads were applied in the vertical and horizontal directions. The deflection of the flexure was measured at four points along the mirror location to establish the slope of the flexure under each applied load. The slopes of the flexures were examined as a function of the zero error point deflection. This examination showed that for a given direction on a single flexure the value of the slope defined in Figure 4-10 is a constant multiple ($G_{V,H}$) of the zero error point deflection (δ_o). This value of ($G_{V,H}$) is constant for a single direction on a particular flexure.

$$slope = \delta_o G_{H,V} \qquad \text{eqn 4.70}$$

This expression can be substituted into eqn 4.69.

$$F_{mV,H} = K_{V,H}\left(\delta_{oH,V} - d_{H,V}\delta_o G_{H,V}\right) \qquad \text{eqn 4.71}$$

Substituting eqn 4.68 into eqn 4.71 yields an expression for the measured force.

$$F_{mV,H} = F_o\left(1 - d_{H,V}G_{H,V}\right) \qquad \text{eqn 4.72}$$

The force measured by the tribometer in the vertical and horizontal directions is the product of the optical sensor voltage ($V_{V,H}$), the displacement-voltage sensor constant ($C_{V,H}$), and the flexure stiffness ($K_{V,H}$).

$$F_{V,H} = \frac{F_{mV,H}}{\left(1 - d_{V,H} G_{V,H}\right)} = \frac{V_{V,H} C_{V,H} K_{V,H}}{\left(1 - d_{V,H} G_{V,H}\right)} \qquad \text{eqn 4.73}$$

Eqn 4.73 is the same functional form as the relations used in eqns 4.47, 4.54, and 4.61.

4.3.5.4 (K): Flexure stiffness

A calibration certificate is supplied by the manufacturer with values for horizontal and vertical cantilever stiffness values (K_H, K_V). For this uncertainty analysis the manufacturer provided values of stiffness are used. These values are also entered into the software interface any time a new flexure is used. These stiffness values are manufacturer calculated by mounting each flexure into a similarly designed housing to that used in the tribometer (Figure 4-3). Known masses are hung from the flexure and the deflection at the mirror is measured using the same type of optical light intensity sensor as it in the tribometer. This manufacturer calibration method is examined to determine the uncertainty in the stiffness values. The maximum measurement displacement for the optical sensors is 1000 μm. The horizontal stiffness is found by applying the maximum force ($Mg_{H1000\mu m}$) that would cause the maximum measurable horizontal displacement ($\delta_{H1000\mu m}$).

$$K_{H1000\mu m} = \frac{Mg_{H1000\mu m}}{\delta_{H1000\mu m}} \qquad \text{eqn 4.74}$$

The variance in the K_H expression can be found using eqn 4.74.

$$u_c^2\left(K_{H1000\mu m}\right) = u^2\left(Mg_{H1000\mu m}\right)\left(\frac{\partial K_{H1000\mu m}}{\partial Mg_{H1000\mu m}}\right)^2 + u^2\left(\delta_{H1000\mu m}\right)\left(\frac{\partial K_{H1000\mu m}}{\partial \delta_{H1000\mu m}}\right)^2 \qquad \text{eqn 4.75}$$

The evaluated partial derivatives in eqn 4.75 are expressed in eqns 4.76 and 4.77.

$$\frac{\partial K_{H1000\mu m}}{\partial Mg_{H1000\mu m}} = \frac{1}{\delta_{H1000\mu m}}, \frac{\partial K_{H1000\mu m}}{\partial \delta_{H1000\mu m}} = -\frac{Mg_{H1000\mu m}}{\delta^2_{H1000\mu m}} \quad \text{eqns 4.76,4.77}$$

The vertical stiffness is similarly found by applying the maximum force ($Mg_{V1000\mu m}$) that would cause the maximum measurable vertical displacement ($\delta_{V1000\mu m}$).

$$K_{V1000\mu m} = \frac{Mg_{V1000\mu m}}{\delta_{V1000\mu m}} \quad \text{eqn 4.78}$$

The variance in the K_V expression can be found using eqn 4.78.

$$u_c^2\left(K_{V1000\mu m}\right) = u^2\left(Mg_{V1000\mu m}\right)\left(\frac{\partial K_{V1000\mu m}}{\partial Mg_{V1000\mu m}}\right)^2 + u^2\left(\delta_{V1000\mu m}\right)\left(\frac{\partial K_{V1000\mu m}}{\partial \delta_{V1000\mu m}}\right)^2 \quad \text{eqn 4.79}$$

The evaluated partial derivatives in eqn 4.79 are expressed in eqns 4.80 and 4.81.

$$\frac{\partial K_{V1000\mu m}}{\partial Mg_{V1000\mu m}} = \frac{1}{\delta_{V1000\mu m}}, \frac{\partial K_{V1000\mu m}}{\partial \delta_{V1000\mu m}} = -\frac{Mg_{V1000\mu m}}{\delta^2_{V1000\mu m}} \quad \text{eqns 4.80,4.81}$$

4.3.6 Stiffness Expansion

4.3.6.1. (Mg): Calibration force

The value for the calibration force used in eqns 4.74-4.81 is the force that would cause a 1000μm displacement based on the stiffness of the flexure. The uncertainty in this force value u($Mg_{H,V}$) is taken as 1μN which is the resolution of a laboratory grade scale.

4.3.6.2 (δ): Calibration displacement

The uncertainty in delta is determined from the displacement-voltage calibration constant and the sensor voltage at a 1000 μm displacement.

$$\delta_{H1000\mu m} = C_H V_{H1000\mu m} \quad \text{eqn 4.82}$$

The variance in δ_H can be found using eqn 4.82.

$$u_c^2\left(\delta_{H1000\mu m}\right)=u^2\left(C_H\right)\left(\frac{\partial\delta_{H1000\mu m}}{\partial C_H}\right)^2+u^2\left(V_{H1000\mu m}\right)\left(\frac{\partial\delta_{H1000\mu m}}{\partial V_{H1000\mu m}}\right)^2 \qquad \text{eqn 4.83}$$

The evaluated partial derivatives in eqn 4.83 are expressed in eqns 4.84 and 4.85.

$$\frac{\partial\delta_{H1000\mu m}}{\partial C_H}=V_{H1000\mu m},\frac{\partial\delta_{H1000\mu m}}{\partial V_{H1000\mu m}}=C_H \qquad \text{eqns 4.84,4.85}$$

This procedure is repeated for the vertical displacement delta.

$$\delta_{V1000\mu m}=C_V V_{V1000\mu m} \qquad \text{eqn 4.86}$$

The variance in δ_V can be found using eqn 4.86.

$$u_c^2\left(\delta_{V1000\mu m}\right)=u^2\left(C_V\right)\left(\frac{\partial\delta_{V1000\mu m}}{\partial C_V}\right)^2+u^2\left(V_{V1000\mu m}\right)\left(\frac{\partial\delta_{V1000\mu m}}{\partial V_{V1000\mu m}}\right)^2 \qquad \text{eqn 4.87}$$

The evaluated partial derivatives in eqn 4.87 are expressed in eqns 4.88 and 4.89.

$$\frac{\partial\delta_{V1000\mu m}}{\partial C_V}=V_{V1000\mu m},\frac{\partial\delta_{V1000\mu m}}{\partial V_{V1000\mu m}}=C_V \qquad \text{eqns 4.88,4.89}$$

Each one of the uncertainties in the measured values is then propagated through their relations according to Figure 4-8. This standard procedure is used to find the friction coefficient, μ, and the uncertainty in the friction coefficient $u_c(\mu)$ for any reciprocating test run on the microtribometer.

This analysis allows for the uncertainty in the friction coefficient to be evaluated over a range of combinations of normal loads and friction coefficient values that may be realized during testing. This uncertainty space can be displayed graphically using plots of lines of constant uncertainty in the friction coefficient as a function of friction coefficient and applied normal load, as shown in Figure 4-11.

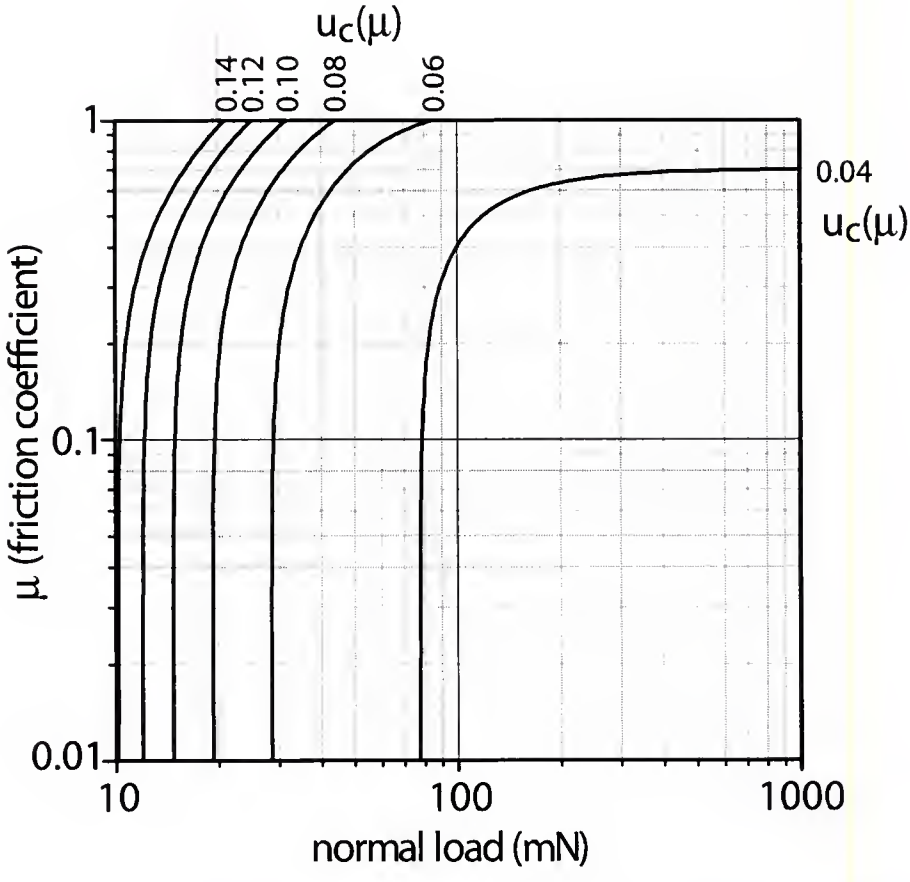

Figure 4-11 Lines of constant uncertainty in the friction coefficient.

The uncertainty in the friction coefficient in Figure 4-11 is a strong function of applied normal load. Lower applied normal loads lead to more uncertainty in the signal. This is correlated to the fact that at lighter loads there is a smaller voltage signal being returned from the optical sensors to the data acquisition card. The uncertainty in the friction coefficient due to the voltage becomes larger as the overall voltage used to determine displacements gets smaller.

Another way to examine the uncertainty space over a range of normal load and friction coefficient values is to look at lines of constant uncertainty in friction coefficient over the friction coefficient value ($u_c(\mu)/\mu$). This is shown in Figure 4-12 over the same

load and friction coefficient range. These lines show the relative magnitude of the uncertainty in the friction coefficient to the friction coefficient value.

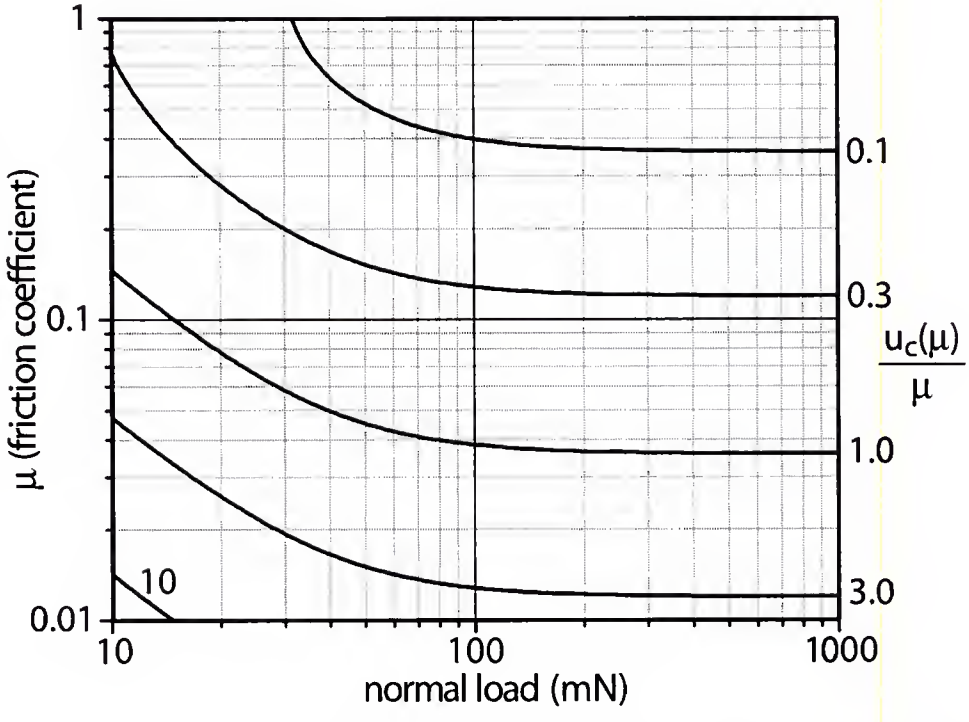

Figure 4-12 Lines of constant uncertainty in friction coefficient over the friction coefficient.

It can be seen that at low friction coefficient values and low loads the uncertainty in the friction coefficient can be up to 1000 times the magnitude of the friction coefficient itself. One thing to note in Figure 4-12 is above approximately 100 mN of normal load the ratio of $u_c(\mu)/\mu$ becomes relatively independent of applied normal load. This trend can be explained if the same load region is examined in Figure 4-11. Above the 100 mN mark in Figure 4-11 the uncertainty in friction coefficient stays relatively constant at around $u_c(\mu) = 0.04$, so the ratio of $u_c(\mu)/\mu$ only becomes a function of the friction coefficient value itself and not the applied normal load.

Figure 4-13 explores the contributors to the uncertainty value by examining one set of data from self-mated NFC films (Chapter 6) and quantifying the relative contributors to the variance.

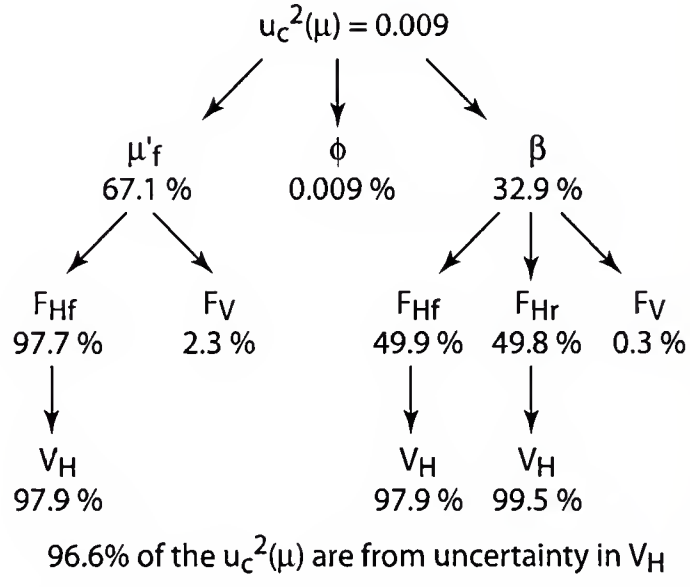

Figure 4-13 Relative contributions to the variance in the friction coefficient.

The major contributor (96.6%) to the square of the uncertainty in the friction coefficient is due to the voltage signal and uncertainty in the voltage signal. The uncertainty in the friction coefficient could be greatly reduced if the quality of this voltage signal was improved. One way that the voltage signal could be improved would be to expand the range of the signal from the optical senor by expanding the voltage range the sensor operates over. Currently for an average test the magnitude of the voltage signal under a 500 mN load changes by approximately 0.6 V. For a material with a friction coefficient of 0.01the friction signal will only vary by 0.006 V. It becomes very difficult to resolve these very small changes in voltage when the uncertainty in the voltage signal itself is 0.0005 V. The expansion of the operating range of voltages could

be achieved through either amplifying the voltage signal to the data acquisition card or using a different displacement sensor that has a more expansive voltage operating range. These potential improvements were not implemented as part of this investigation.

The magnitude of uncertainty in friction coefficient on the low-friction values seen in self mated NFC testing may be quite significant. Bars signifying one standard uncertainty based on the formulas developed in this chapter are included on data in Chapter 6 of this work. In Chapter 6 the significance of this uncertainty interval is discussed in more detail. The uncertainty analysis and friction coefficient equations developed in this chapter can now be used to transfer reciprocating forward and reverse friction coefficient data as it comes from the tribometer into a bias corrected friction coefficient value, the uncertainty in that value and the misalignment roll angle the counterface was situated at during testing. Chapter 5 of this work will now examine some preliminary testing of NFC films on this low contact pressure tribometer. The uncertainty analysis derived in this chapter is not applied to the preliminary data in Chapter 5, but is used on the more tailored experiments of Chapter 6.

CHAPTER 5
INITIAL ENVIRONMENTAL TRIBOLOGY OF NFC FILMS

The low contact pressure tribometer was used to investigate the environmental dependence of friction coefficient of self-mated NFC films. Self-mated is defined as both the pin and the counterface samples being coated with near frictionless carbon. The pin sample used in these tests is a borosilicate crown glass with a 7.78 mm radius of curvature. The counterface sample is a 1 mm thick microscopy slide. Both the pin and the counterface were coated with NFC. Surface scans (Figure 5-1) of the samples were performed using a WYKO white light interferometer.

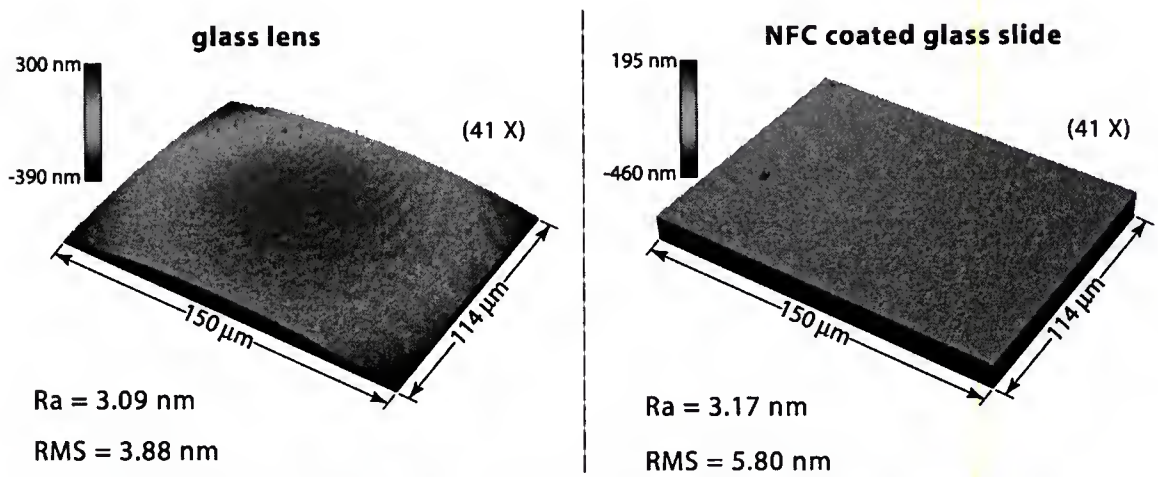

Figure 5-1 Surface scans of uncoated pin sample and coated flat sample.

These surface scans show the NFC coating has an average roughness of approximately 3.2 nm.

5.1 Near Frictionless Carbon Run-In Testing

The first series of experiments run on the low contact pressure tribometer were to look at the frictional properties of the surface of the NFC films. Other investigators have used neutron reflectivity to determine that the as-deposited NFC films are composed of two layers, an approximately 30Å thick higher density surface layer with the remainder or the coating being of lower density [35]. Friction coefficient tests were run with a self-mated NFC pair in a dry argon gas environment. An initial run-in test was performed in which the self-mated pair were run against one another at 18 mm/s, under a 100 mN normal load over a 0.6 mm reciprocating path. This test was run until the surfaces "ran-in" to a steady state low friction coefficient.

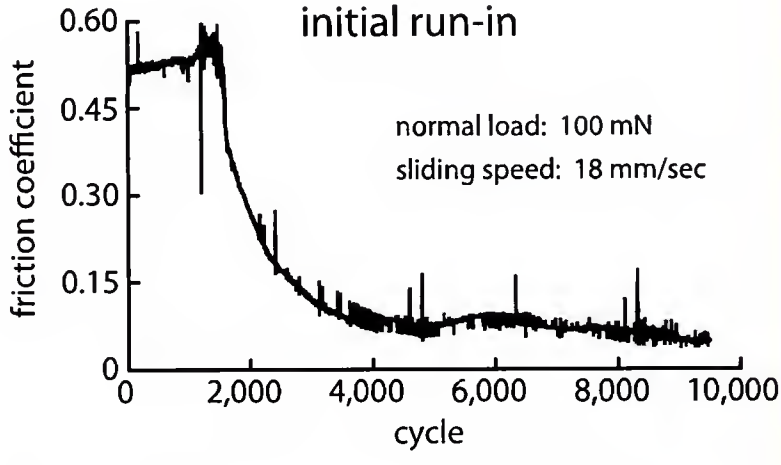

Figure 5-2 Initial run-in of two unworn self-mated NFC samples in a dry argon environment.

It is interesting that the friction coefficient of the as deposited films started at μ~0.5, which is a traditionally very high friction coefficient value for self mated NFC films in a dry environment. Only after 1500-2000 cycles of sliding in dry argon did the self mated NFC pair run-in to a low friction value. There is a standing hypothesis based on neutron

reflectivity data saying the as-deposited NFC coatings are comprised of two layers (a thinner high-density surface layer followed by a lower density lower layer) [35]. Initial calculations for the experiment in Figure 5-2 show that approximately 0.09 J of frictional energy are put into the contact during the initial 1500 cycles of higher friction sliding. (Appendix F). The amount of energy required to break the bonds associated with the as-deposited higher density surface layer is estimated as 8μJ, so the initial higher friction cycles should have put more than enough energy into the contact to break through the higher friction layer (Appendix F).

To investigate if this higher friction surface layer re-forms a series of tests was run in the same wear track as the experiment in Figure 5-2, without breaking the dry argon environment. A standard test consisting of 1000 cycles at 5 mm/s, under 3 mN of load, over a 0.6 mm track length was run on the same track. Then periods of dwell were instituted between this standard test where the pin and flat sample were separated from one another but remained in the argon environment. The periods of dwell between standard tests were varied randomly by orders of magnitude from 1 minute to 10,000 minutes. The friction coefficient run-in of each of these standard tests after varying amount of times of exposure to the inert environment were examined to see if there was evidence of the surface layer re-forming or environmental species adsorbing on the surface. Plots of the friction coefficient trends after the periods of dwell for each standard test are shown in Figure 5-3.

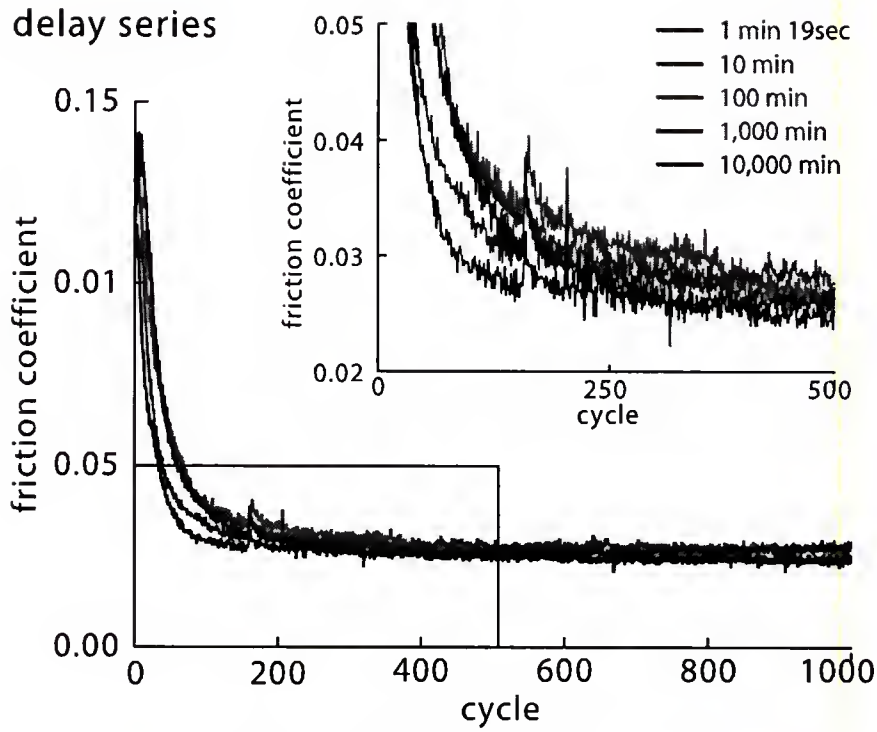

Figure 5-3 Environment exposure dwell experiments.

The first item to note for all of the standard experiments, regardless of delay time, the initial friction coefficient value begins at approximately μ=0.13. This value is close to the longest exposure time steady state friction coefficient seen by Heimberg *et al.*[9]. Additionally, this value is both lower than the initial friction coefficient of the as deposited NFC run-in test (μ=0.52) and unlike the initial run-in test, quickly dropped down to reach a steady state low friction coefficient value. It is also observed that over all dwell times the amount of time to reach a low steady state friction coefficient value was approximately equal. It appears that even after 10,000 minutes in a dry argon environment no surface layer like the initial as-deposited layer re-forms on the NFC, and whatever adsorbents or interactions that do occur on the surface are quickly overcome regardless of the amount of exposure time they have to form.

5.2 Sample Pair and Humidity Variation Experiments

A preliminary series of experiments is examined and discussed in Appendix G that consisted of varying the normal load, sliding speed and reciprocating track length to try to find the range of test conditions under which a self mated NFC pair would realize both low friction values and free sliding between the pin and flat samples. These preliminary tests show for self mated NFC samples in dry argon the optimal operating conditions for a combination of low friction coefficient and free sliding of the samples with the low pressure tribometer are at speeds above 1.89 mm/s, reciprocating track lengths above 0.3mm, and loads above 300 mN.

After more optimal test conditions were found three additional test matrices were run. The first was a NFC coated pin against a NFC coated flat in a dry argon environment (Appendix H), the second was an uncoated pin against a NFC coated flat in dry argon (Appendix I) and the third was a NFC coated pin against a NFC coated flat in a humid argon environment (Appendix J). Details and discussions on each of these three sets of experiments are included in their respective appendices; the results are briefly described here. The summary of the test conditions for these three series of test is shown in Figure 5-4.

NFC-NFC dry Ar dry argon (<5 ppm O_2, H_2O) oxygen meter	7.78 mm radius of curvature borosilicate glass pin coated with NFC6 1mm thick glass microscope slide coated with NFC6	normal load [mN] = 100, 200, 300 max Hertzian [MPa] = 70, 89, 106 sliding speed [mm/s] = 1,2,4,5,8,9,10 track length [mm] = 0.3, 0.6 number of cycles = 400
glass-NFC dry Ar dry argon (<5 ppm O_2, H_2O) oxygen meter	7.78 mm radius of curvature borosilicate glass pin 1mm thick glass microscope slide coated with NFC6	normal load [mN] = 100, 200, 300 max Hertzian [MPa] = 77, 97, 115 sliding speed [mm/s] = 1,2,4,5,8,9,10 track length [mm] = 0.3, 0.6 number of cycles = 400
NFC-NFC humid Ar argon and H_2O (<5 ppm O_2) oxygen meter	7.78 mm radius of curvature borosilicate glass pin coated with NFC6 1mm thick glass microscope slide coated with NFC6	normal load [mN] = 100, 200, 300 max Hertzian [MPa] = 70, 89, 106 sliding speed [mm/s] = 1,2,4,5,8,9,10 track length [mm] = 0.3, 0.6 number of cycles = 400

Figure 5-4 Test conditions for the three matrix series.

The first matrix of tests was a self-mated NFC pair in a dry argon environment. In examining the steady state friction coefficient data there was no apparent trend in the data with load, speed or length. In most cases the friction coefficient of the self mated pair in dry argon averaged μ=0.01. This value is fairly low and shows under the range of experimental conditions in this matrix low friction was sustained and the NFC pair did not experience any surface adsorption or interaction that interrupted the low friction regime. The second test matrix in this series consisted of an uncoated borosilicate glass pin on a NFC coated sample in a dry argon environment. This data also showed no trend for steady state friction coefficient as a function of load, speed or track length. For the majority of the tests the steady state friction was slightly higher (μ=0.015) than in the self mated NFC pair in dry argon. It is surprising that for a glass-NFC pair in dry argon the friction coefficient is similar to the low friction value seen for the NFC-NFC pair in dry argon. The third matrix of tests in this series consisted of a self-mated pair of NFC films

in an argon environment with water vapor added to achieve 10% relative humidity. This data also showed no trend for steady state friction coefficient as a function of load, speed or track length. The average steady state friction coefficient (μ=0.35) was higher than both the self mated NFC pair and glass pin with NFC flat pair in dry argon.

While there were no model correlating trends in friction coefficient, one interesting aspect of these series of tests were the pin surfaces after the experiments. Interferometer surface scans (Figure 5-5) of the wear scars on the pin samples were taken after each of the three test matrices to ensure that the NFC coating was still present and to investigate whether or not transfer films formed.

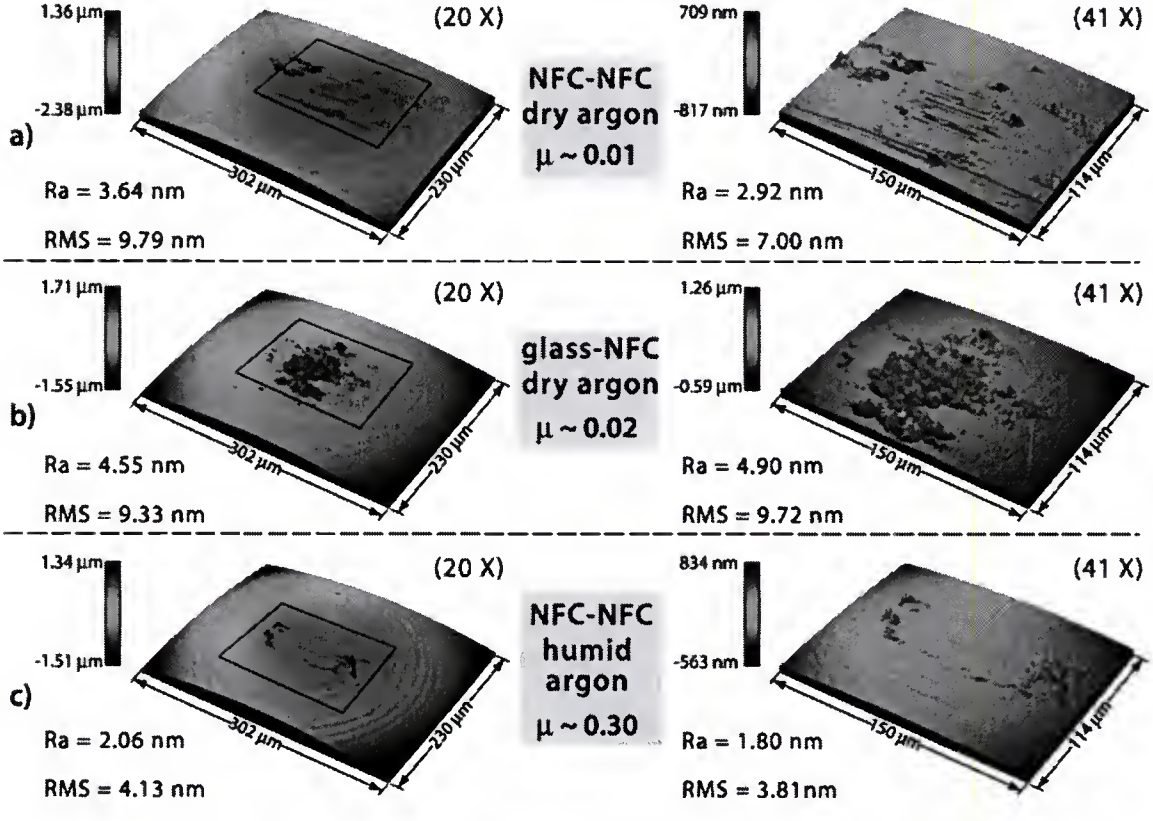

Figure 5-5 Surface scans of pin samples after a) self mated NFC tests in dry argon, b) glass pin against a NFC coated counterface in dry argon, and c) self mated NFC tests in humid argon.

For the self mated series of test run in dry argon the surface of the pin showed a small amount of wear in the sliding direction, but it was not quantifiable (Figure 5-5a). In the case of the glass pin against the NFC counterface, there seemed to be material deposited on the glass pin (Figure 5-5b). The composition of material was not analyzed. It is possible that some of the NFC coating on the counterface was transferred to the glass pin and the low friction coefficient values realized in this pairing were actually due to a layer of NFC on the glass pin rubbing against the NFC coated flat. The self-mated NFC run in humid argon pin sample also showed deposition onto the pin surface (Figure 5-5c). The nature of this material appears to be a smooth, almost smeared layer in the direction of pin sliding. It is possible that this deposited material is a transfer layer, but no chemical composition analysis was performed. These NFC experiments did not show friction coefficient to be a function of exposure time (through sliding speed and track length variations) as predicted by modeling in Chapter 2, but they did show a frictional dependence on the humidity level in the environmental chamber. This result is investigated further using a humidity ramp in the environmental chamber.

5.3 Water Vapor Ramp

The NFC-NFC humid argon experiments performed isolated water vapor as a specific species responsible for a rise in the friction coefficient of self mated NFC films. If gas-surface adsorption and removal of water vapor is occurring the low friction state should be a recoverable function of chamber humidity. To test this hypothesis an experiment was run in which the environment starts as dry argon and the friction coefficient was allowed to run-in to a low value. Then the amount of water vapor was

ramped up and back down to see how the friction coefficient behaved to a prescribed change in relative humidity of the chamber. Figure 5-6 shows friction coefficient performance for the prescribed variation of humidity within an argon environment.

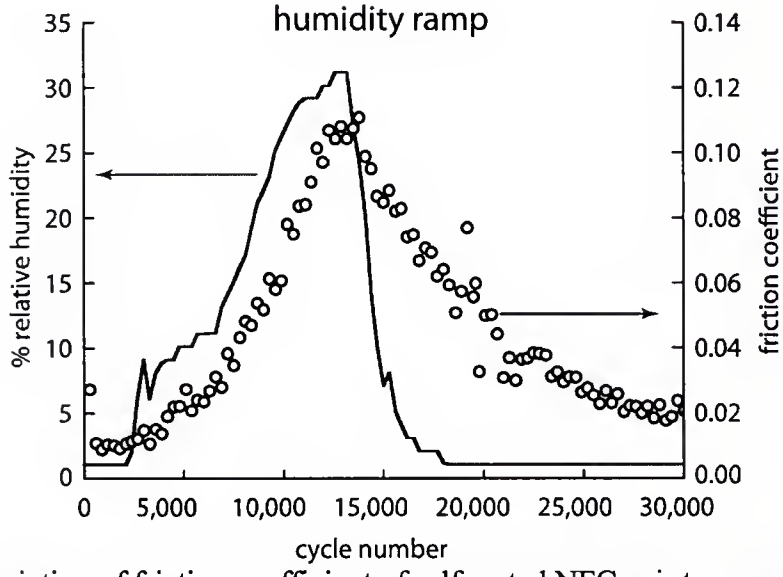

Figure 5-6 Variation of friction coefficient of self mated NFC pair to a prescribed change in relative humidity of an argon environment.

This test clearly shows that water vapor is a species that affects the friction coefficient of self mated NFC films. While this data does not indicate the specific role water plays in the friction coefficient performance, the shape of the curves in Figure 5-6 shows an interesting trend. When humidity is increased there is a slight offset to the increase in friction coefficient, but the two increasing curves are the same general shape. However, when the humidity is ramped back down the friction coefficient does drop, but at a slower rate than the humidity level drops. This could be an indication that a layer has adsorbed or interacted with the sample surfaces that may take a certain amount of time, pin interaction, or environmental composition before it can be removed or desorbed.

The tribological testing in this chapter did distinguish an initial higher friction surface layer on the as-deposited NFC coatings from the lower friction layer established

after run-in. Additionally, the experiments in this chapter isolated water vapor as a gaseous species that has a detrimental influence on the friction coefficient of self-mated NFC films in a tribological contact. However, these self-mated NFC experiments did not show friction coefficient to be a function of exposure time (through sliding speed and track length variations) as predicted by modeling in Chapter 2. This may be due to the range of sliding speeds and track lengths chosen for the experiments. An additional experimental parameter that can be controlled during tribological testing is counterface temperature. Temperature is a commonly varied parameter to look for trends in gas-surface interactions. A series of experiments varying chamber water vapor pressure and counterface surface temperature is investigated in Chapter 6 to see if trends in friction coefficient can be correlated to activation energies for competitive rates of water adsorption and desorption on the NFC coating surfaces.

CHAPTER 6
WATER VAPOR PRESSURE AND SUBSTRATE TEMPERATURE EFFECTS

Experiments in the previous chapter isolated water vapor as the environmental species causing a rise in friction coefficient of self mated NFC tribological pairs. This chapter will execute a series of experiments varying chamber water vapor pressure and NFC counterface surface temperature in an attempt to determine if water vapor is interacting with the NFC by surface adsorption. Frictional trends with prescribed variations in these two experimental parameters will be compared with modeling using Langmuir expressions for adsorption and desorption of water vapor on surfaces.

6.1 Water Vapor and Surface Temperature Experiments

The water vapor pressure of the environmental chamber was controlled by mixing prescribed amounts of dry and humidified argon, while maintaining less than 10 ppm O_2 during all tests. Counterface surface temperatures were prescribed through a PID controller using an encapsulated heater under the counterface and an adhesive thermocouple on the sample surface. A schematic of this setup was illustrated in Figure 4-2.

A single self-mated NFC coated pin and counterface sample was used for the entire matrix of experiments in this section. The pin sample consisted of a 7.78 mm radius of curvature NFC coated borosilicate glass lens and the counterface was a NFC coated microscopy slide. An initial run-in test, similar to the one in Figure 5-2 was performed to

remove the initial higher friction surface layer and achieve low-friction between the pin counterface surfaces. The water vapor pressure and temperature experiments were then all executed in the same wear track as the initial run-in test. The matrix for this series consisted of four individual experiments. During each experiment the chamber water vapor pressure was held at a distinct prescribed value, ranging from 123 Pa to 4933 Pa of vapor pressure. Each vapor pressure experiment consisted of 32,000 cycles of sliding under a 100 mN normal load, at 18 mm/sec, over a 0.6 mm track length. The experimental matrix is outlined in Figure 6-1.

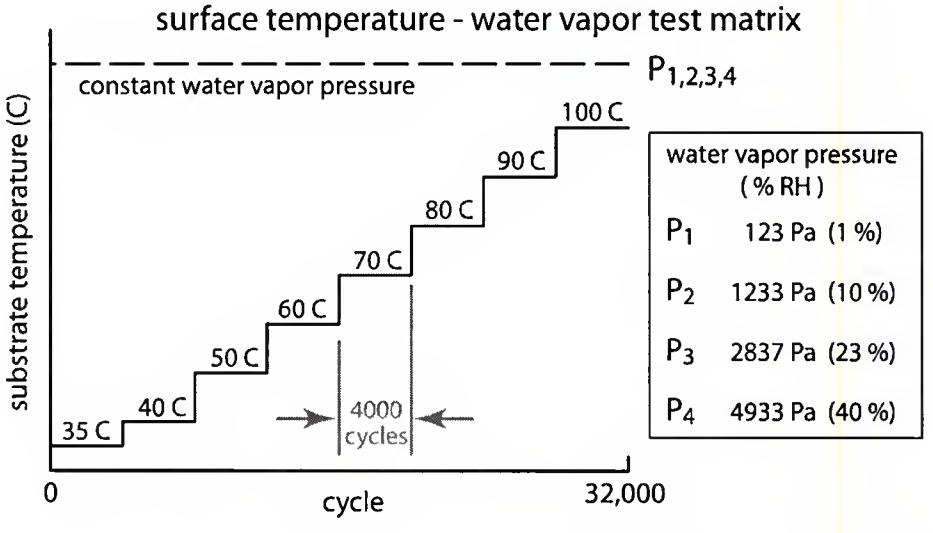

Figure 6-1 Experimental matrix for variations of chamber vapor pressure and NFC temperature.

The counterface surface temperature was held for 4,000 cycles of sliding at eight distinct temperatures during each experiment. The friction coefficient values examined from the four water vapor pressure experiments were average values from cycles 3,500-4,000 at each temperature step. Steady state friction coefficient values were determined by averaging over the middle third of the reciprocation length (to discard reversal

locations) for the last 500 cycles of sliding. The results of these experiments are examined for each water vapor pressure in Figure 6-2.

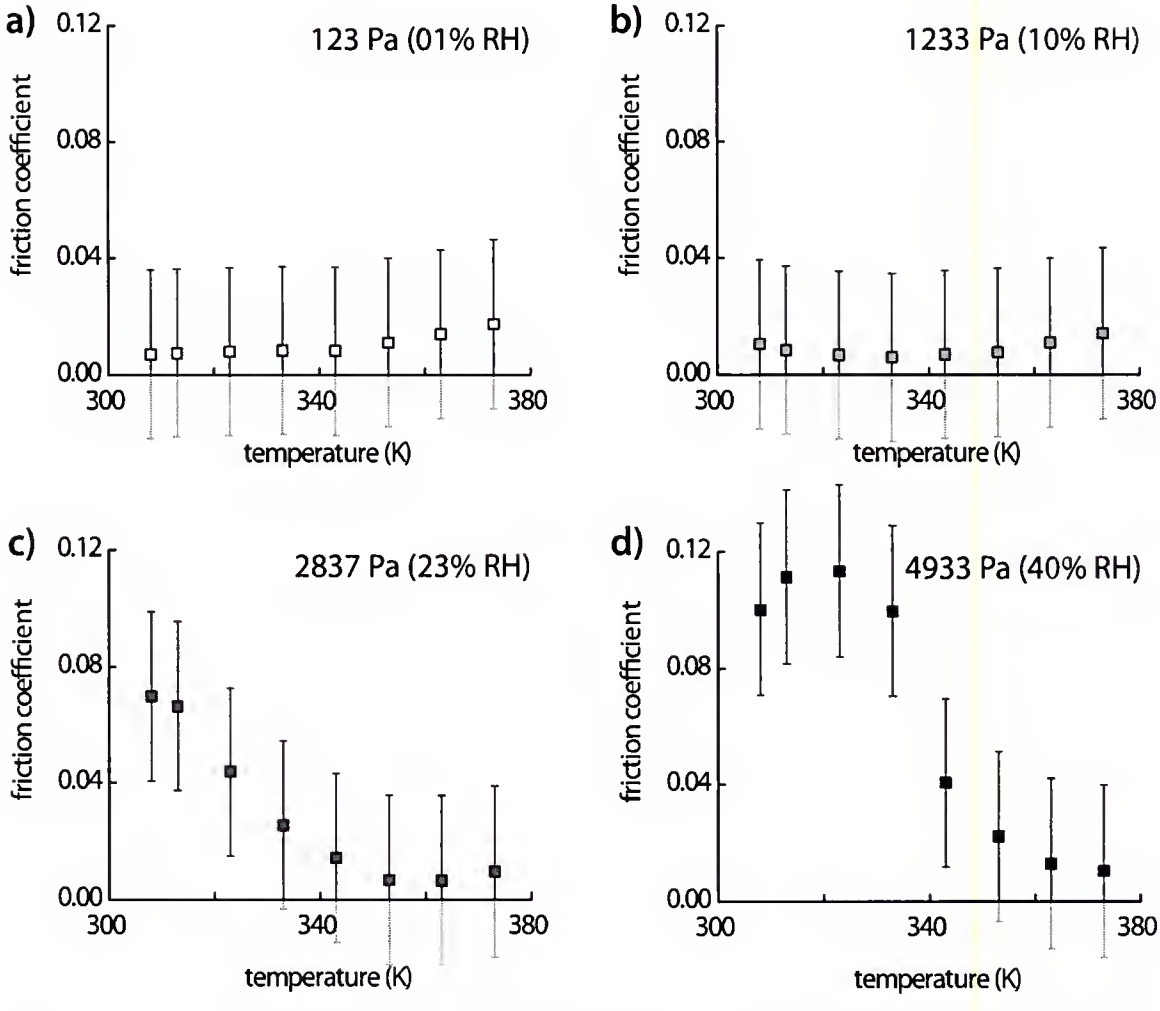

Figure 6-2 Steady state friction coefficient values as a function of counterface surface temperature for a) 123 Pa, b) 1233 Pa, c) 2837 Pa and d) 4933 Pa of water vapor pressure.

Using the analysis outlined in Chapter 4, uncertainty intervals representing one standard uncertainty in friction coefficient are included on each data set. One standard uncertainty interval signifies a 68% confidence level that the true value of friction coefficient lays within the interval. As outlined in Chapter 4 and from Figure 6-2 it can be seen that the uncertainty intervals are significant in magnitude in comparison to the

friction coefficient values. For this reason it would be difficult to say much about the absolute values of friction coefficient for each experiment. Instead, general trends in friction coefficient with water vapor pressure and temperature changes will be examined. Additionally, intervals were calculated for temperature variations that signified the standard deviation of the temperature readings during the 500 cycles of steady state sliding for each data point in Figure 6-2. However, the size of these bars was smaller that the graphic used for each data point in the Figure, so they are not included on the plot. The average of the standard deviations in temperature was 0.29 K with a maximum standard deviation of 0.76 K.

In the experiment with the lowest water vapor pressure, 123 Pa (Figure 6-2a), a low steady state friction coefficient was maintained between the NFC pair over the entire range of surface temperatures. When the water vapor pressure was increased to 1233 Pa (Figure 6-2b) the same low steady state friction coefficient was maintained over the entire range of counterface surface temperatures. When the water vapor pressure in the chamber was increased further to 2837 Pa (Figure 6-2c), a change in friction coefficient was realized. At 308 K and 2837 Pa the friction coefficient of the self mated pair started at μ=0.07. As the substrate temperature was increased there was a monotonic drop in friction coefficient down to the same low friction value as the 123 Pa and 1233 Pa tests (μ~0.009). For the highest water vapor pressure test at 4933 Pa (Figure 6-2d), the friction coefficient at 308 K started at μ~0.1, a higher value than all the previous lower humidity level tests. When the counterface surface temperature was increased the friction coefficient stayed at approximately the same higher value until it reached 333 K. Then the friction coefficient monotonically decreased with increasing substrate temperature

down to the same low friction coefficient value of μ~0.009. The general trends seen in the water vapor pressure and substrate temperature data make sense for the hypothesis of surface adsorption of water on the NFC films interrupting the low friction sliding of the pairs. As the amount of water vapor in the chamber was increased the initial (lowest temperature) steady state friction coefficient increased, which may correlate to more coverage by water vapor leading to a higher friction coefficient. Additionally, if at the lowest temperature state, there was water on the surface (increased μ at T = 308 K), there was a drop in friction coefficient as the counterface temperature was increased, which may correlate to more water desorption from the surface as the counterface temperature is raised.

In addition to putting uncertainty intervals on the data, another useful outcome of the uncertainty analysis from Chapter 4 is the ability to solve and correct for the counterface roll angle, β, for any reciprocating test. It was expected once a counterface sample and stub was secured into the reciprocating stage the roll angle would not be zero, but would remain relatively constant during a single experiment. Analyzing the data from the experiments in Figure 6-2 returned an interesting trend in the roll angle β. Figure 6-3 examines the counterface roll angle as a function of surface temperature for all four water vapor pressure experiments.

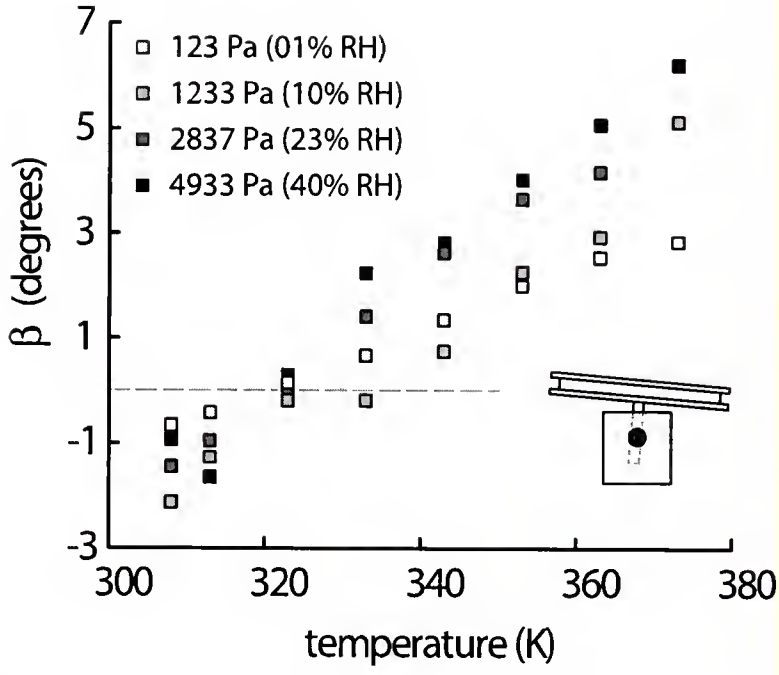

Figure 6-3 Counterface roll angle β as a function of surface temperature for the experiments from Figure 6-2.

In examining the relative positioning of the pin and counterface sample in Figure 4-3, the temperature effect on the roll angle β is not surprising. The counterface stub is held in place with a single set screw and in the loop from the counterface surface to the pin surface there are multiple components made of different materials. Thermal expansions over the range of temperature tested in these experiments could easily cause the monotonic change in roll angle seen in Figure 6-3. Using the uncertainty analysis allowed the temperature dependence of β to been seen and for the bias caused by the misalignment angle to be accounted for in the data.

Frictional trends in the self mated NFC pairs have been established as a function of water vapor pressure and counterface surface temperature (Figure 6-2). Gas-surface modeling for surface coverage will now be used to see if the trends in the friction coefficient correlate to surface adsorption and desorption of water vapor.

6.2 Gas-Surface Modeling: Adsorption and Desorption Rates

The trends in friction coefficient with water vapor pressure and surface temperature have been established experimentally. To compare that data to modeling of surface adsorption and desorption of water vapor, friction coefficient has to be related back to surface coverage. This is done in the same manner as the modeling in Chapter 2, using a linear rule of mixtures. The difference in this chapter the friction coefficient data is transformed into coverage instead transforming the model equations to friction coefficient. This is just a simple rearrangement of eqn 2.22 to the form in eqn 6.1.

$$\theta = \frac{(\mu - \mu_0)}{(\mu_1 - \mu_0)} \qquad \text{eqn 6.1}$$

Using the same values for nascent and fully covered friction coefficient as in previous modeling ($\mu_0 = 0.006$ and $\mu_1 = 0.12$), the friction coefficient data in Figure 6-2 is correlated to fraction surface coverage (θ) in Figure 6-4.

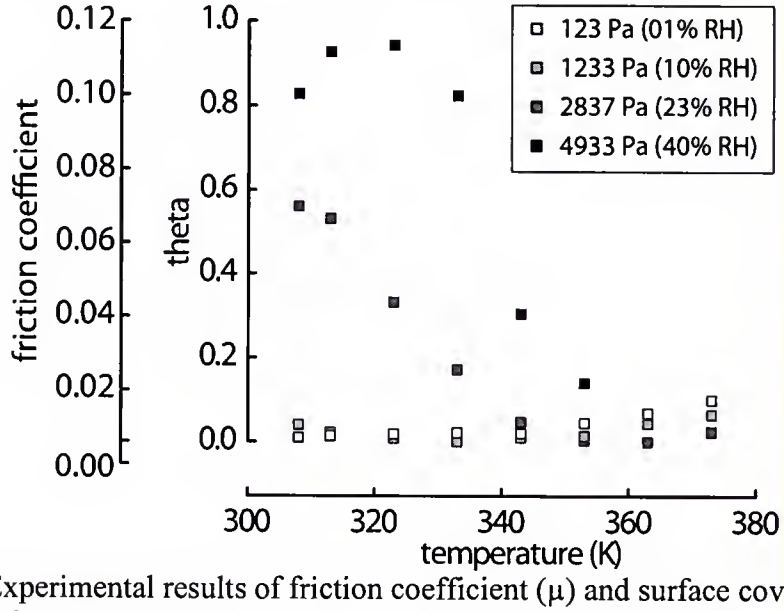

Figure 6-4 Experimental results of friction coefficient (μ) and surface coverage (θ) as a function of counterface surface temperature and water vapor pressure.

Modeling of the trends in surface coverage with changes in water vapor pressure and counterface temperature is going to be performed using the Langmuir model for

relative rates of surface adsorption and desorption [36]. Table 6-1 outlines the modeling parameters that will be used in the derivation.

Table 6-1 Gas-surface modeling nomenclature.

symbol	units	definition
E_a	J/mol	energy to dissociate from surface
I	#/(cm^2-sec)	molecular impingement rate
k	J/K	Boltzmann constant
K_a	1/(Pa-sec)	adsorption rate coefficient
K_d	1/sec	desorption rate
m	kg	molecular mass
n_0	sites/m^2	site density
P	Pa	pressure
subscript ss	n/a	steady state
t	sec	time
T	K	temperature
τ_a	sec	average stay time
τ_0	sec	time between attempts
θ	*	covered fraction
1-θ	*	nascent fraction

The Langmuir model for adsorption and desorption says the change in surface coverage as a function of time is equal to an adsorption rate (K_aP) acting on the nascent portion of the surface (1-θ) minus a desorption rate (K_d) acting on the covered fraction of the surface (θ), as expressed in eqn 6.2.

$$\frac{d\theta}{dt} = K_a P(1-\theta) - K_d\theta \qquad \text{eqn 6.2}$$

This expression can be integrated to solve for the fractional coverage (θ) as a function of the adsorption rate (K_aP), the desorption rate (K_d) the initial coverage (θ_0) and time (t). Details of the integration steps can be found in Appendix K.

$$\theta = \frac{K_a P}{K_a P + K_d} + \left(\theta_0 - \frac{K_a P}{K_a P + K_d}\right) e^{-(K_a P + K_d)t} \qquad \text{eqn 6.3}$$

The data used for model comparison was from cycles 3,500-4,000 of each test and is assumed to be steady state data. The steady state Langmuir model expression for coverage can be found by allowing time to go to infinity in eqn 6.3.

$$\theta_{ss} = \frac{K_a P}{K_a P + K_d} \qquad \text{eqn 6.4}$$

The environmental species added during these experiments was water vapor. To see if the steady state expression in eqn 6.4 compares with the experimental trends seen in varying water vapor pressure and temperature the Langmuir expressions for adsorption rate (K_aP) and desorption rate (K_d) will be examined for water. The Langmuir expression for the adsorption rate coefficient (K_a) is given in eqn 6.5.

$$K_a = \frac{I}{n_0 P} = \frac{1}{n_0 (2\pi m k T)^{\frac{1}{2}}} \qquad \text{eqn 6.5}$$

In this expression, the adsorption rate coefficient is a function of the molecular impingement rate onto the surface (I), the surface site density (n_0), and the pressure (P). The adsorption rate coefficient can also be expressed as a function of the site density (n_0), molecular mass (m), the Boltzmann constant (k), and the temperature driving adsorption (T). For this series of experiments in water vapor, values for all the parameters in the adsorption rate coefficient can be estimated. The site density (n_0) is estimated as 1.26E19 sites/m^2, based on the number of molecules of water per unit area that the surface of the NFC films can accommodate assuming a 2.8 angstrom diameter of a water vapor molecule. The molecular mass of water is taken as 2.99-26 kg. The Boltzmann constant is defined as 1.3807E-23 J/K. Finally, the temperature driving adsorption is going to be assumed to be the surrounding chamber temperature, which was held at 303 K for all of the experiments. Entering these values into eqn 6.5 yields $K_a = 2838\ Pa^{-1}sec^{-1}$. The value

for each of the four water vapor pressures (P) is entered into eqn 6.4 to achieve a value for the adsorption rate (K_aP) and to solve for model fractional coverage (θ).

The Langmuir expression for desorption rate is given in eqn 6.6.

$$K_d = \frac{1}{\tau_a} = \frac{1}{\tau_0} e^{\left(\frac{E_a}{kT}\right)} \qquad \text{eqn 6.6}$$

The Langmuir desorption rate is defined as the inverse of the average stay time (τ_a) of a molecule on the surface. The average stay time of a molecule on the surface is defined as a function of the time between molecular escape attempts off of the surface (τ_0), the activation energy to remove a molecule from the surface (E_a), the Boltzmann constant (k), and the temperature driving the desorption process (T). For the series of experiments executed two of the four parameters in eqn 6.6 are known values. The Boltzmann constant is defined as 1.3807E-23 J/K. The controlled counterface surface temperature of each individual test is taken as the temperature driving the desorption process. The two values in eqn 6.6 that are going to be fit to the experimental data are the time between molecular escape attempts from the surface of the NFC film (τ_0) and the activation energy to remove the molecule from the surface (E_a). The expression for desorption rate is entered into eqn 6.4, to solve for an expression for fractional surface coverage (θ).

Model fits can now be performed between the steady state Langmuir expression for fractional surface coverage in eqn 6.4 and the temperature and water vapor pressure data in Figure 6-4. The two unknown parameters that will be examined in the model fit are the time between molecular escape attempts from the surface of the NFC film (τ_0) and the activation energy to remove the molecule from the surface (E_a). The model fits to these two parameters will be examined to see if gas-surface adsorption and desorption can

explain the experimental trends in friction coefficient with water vapor pressure and counterface surface temperature. The first model fit to the data is examined in Figure 6-5.

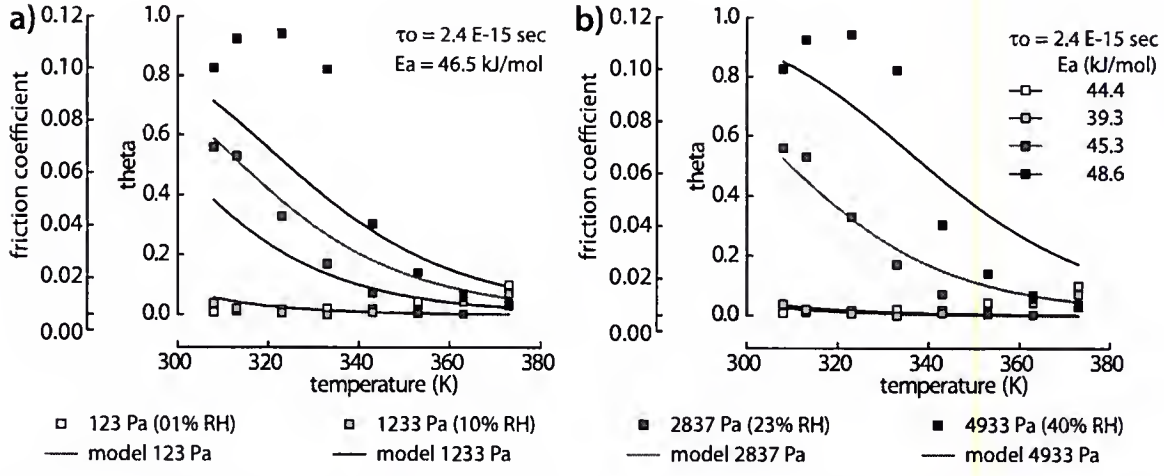

Figure 6-5 Model fit of eqn 6.4 to experimental data with a) a universally fit value for τ_0 and E_a, and b) a universally fit value of τ_0 and a variable fit of E_a.

In Figure 6-5a universal values were fit to all the data points for both the attempt time and the activation energy. This returned a time between escape attempts of τ_0 = 2.5E-15 sec and an activation energy of E_a = 46.5 kJ/mol. Figure 6-5b shows the comparison between eqn 6.4 and the data for a universal value of attempt time and variable fit values for activation energy for each water vapor pressure. These fits returned a time between escape attempts of τ_0 = 2.5E-15 sec and an activation energy ranging from E_a = 39.3 to 48.6 kJ/mol.

The model curve lines in Figure 6-5a do not fit the data extremely well. However, the same general trend is seen in the data and model curves. Allowing the activation energy to vary for each vapor pressure (Figure 6-5b) did return a closer model line and data fit. The average value of these four fits was 44.4 kJ/mol, which compares fairly well

to other investigators experimental results of a 40 kJ/mol activation energy of water off of a Pt(111) surface [37]. Both fits returned value for average stay time of a water molecule on the surface of τ_0 = 2.5E-15 sec, lies within the range of experimentally calculated values [36], but is a little shorter than expected for time between molecular escape attempts off of a surface.

Some researches consider the inverse of the crystal lattice vibrational frequency as a reasonable estimate of the time between molecular surface escape attempts. Using this assumption would result in a value of τ_0 = 1.0E-13 sec. Using this set value for attempt time results in the model fits in Figure 6-6.

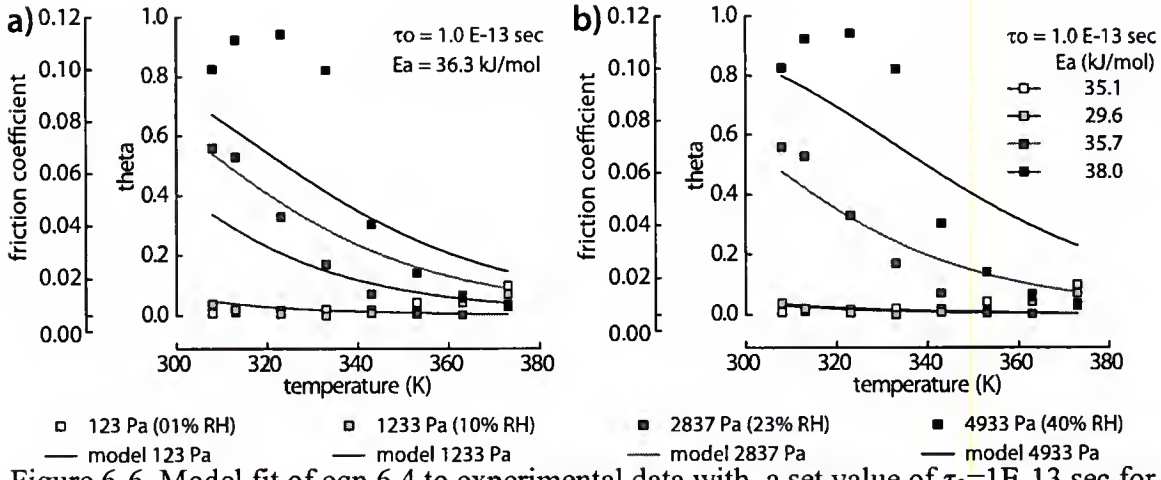

Figure 6-6 Model fit of eqn 6.4 to experimental data with a set value of τ_0=1E-13 sec for a) a universally fit value of E_a, and b) a variable fit of E_a.

In Figure 6-6a a universal value was fit for the activation energy. This returned an activation energy of E_a = 36.3 kJ/mol. Figure 6-6b shows the comparison between eqn 6.4 and the data for variable fit values for activation energy for each water vapor pressure. Allowing the activation energy to vary for each vapor pressure (Figure 6-6b) did return a closer model line and data fit. The average value of these four fits was 34.6

kJ/mol, which also compares fairly well to other investigators experimental results of a 40 kJ/mol activation energy of water off of a Pt(111) surface [37].

While the model line fits and data trends in Figures 6-5 and 6-6 are not perfect, they do compare fairly well for using frictional data from a tribometer as an indication of surface science phenomena. The values fit for an activation energy and average stay time of a molecule on the surface support the idea that a gas-surface adsorption and desorption of water vapor is a contributing factor to the tribological performance of these self mated highly-hydrogenated diamond like carbon films.

CHAPTER 7
CONLCUDING REMARKS

This study on the frictional properties of this highly hydrogenated diamond-like carbon film has established through both modeling and experimental tribometry that surface adsorption and desorption of water vapor in the surrounding environment is a mechanism in the frictional performance of NFC films. The scope of this work can be summarized by each chapter's contributions.

1) This study developed closed form models by balancing competitive rates of adsorption and mechanical removal in a tribological contact. This closed form modeling can be used for coverage prediction by gas-surface interactions of any materials in a tribological contact that experience surface adsorption. (Chapter 2)

2) The derived models were used for comparison to other investigators experimental data of self-mated highly hydrogenated diamond-like carbon films in a self mated contact. This model fitting showed at low friction values the self-mated films behaved in accordance with the derived models. However, at higher friction values the modeling did not predict the positional friction behavior. (Chapter 3)

3) An uncertainty analysis was performed on a low contact pressure tribometer to quantify experimental uncertainty in friction coefficient due to machine measurement design. (Chapter 4)

4) Tribological experiments with self mated NFC films established the as-deposited films have an initial higher friction layer that must be run-in to realize the low friction sliding. A direct and recoverable relationship was established between the amount of water vapor in the experimental chamber and the friction coefficient of self mated NFC films. (Chapter 5)

5) Temperature and water vapor experiments combined with gas-surface modeling verified that surface adsorption and desorption of water vapor is a mechanism that plays a role in the frictional behavior of NFC films. (Chapter 6)

Overall this work has contributed to establish possible useful regimes for near frictionless carbon films. Any practical sliding application of these coatings has to begin with the as-deposited NFC films in a self mated contact being run-in in an inert environment to remove their initial higher friction layer and establish a low-friction regime of sliding. Additionally, the functional application of these coatings is in an inert environment. In practice, this would mean a sealed inert liquid or gas environment, or possibly a space application, where no environmental species would interrupt the low friction sliding. With sustainable friction coefficient values of $\mu = 0.006$ in the proper environment, near frictionless carbon has the potential to serve as a super low friction, low wear coating for tribological contact applications.

APPENDIX A
LANGMUIR MODEL DERIVATION

The approach used to develop a closed-form analytical solution for the fractional coverage of an adsorbed surface film in tribological contact uses a Langmuir adsorption model. The model development offered here is minimally described and written as compactly as possible.

$$\frac{d\theta}{dt} = \nu'(1-\theta)$$

$$\int \frac{d\theta}{(1-\theta)} = \int \nu' dt$$

$$-\ln(1-\theta) = \nu' t + c$$

$$\ln(1-\theta) = -\nu' t + c$$

Boundary Conditions:
at $t = 0$

$$\theta = \theta_{out}$$

$$\ln(1-\theta_{out}) = -\nu'(0) + c$$

$$c = \ln(1-\theta_{out})$$

$$\ln(1-\theta) = -\nu' t + \ln(1-\theta_{out})$$

$$(1-\theta) = \exp[-\nu' t + \ln(1-\theta_{out})]$$

$$(1-\theta) = \exp(-\nu' t)\exp[\ln(1-\theta_{out})]$$

$$(1-\theta) = (1-\theta_{out})\exp(-\nu' t)$$

$$\theta_{in} = 1-(1-\theta_{out})\exp(-\nu' t)$$

$$\theta_{out} = \lambda\theta_{in}$$

$$\theta_{in} = 1-(1-\lambda\theta_{in})\exp(-\nu' t)$$

$$\theta_{in} - \lambda\theta_{in}\exp(-\nu' t) = 1-\exp(-\nu' t)$$

$$\theta_{in} = \frac{1-\exp(-\nu' t)}{1-\lambda\exp(-\nu' t)}$$

The Langmuir model says the surface consists of a number of adsorption sites. All adsorbed species interact only with a site and not with each other. The adsorption is limited to a monolayer.

APPENDIX B
HENRY'S LAW

Henry's law says that the time change of fractional coverage is equal to an adsorption rate v, and is not dependent on the fractional coverage on the surface and has no saturation point:

$$\frac{d\theta}{dt} = \nu$$

The first few terms for the fractional coverage are:

$$\theta_{0in} = \theta_0$$
$$\theta_{0out} = \lambda\theta_0$$
$$\theta_{1in} = \nu t_c + \lambda\theta_0$$
$$\theta_{1out} = \lambda\left(\nu t_c + \lambda\theta_0\right)$$
$$\theta_{2in} = \nu t_c + \theta_{1out}$$
$$\theta_{2out} = \lambda\theta_{2in}$$

This results in a difference pattern of:

$$\Delta\theta_N = \lambda^{(N-1)}(\nu t_c + \lambda\theta_0 - \theta_0)$$

The resulting series expression is:

$$\theta_n = \theta_0 + \sum_{N=1}^{n} \lambda^{(N-1)}(\nu t + \lambda\theta_0 - \theta_0)$$

The closed-form solution for coverage based on cycle number then becomes:

$$\theta_n = \theta_0 + \left[\frac{1-\lambda^n}{1-\lambda}\right]\left(\nu t_c + \lambda\theta_0 - \theta_0\right)$$

Taking the number of cycles to infinity gives a steady-state solution:

$$\theta_{SS} = \frac{\nu t_c}{1-\lambda}$$

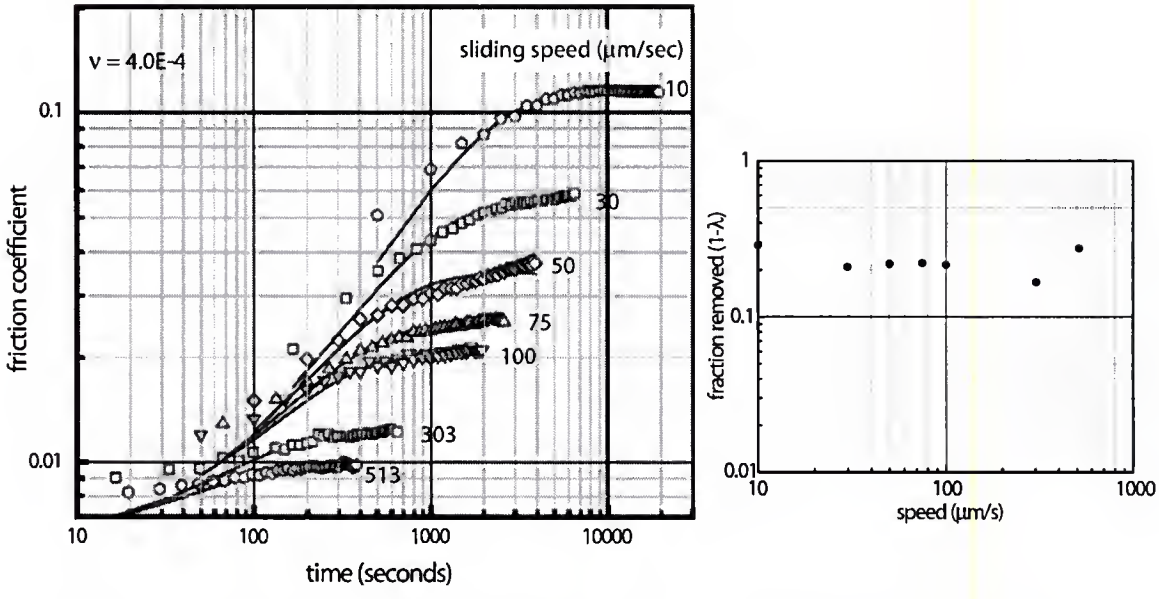

Figure AB-1 Henry's Law model fit to Heimberg et al. data from Figure 3-2.

Model fits of the Henry model expression match the data in Figure AB-1 about as well as the Langmuir derived closed-form model fit in Figure 3-2. One item of note in the Henry derived model the values of the fractions removed, 1-λ, are approximately the same values as for the Langmuir model. The scope of this work is not discuss merits or the validity one gas-surface model over another, but rather to see if trends in the frictional data can be correlated to surface phenomena. The close model fit of the Henry equation supports the argument of gas-surface adsorption playing a role in the tribological performance of NFC films.

APPENDIX C
ELOVICH EQUATION

The Elovich equation is an empirical model for adsorption rate that has a unique dependence on the surface fractional coverage:

$$\frac{d\theta}{dt} = \nu \exp(-\alpha\theta)$$

The same recursive modeling derivation as used in Chapter 2 can be applied using the Elovich equation.

$$\frac{1}{\alpha}\exp(\alpha\theta) = \nu t + c$$
$$\exp(\alpha\theta) = \alpha\nu t + \alpha c$$
$$\alpha\theta = \ln(\alpha\nu t + \alpha c)$$
$$\theta = \frac{1}{\alpha}\ln(\alpha\nu t + \alpha c)$$

Boundary Conditions:
at t=0

$$\theta = \theta_{out}$$

$$c = \frac{\exp(\alpha\theta_{out})}{\alpha}$$

$$\theta_{in} = \frac{1}{\alpha}\ln[\alpha\nu t + \exp(\alpha\theta_{out})]$$

$$\theta_{out} = \lambda\theta_{in}$$

For cycle zero:

$\theta_{in} = 0$

$\theta_{out} = 0$

For each cycle:

θ_{in} uses the θ_{out} from the previous cycle

$$\theta_{ss} = \frac{\ln(-\alpha t v + 1)}{\alpha\lambda}$$

This model has no saturation point, and fractional coverage is allowed to proceed past unity. The first few terms of the inlet fractional coverage (θ_{in} values), letting $\beta = \alpha v t$ and $\gamma = \exp(\alpha\lambda\theta_0)$, are:

$$\theta_1 = \left(\frac{1}{\alpha}\right)\ln(\beta + \gamma)$$

$$\theta_2 = \left(\frac{1}{\alpha}\right)\ln\left(\beta + (\beta + \gamma)^{\lambda}\right)$$

$$\theta_3 = \left(\frac{1}{\alpha}\right)\ln\left(\beta + \left(\beta + (\beta + \gamma)^{\lambda}\right)^{\lambda}\right)$$

This repetition inside the natural log term can be compactly described as:

$$U_n = \beta + (U_{n-1})^{\lambda}$$

$$U_{n+1} = \beta + (U_n)^{\lambda}$$

Unfortunately, there is no closed-form solution for this recursive relationship; however, the equation can be easily used computationally. Figure AC-1 is the Elovich numerical model solution fit to the data from Figure 3-2.

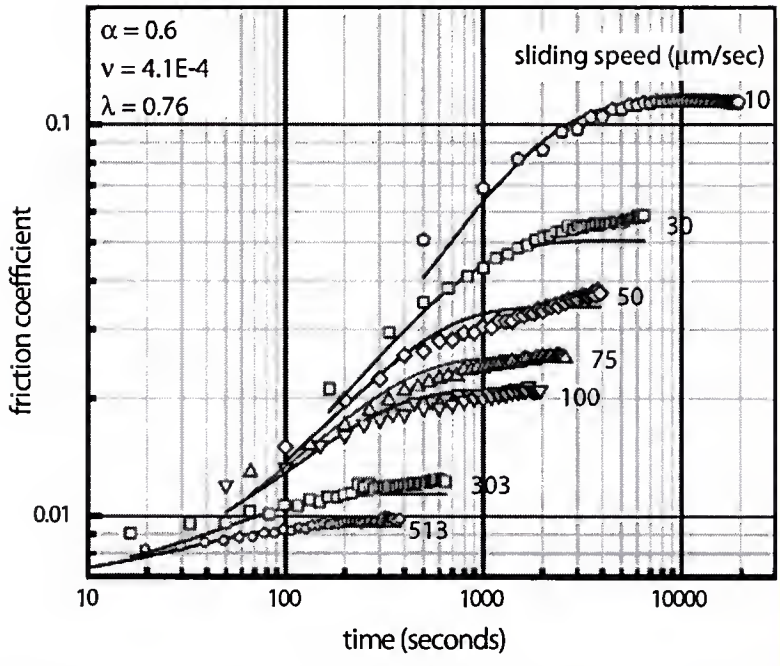

Figure AC-1 Elovich numerical model fit to Heimberg et al. data from Figure 3-2.

Numerical fits of the Elovich model expression match the data in Figure AC-1 about as well as the Langmuir derived closed-form model fit in Figure 3-2. One item of note in the Elovich derived model is a single value of the removal ratio, λ, is used for all of the sliding speed data. The scope of this work is not discuss merits or the validity one gas-surface model over another, but rather to see if trends in the frictional data can be correlated to surface phenomena. The close numerical model fit of the Elovich equation supports the argument of gas-surface adsorption playing a role in the tribological performance of NFC films.

APPENDIX D
LINEAR APPERANCE OF CURVES

The forward-direction-entering fractional coverage expression given in eqn 2.16 is examined to illustrate why the model curves appear linear. Cycle dependence enters through the g^{n-1} term in eqn 2.16. Position dependence occurs in the c term of the expression. From Table 2-6, $c = \lambda\left(1-e^{-\nu P t_r}\right)e^{-\nu P t_f} + \left(1-e^{-\nu P t_f}\right)$, which can also be written as $c = 1-\left(1-\lambda\right)e^{-\nu P t_f} - \lambda e^{-\nu P T}$. The only term that is track position (a, following the nomenclature in Figure 2-3) dependent in the expression is t_f, which can be expressed as $t_f = \frac{2a}{V}$ for a constant speed V. Note that for the experimental conditions evaluated here, the expressions $\nu P t_f$ and λ are always between 0 and 1. The first few terms of the series expansion of an exponential is given in eqn. AD.1.

$$e^{-s} = 1 - s + \frac{s^2}{2!} - \frac{s^3}{3!} + \ldots \qquad \text{AD.1}$$

For the case of a fractional value of s the higher order terms of the expression are alternating in sign and small in comparison to the first-order terms. Substituting the first-order terms from the exponential into the expression for c and simplifying yields,

$$c = \left[\lambda\left(1-e^{-\nu P T}\right)\right] + \left[\left(1-\lambda\right)\frac{2\nu P}{V}\right]a \qquad \text{AD.2}$$

The terms in the square brackets of eqn AD.2 are constants for any given test. While the analytical expressions were used in the model fittings, the above order-of-magnitude analysis describes the linear appearance of the model curves.

APPENDIX E
INFLUENCE OF PICH ANGLE ON UNCERTAINTY

The influence of varying the value of the pitch angle, ϕ on the value of the uncertainty in the friction coefficient is addressed in this appendix, for the body of the work both the pitch angle and the uncertainty in the pitch angle were set to a value of 0.035 radians for all calculations. In this evaluation, regardless of value, the pitch angle and the uncertainty in the pitch angle are always set to be equal. The uncertainty in the coefficient of friction (eqns 4.34-4.37) can be evaluated over a range of values for the pitch angle, ϕ and uncertainty in the pitch angle. From these equations it can be shown the uncertainty in the friction coefficient, $u(\mu)$, is a function of the roll angle, β, and uncertainty in the roll angle $u(\beta)$, as well as the tribometer read friction coefficient, μ_f', and the uncertainty in the tribometer read friction, $u(\mu_f')$. Entering values of $\beta = -0.025$ rad, $u(\beta) = 0.017$ rad, $\mu_f' = 0.095$ and $u(\mu_f') = 0.025$, conditions from one of the experiments in Chapter 6 (2837 Pa water pressure and 308 K counterface temperature), yields the expression in eqn AE.1 for the square of the uncertainty in friction coefficient.

$$u^2(\mu) = 0.005u^2(\phi)\sin\left(u^2(\phi)\right) + 0.0009\cos\left(u^2(\phi)\right) \qquad \text{eqn AE.1}$$

Figure AE-1 examines the effect on the uncertainty in friction coefficient by varying the value of the pitch angle in eqn AE.1.

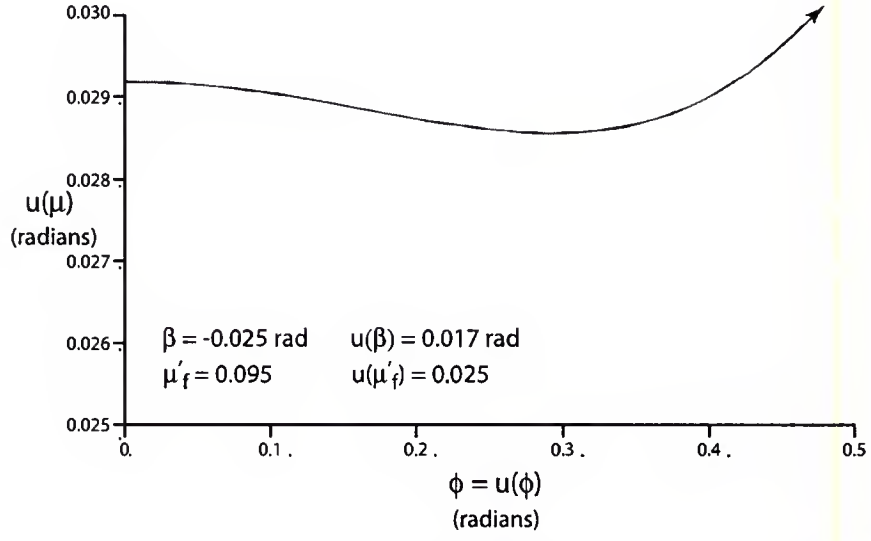

Figure AE-1 Effect of the pitch angle on the uncertainty in friction coefficient for the 2837 Pa water pressure and 308 K counterface temperature experiment

Figure AE-1 shows that as the pitch angle is increased there is an initial drop in the uncertainty in friction coefficient, a minimum value is reached around $\phi = 0.32$ rad, and then with increasing ϕ there is a monotonic increase in the uncertainty in friction coefficient. This initial decrease in the uncertainty in friction coefficient was not intuitive. It was thought as the pitch misalignment angle increased it would naturally cause an increase in the value of the uncertainty of the friction coefficient.

APPENDIX F
RUN-IN BOND ENERGY

The energy dissipated during the approximately 1500 cycles of higher friction run-in sliding in Figure 5-2 can be estimated by equation AF.1.

$$E = (\mu)(Fn)(2length)(\#cycles) \qquad \text{AF.1}$$

Where the energy, E, is a function of the friction coefficient, μ, the normal load, Fn, the track length and the number of cycles. The values for experimental parameters are entered in, (eqn AF.2) resulting in approximately 0.09 J of energy.

$$E = (0.5)(0.1N)(0.0012m)(1500) = 0.09J \qquad \text{AF.2}$$

From neutron reflectivity [35] initial surface layer is thought to be 30 Å thick. Under the 100 mN load, the Hertzian track width was approximately 0.05mm, and the reciprocating track length was 0.6mm during the run-in experiment. This results in a higher density layer volume of approximately 90 μm^3 that needs to be run through to reach the lower friction sliding. Based on a 1.5Å C-C bond length, there are 1.3E13 bonds that would need to be broken during the run-in sliding. Using a 350 kJ/mol bond energy, the energy needed to break that number of bonds is approximately 8μJ. The frictional energy

dissipated during sliding (eqn AF.2) was 90mJ, so there was more than enough energy put into the contact from sliding to break the bonds associated with the higher density layer on the as-deposited NFC films.

APPENDIX G
PRELIMINARY LOW CONTACT PRESSURE EXPERIMENTS

A preliminary series of experiments consisted of varying the normal load, sliding speed and reciprocating track length to try to find the range of test conditions under which a self mated NFC pair would realize both low friction values and free sliding between the pin and flat samples. In the modeling derived in Chapter 2 the predicted friction coefficient of self-mated NFC tribological pairs was a function of competitive rates of surface exposure time (gaseous species adsorption) and adsorbate removal. If surface species adsorption is a function of exposure time, variations in sliding speed and track length can be implemented to experimentally vary exposure time. Additionally, normal load variations can be implemented to see if contact pressure contributes to adsorbate removal. Each of these tests was run in a dry argon environment for 300 cycles of reciprocation. Sliding speed was varied from 0.05 to 5 mm/s, normal load from 3 to 300 mN and reciprocating track length from 0.06 to 0.6mm.

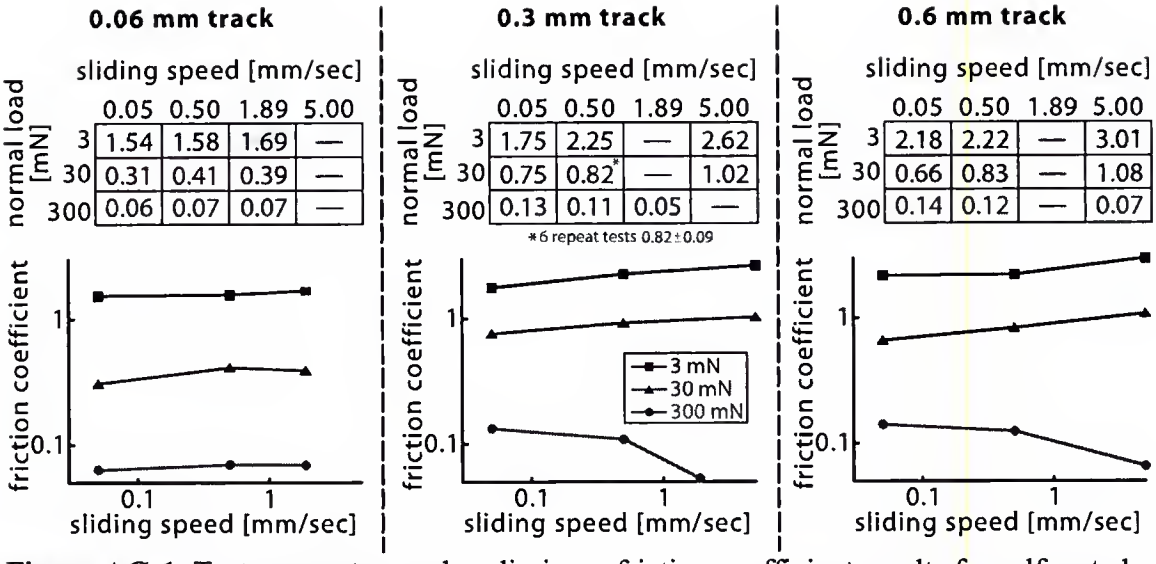

Figure AG-1 Test parameters and preliminary friction coefficient results for self mated NFC films in a dry argon environment over a range of sliding speeds, reciprocating track lengths, and normal loads.

Figure AG-1 shows the friction coefficient results from varying sliding speed, track length, and normal load over a broad range to try to find a low friction regime for self mated NFC films in a dry argon environment. These preliminary tests show for self mated NFC samples in dry argon the optimal operating conditions for a combination of low friction coefficient and free sliding of the samples with the low pressure tribometer are at speeds above 1.89 mm/s, reciprocating track lengths above 0.3mm, and loads above 300 mN. Having optimal conditions under a higher load and speed range supports the hypothesis that gas-surface interactions are the cause for variations in friction coefficient. A higher sliding speed reduces the amount of environmental exposure time between pin contacts and a higher load promotes more energy to wiping the surface under the pin contact.

APPENDIX H
NFC-NFC DRY ARGON

The first matrix of tests was a self-mated NFC pair in a dry argon environment. Figure 5-6 shows the parameters varied in the test matrix as well as steady state friction coefficient value for each parameter combination. The steady state friction coefficient was calculated as the average of cycles 375-400 of sliding over the middle third of the reciprocating path length (to remove reversal locations). The order of the tests run was randomized. For the repeat tests the average value for the steady state values along with their standard deviation is reported.

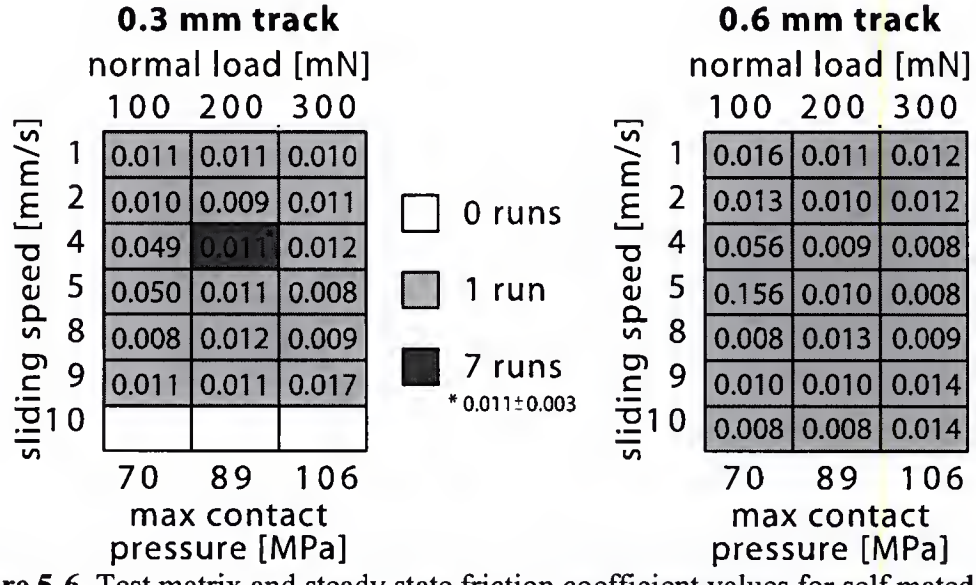

Figure 5-6 Test matrix and steady state friction coefficient values for self mated NFC samples in a dry argon environment.

The variation of the sliding speed, track length, and normal load was used in this matrix to look for the influence of sample exposure time and removal energy in the pin contact.

In examining the steady state friction coefficient data there was no apparent trend in the data with load, speed or length. In most cases the friction coefficient of the self mated pair in dry argon averaged μ=0.01. This value is fairly low and shows under the range of experimental conditions in this matrix low friction was sustained and the NFC pair did not experience any surface adsorption or interaction that interrupted the low friction regime. There was also no trend in the shape of the run-in portion of the friction coefficient plots. Each test was run on a new counterface location and slight variations in the shape of the run-in portion of each curve are attributed to localized variations in the surface composition of the NFC film.

NFC/NFC in dry argon (0.3 mm track length)

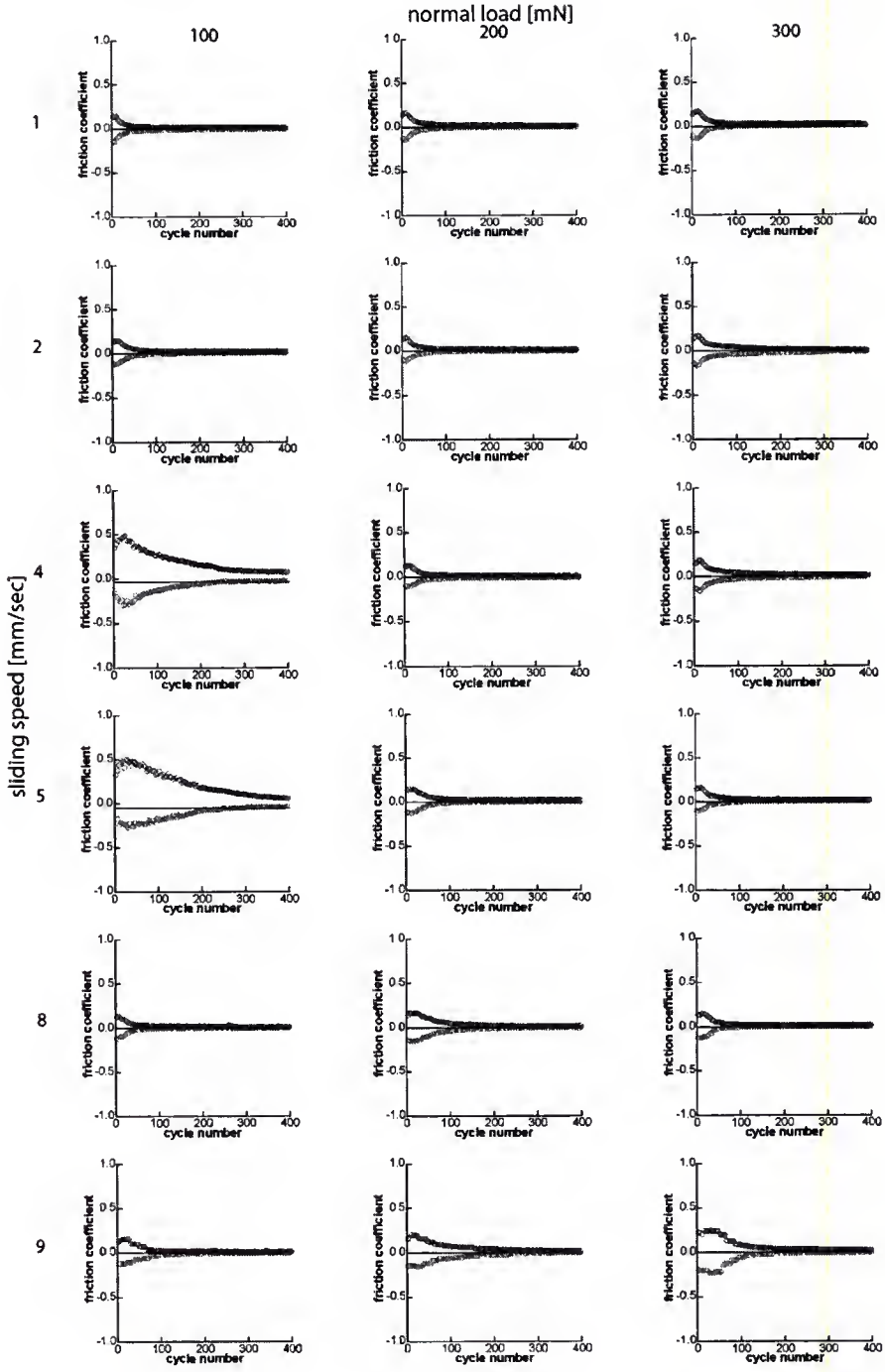

NFC/NFC in dry argon (0.6 mm track length)

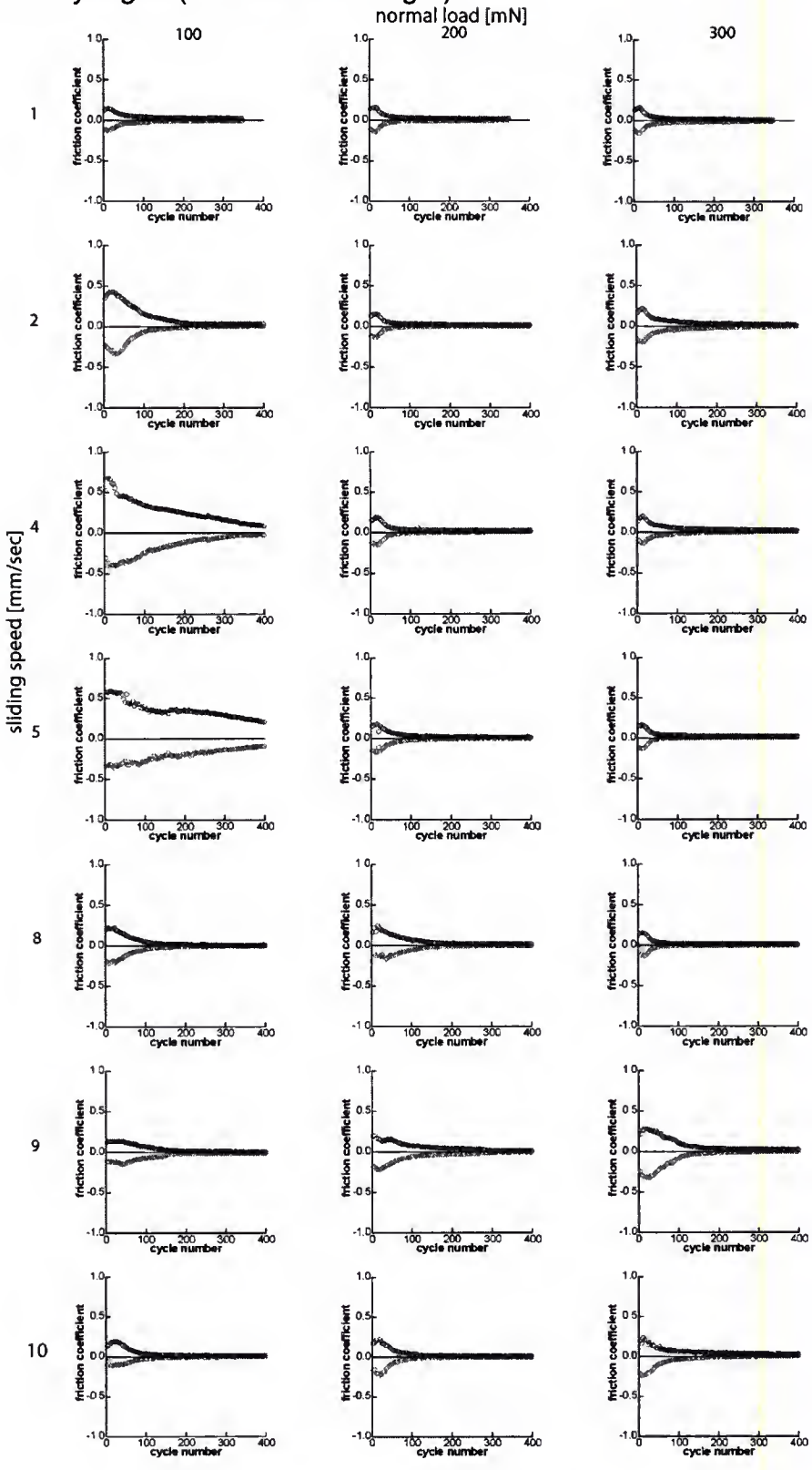

NFC/NFC in dry argon (Repeat Tests - 0.3 mm track length)

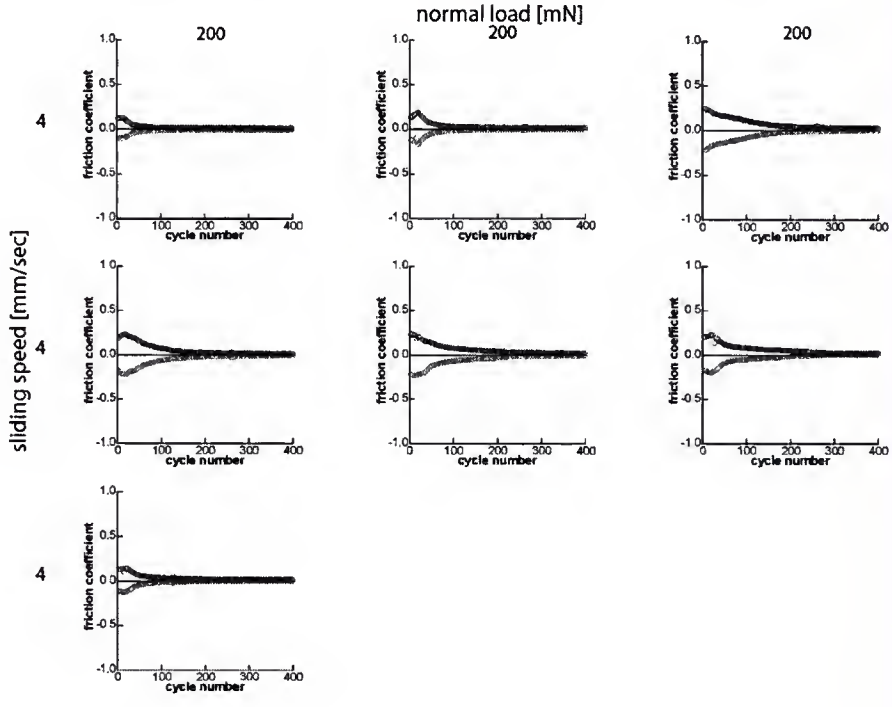

APPENDIX I
GLASS-NFC DRY ARGON

The second test matrix in this series consisted of an uncoated borosilicate glass pin on a NFC coated sample in a dry argon environment. This series served as a comparison matrix to see if under the same set of speed, track length and load conditions a difference in the friction coefficient could be seen between a non-NFC/NFC and a self mated NFC pairing. Again, the order of testing was randomized and the steady state friction coefficient was calculated from the last 25 cycles of sliding. Figure 5-7 shows the parameters varied in this matrix as well as steady state friction coefficient value for each parameter combination.

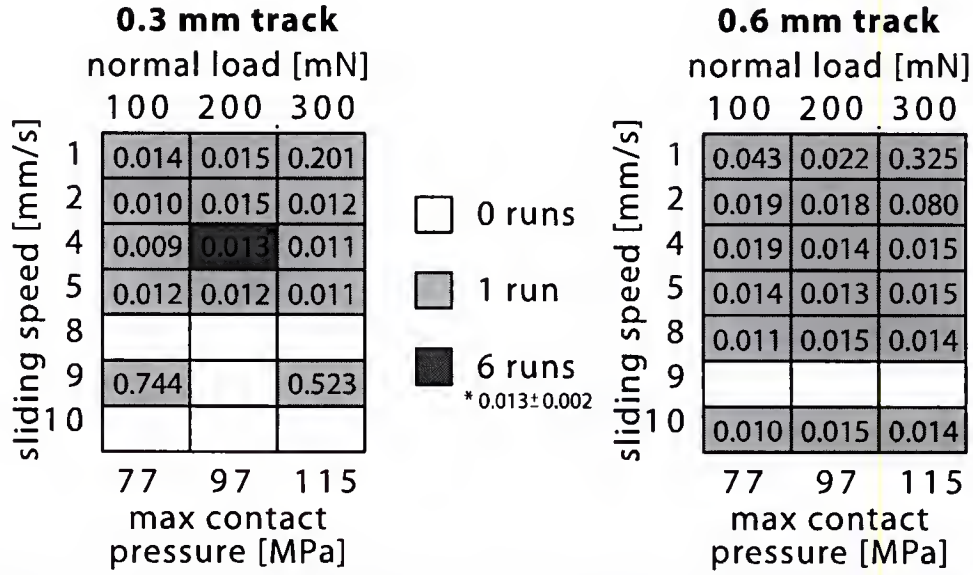

Figure 5-7 Test matrix and steady state friction coefficient values for glass pin against NFC coated counterface in a dry argon environment.

This data also showed no trend for steady state friction coefficient as a function of load, speed or track length. For the majority of the tests the steady state friction was slightly higher (μ=0.015) than in the self mated NFC pair in dry argon. It is surprising that for a glass-NFC pair in dry argon the friction coefficient is similar to the low friction value seen for the NFC-NFC pair in dry argon. If the mechanism for low friction is the uninterrupted sliding of self mated hydrogen terminated carbon surfaces, it would not be expected that the glass-NFC pair would realize such a low friction coefficient. There were a few tests that had noticeably larger steady state friction coefficients than the majority of the matrix. Upon further examination, it was noted that for these higher friction tests the parts per million (ppm) of O_2 in the chamber were slightly higher than the other tests. The reduction in the ppm of O_2 in the chamber is both an indication of the ppm of water vapor in the chamber and the order in which the tests were run, as testing progressed a constant purge or argon gas went through the chamber and the ppm of both O_2 decreased with time. These few tests with a higher friction coefficient could be an indication that as testing progressed a change occurred on the single ball surface used for this entire matrix that allowed the latter tests to see a lower friction coefficient. It could also be an indication that the NFC films are sensitive to relatively low amount of O_2 and/or water vapor, and until the ppm of these environmental species dropped below a certain threshold lower friction coefficient values could not be realized. There was also no trend in the shape of the run-in portion of the friction coefficient plots. Slight variations in the shape of the run-in portion of each curve are attributed to localized variations in the surface composition of the NFC film.

glass/NFC in dry argon (0.3 mm track length)

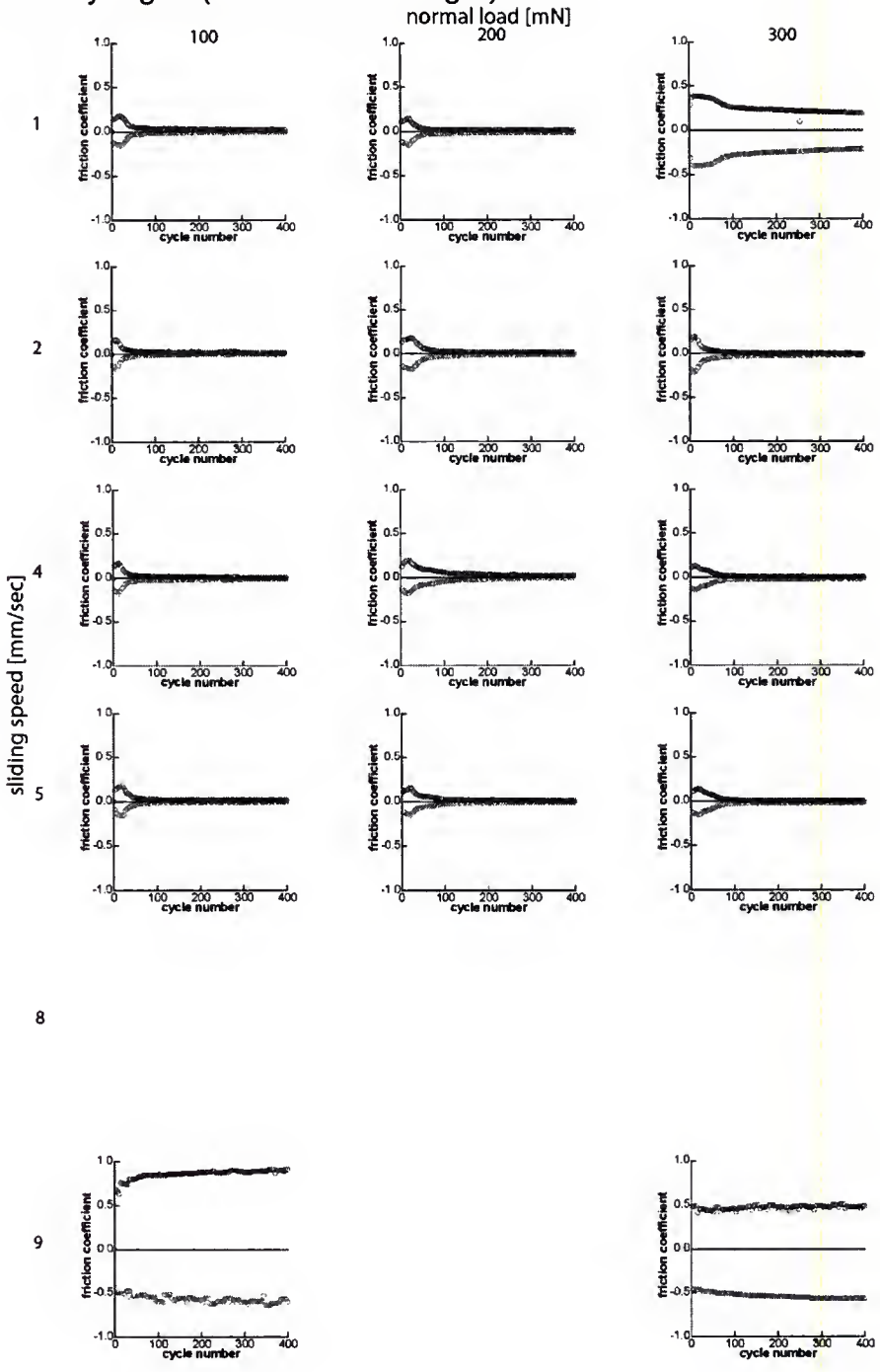

glass/NFC in dry argon (0.6 mm track length)

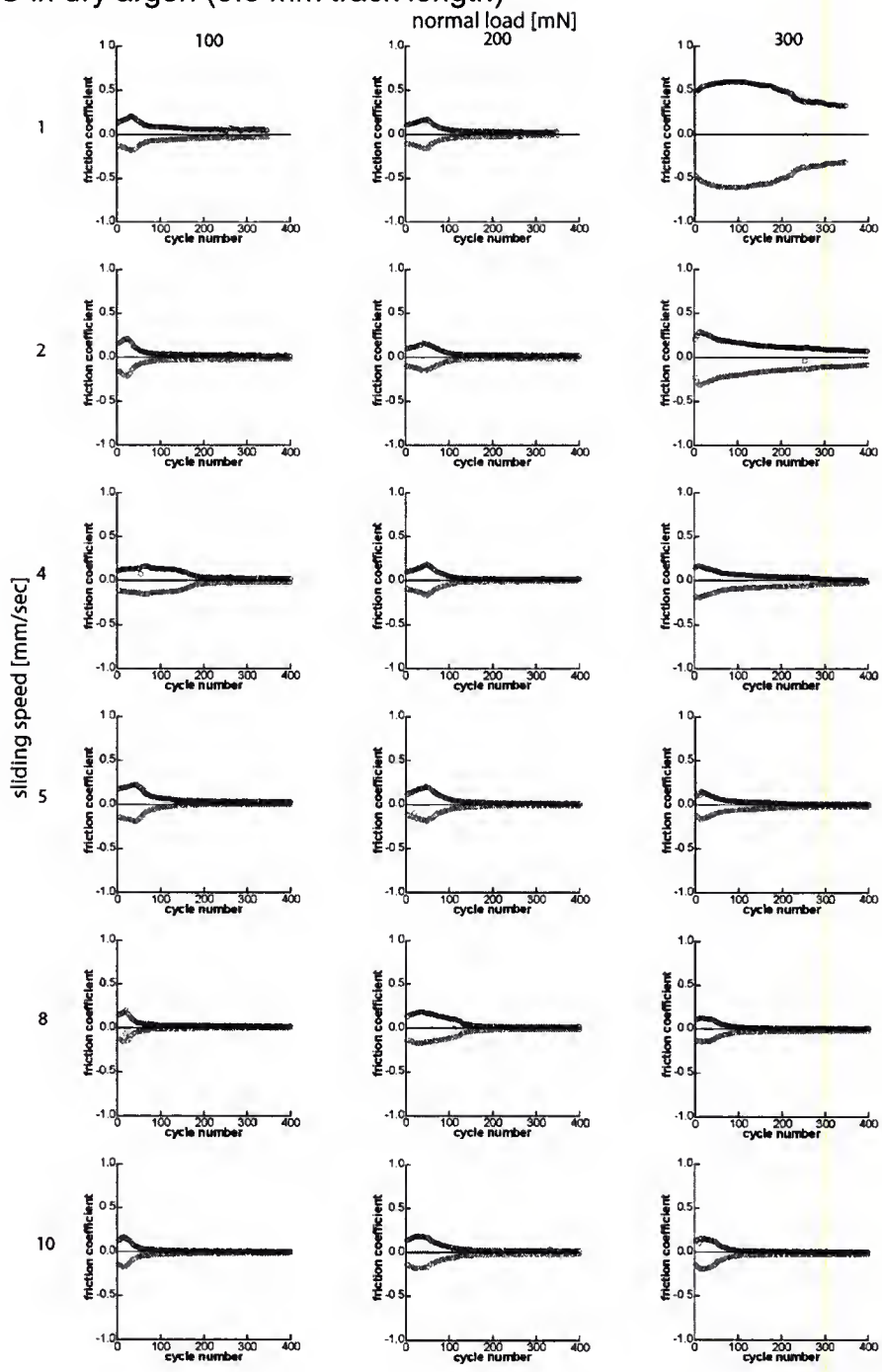

glass/NFC in dry argon (Repeat Tests - 0.3 mm track length)

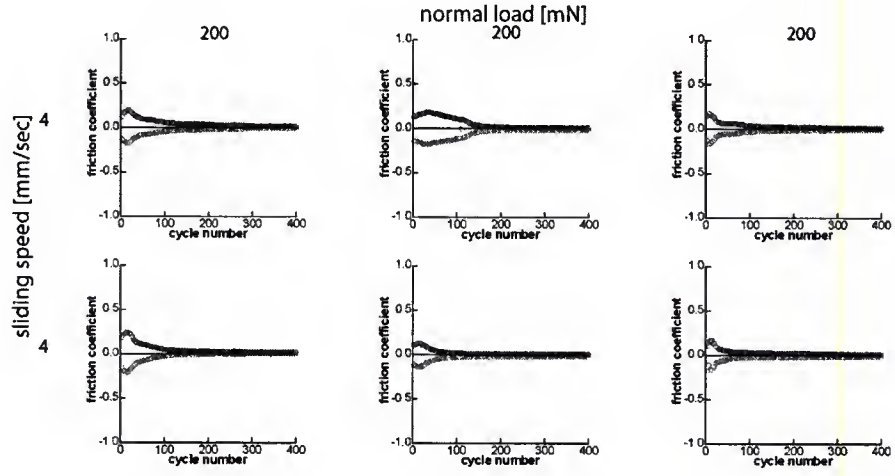

APPENDIX J
NFC-NFC HUMID ARGON

The third matrix of tests in this series consisted of a self-mated pair of NFC films in an argon environment with water vapor added to achieve 10% relative humidity. This series served as a comparison matrix to see if under the same set of load, speed and track length conditions a difference in the friction coefficient could be seen for NFC/NFC pairing between a dry argon and wet argon environment. During this matrix the ppm of O_2 in the environment was kept below the same level (10 ppm O_2) as the dry argon tests via use of the bubbler schematic described in Figure 4-7. Again, the order of testing was randomized and the steady state friction coefficient was calculated from the last 25 cycles of sliding. Figure 5-8 shows the parameters varied in this matrix as well as steady state friction coefficient value for each parameter combination.

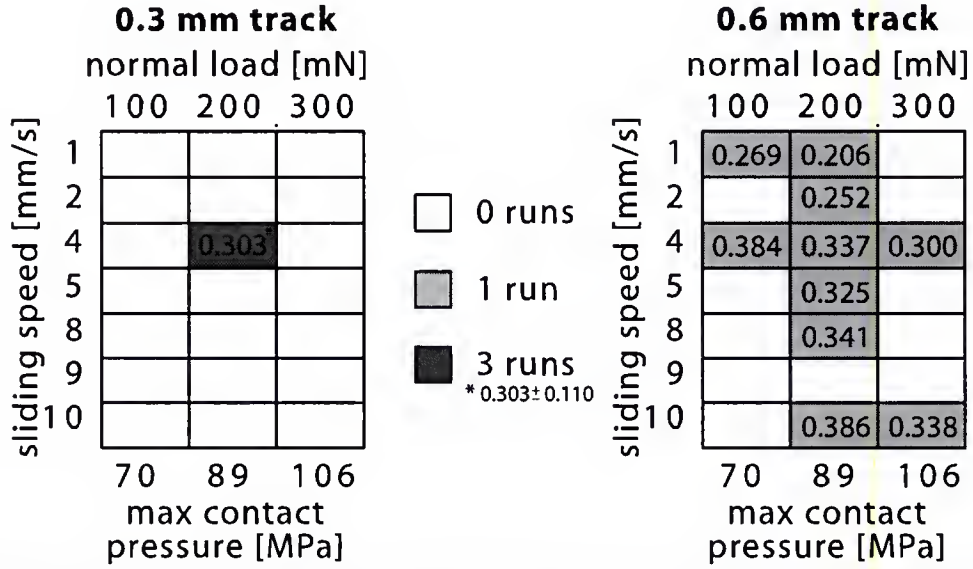

Figure 5-8 Test matrix and steady state friction coefficient values for self mated NFC coated pair in a humid argon environment.

This data also showed no trend for steady state friction coefficient as a function of load, speed or track length. The average steady state friction coefficient (μ=0.35) was higher than both the self mated NFC pair and glass pin with NFC flat pair in dry argon. The lack of trend as a function of load, speed and track length could be due to the fact that at 10% RH the surface of the NFC films becomes completely saturated with water vapor and the combinations of loads, speeds and track lengths prescribed in this matrix is not enough for the removal portion of the pin interaction to overcome the adsorption occurring from the environment on the NFC surface. The fact that the steady state friction coefficient is higher for all teat combinations in the humid argon environment supports the idea that environmental exposure to water vapor causes an increase in friction coefficient of NFC films. There was also no trend in the shape of the run-in portion of the friction coefficient plots. Slight variations in the shape of the run-in portion of each curve are attributed to localized variations in the surface composition of the NFC film.

NFC/NFC in humid argon (0.6 mm track length)

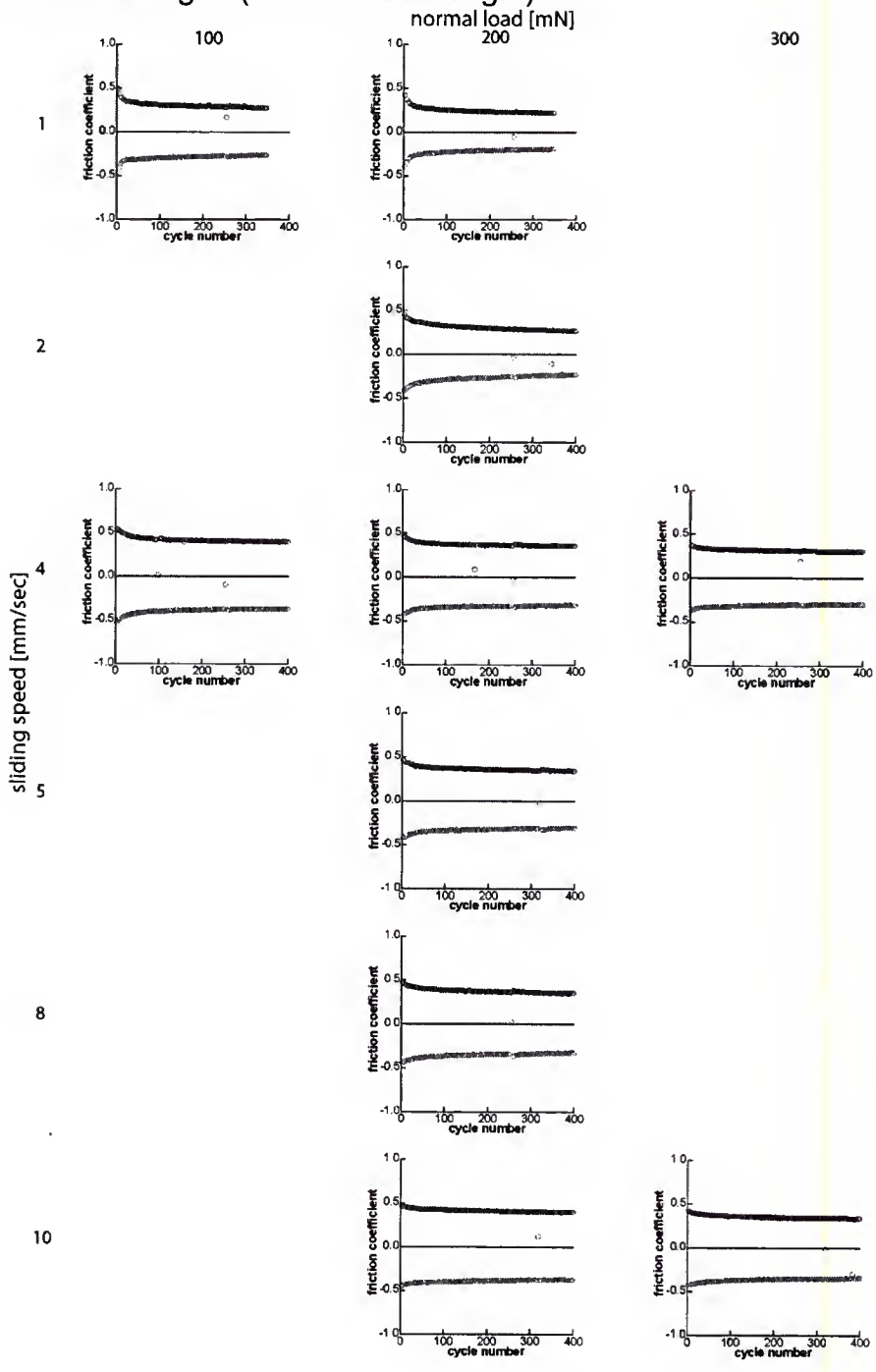

NFC/NFC in humid argon (Repeat Tests - 0.3 mm track length)

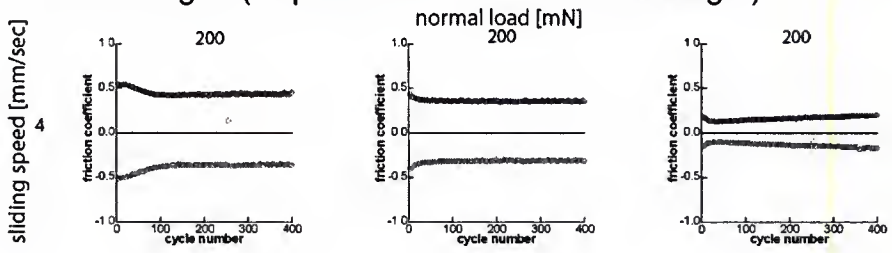

APPENDIX K
LANGMUIR ADSOPTION AND DESORPTION INTEGRATION

The steps for the integration performed for the Langmuir adsorption and desorption modeling of Chapter 6 is expressed as compactly as possible.

$$\frac{d\theta}{dt} = K_a P(1-\theta) - K_d\theta$$

$$\frac{d\theta}{dt} + (K_a P + K_d)\theta = K_a P$$

$$e^{\int (K_a P + K_d)dt}\frac{d\theta}{dt} + e^{\int (K_a P + K_d)dt}(K_a P + K_d)\theta = e^{(K_a P + K_d)dt} K_a P$$

$$\theta(t) e^{\int (K_a P + K_d)dt} = \int\left(K_a P e^{\int (K_a P + K_d)dt}\right)dt + C$$

$$\theta(t) = \frac{1}{e^{(K_a P + K_d)t}}\left[\frac{K_a P}{(K_a P + K_d)} e^{(K_a P + K_d)t} + C\right]$$

$$\theta(0) = \theta_0$$

$$C = \theta_0 - \frac{K_a P}{(K_a P + K_d)}$$

$$\theta = \frac{K_a P}{K_a P + K_d} + \left(\theta_0 - \frac{K_a P}{K_a P + K_d}\right) e^{-(K_a P + K_d)t}$$

$$\theta_{ss} = \frac{K_a P}{K_a P + K_d}$$

LIST OF REFERENCES

[1]Erdemir, A., *Modern tribology handbook*, in *Mechanics and materials science series*, B. Bhushan, Editor. 2001, CRC Press: Boca Raton, FL. p. 787-825.

[2]Grill, A., 1999,"Diamond-like carbon: state of the art," Diamond and Related Materials, **8**, pp. 428-434.

[3]Erdemir, A., Eryilmaz, O.L., Nilufer, I.B., and Fenske, G.R., 2000,"Synthesis of superlow-friction carbon films from highly hydrogenated methane plasmas," Surface & Coatings Technology, **133**, pp. 448-454.

[4] Liu, Y., Erdemir, A., Meletis, E.I., 1996, "A study of the wear mechanism of diamond-like carbon films," Surface &. Coatings Technology, **82**, pp. 48-56.

[5] Lu, L., Jones, M.W., Wu, R.L., 1993, "Diamond-like carbon as biological compatible material for cell culture and medical application," Bio-Medical Materials and Engineering, **3**, pp. 223-228.

[6] Liu, Y., Erdemir, A., Meletis, E.I., 1997, "Influence of environmental parameters on the frictional behavior of DLC coatings," Surface & Coatings Technology, **94-95**, p. 463.

[7]Erdemir, A., Eryilmaz, O.L., Nilufer, I.B., and Fenske, G.R., 2000,"Effect of source gas chemistry on tribological performance of diamond-like carbon films," Diamond and Related Materials, **9**, pp. 632-637.

[8]Erdemir, A., 2001,"The role of hydrogen in tribological properties of diamond-like carbon films," Surface & Coatings Technology, **146**, pp. 292-297.

[9]Heimberg, J.A., Wahl, K.J., Singer, I.L., and Erdemir, A., 2001,"Superlow friction behavior of diamond-like carbon coatings: Time and speed effects," Applied Physics Letters, **78**, pp. 2449-2451.

[10]Andersson, J., Erck, R.A., and Erdemir, A., 2003,"Frictional behavior of diamondlike carbon films in vacuum and under varying water vapor pressure," Surface & Coatings Technology, **163-164**, pp. 535-540.

[11]Rowe, C.N., 1967,"A Relation between adhesive wear and heat of adsorption for vapor lubrication of graphite," ASLE Transactions, **10**, pp. 10.

[12]Langmuir, I., 1916,"The constitution and fundamental properties of solids and liquids," Journal of the American Chemical Society, **38**, pp. 2221-2295.

[13]Bowden, F.P. and Rowe, G.W., 1957,"Lubrication with molybdenum disulphide formed from the gas phase.," Engineer, 667.

[14]Blanchet, T.A., Lauer, J.L., Liew, Y.F., Rhee, S.J., and Sawyer, W.G., 1994,"Solid lubrication by decomposition of carbon-monoxide and other gases," Surface & Coatings Technology, **68**, pp. 446-452.

[15]Zaidi, H., Paulmier, D., and Lepage, J., 1990,"The influence of the environment on the friction and wear of graphitic carbons .2. Gas coverage of wear debris," Applied Surface Science, **44**, pp. 221-233.

[16]Adamson, A.W. and Gast, A.P., 1997, *Physical chemistry of surfaces*, 6th ed. Wiley, New York.

[17]Sawyer, W.G. and Blanchet, T.A., 2001,"Vapor-phase lubrication in combined rolling and sliding contacts: Modeling and experimentation," Journal of Tribology-Transactions of the ASME, **123**, pp. 572-581.

[18]Blanchet, T.A. and Sawyer, W.G., 2001,"Differential application of wear models to fractional thin films," Wear, **251**, pp. 1003-1008.

[19]Dickrell, P.L., Sawyer, W.G., and Erdemir, A., 2004,"Fractional coverage model for the adsorption and removal of gas species and application to superlow friction diamond-like carbon," ASME Journal of Tribology, **126**, pp. 615-619.

[20]Erdemir, A., Fenske, G.R., Terry, J., and Wilbur, P., 1997,"Effect of source gas and deposition method on friction and wear performance of diamondlike carbon films," Surface & Coatings Technology, **94-5**, pp. 525-530.

[21]Casiraghi, C., Piazza, F., Ferrari, A.C., Grambole, D., Robertson, J., 2004, "Bonding in hydrogenated diamond-like carbon by Raman spectroscopy," Diamond and Related Materials, **14**, pp. 1098-1102.

[22]Andersson, J., Erck, R.A., Erdemir, A., 2003, "Friction of diamond-like carbon films in different atmospheres," Wear, **254**, 1070-1075.

[23]Sawyer, W.G. and Dickrell, P.L., 2004,"A fractional coverage model for gas-surface interaction in reciprocating sliding contacts," Wear, **256**, pp. 73-80.

[24]Kopta, S. and Salmeron, M., 2000,"The atomic scale origin of wear on mica and its contribution to friction," Journal of Chemical Physics, **113**, pp. 8249-8252.

[25]Dickinson, J.T., Park, N-S., Kim, M-W., Langford, S.C., 1997,"A scanning force microscope study of a tribochemical system: stress-enhanced dissolution," Tribology Letters, **3**, pp. 69-80.

[26]Donnet, C., 1998,"Recent progress on the tribology of doped diamond-like and carbon alloy coatings: A review," Surface & Coatings Technology, **101**, pp. 180-186.

[27]Scharf, T.W. and Singer, I.L., 2002,"Role of third bodies in friction behavior of diamond-like nanocomposite coatings studied by in situ tribometry," Tribology Transactions, **45**, pp. 363-371.

[28]Sanchez-Lopez, J.C., Erdemir, A., Donnet, C., and Rojas, T.C., 2003,"Friction-induced structural transformations of diamondlike carbon coatings under various atmospheres," Surface & Coatings Technology, **163**, pp. 444-450.

[29]Donnet, C., Le Mogne, T., Ponsonnet, L., Belin, M., Grill, A., Patel, V., and Jahnes, C., 1998,"The respective role of oxygen and water vapor on the tribology of hydrogenated diamond-like carbon coatings," Tribology Letters, **4**, pp. 259-265.

[30] *Guide to the expression of uncertainty in measurement*, 1993, International Standards Organization (ISO)

[31] Taylor, B.N. and Kuyatt, C.E., Guidelines for Evaluating and Expressing the Uncertainty of NIST Measurement Results. in NIST Technical Note 1297, 1994.

[32] Schmitz, T.L., Action, J.E., Burris, D.L., Ziegert, J.C., Sawyer, W.G., 2004, "Wear-Rate Uncertainty Analysis," Trans. of the ASME Journal of Tribology, **126**, pp. 802-808.

[33] Schmitz, T.L., Action, J.E., Ziegert, J.C., Sawyer, W.G, 2005, "The Difficulty of Measuring Low Friction: Uncertainty Analysis for Friction Coefficient Measurements," Trans. of the ASME Journal of Tribology, **127**,pp.673-678.

[34] E. Oberg, F.D. Jones, H.L. Horton , *Machinery's Handbook 23*, pg 632, milling and turning ANSI tolerance, Industrial Press, 1990, New York.

[35] Johnson, J.A., Woodford, J.B., Erdemir, A., Fenske, G.R., 2003, "Near-Surface Characterization of Amorphous Carbon Films by Neutron Reflectivity," Applied Physics Letters, **83**, pp. 452-454.

[36] Hudson, J.B., 1998, *Surface Science: an introduction* , Wiley, New York.

[37] Biener, J., Lang, E., Lutterloh, C., Kuppers, J., 2002, "Reactions of Gas-Phase H Atoms With Atomically and Molecularly Adsorbed Oxygen on Pt(111)," Journal of Chemical Physics, **116**, pp. 3063-3074.

BIOGRAPHICAL SKETCH

Pamela Laurie Frysz was born on March 11, 1979, in Buffalo, NY, to Clementina Carmella Matteliano and Raymond John Frysz. She has one older sister, Monica Nannis. Pamela grew up in Tampa, FL, and later moved to Brandon, FL, with her mother and stepfather, Carl Ellis McLean, where she graduated from Bloomingdale High School in June 1996. Pamela received her Bachelor of Science in mechanical engineering from the University of Florida in December of 2000. She was married to Daniel John Dickrell III on December 22, 2002. She received her Master of Science in mechanical engineering from the University of Florida in December of 2003. She will receive her Doctorate of Philosophy in mechanical engineering in August of 2005.

Upon completion of her Ph.D. Pamela will be heading any way the wind blows.

I certify that I have read this study and that in my opinion it conforms to acceptable standards of scholarly presentation and is fully adequate, in scope and quality, as a dissertation for the degree of Doctor of Philosophy.

W. G. Sawyer

Wallace Gregory Sawyer, Chairman
Assistant Professor of Mechanical and Aerospace Engineering

I certify that I have read this study and that in my opinion it conforms to acceptable standards of scholarly presentation and is fully adequate, in scope and quality, as a dissertation for the degree of Doctor of Philosophy.

D. W. Hahn

David W. Hahn
Associate Professor of Mechanical and Aerospace Engineering

I certify that I have read this study and that in my opinion it conforms to acceptable standards of scholarly presentation and is fully adequate, in scope and quality, as a dissertation for the degree of Doctor of Philosophy.

Tony L. Schmitz

Tony L. Schmitz
Assistant Professor of Mechanical and Aerospace Engineering

I certify that I have read this study and that in my opinion it conforms to acceptable standards of scholarly presentation and is fully adequate, in scope and quality, as a dissertation for the degree of Doctor of Philosophy.

John C. Ziegert

John C. Ziegert
Professor of Mechanical and Aerospace Engineering

I certify that I have read this study and that in my opinion it conforms to acceptable standards of scholarly presentation and is fully adequate, in scope and quality, as a dissertation for the degree of Doctor of Philosophy.

Paul Holloway

Paul H. Holloway
Distinguished Professor of Materials Science and Engineering

This dissertation was submitted to the Graduate Faculty of the College of Engineering and to the Graduate School and was accepted as partial fulfillment of the requirements for the degree of Doctor of Philosophy.

August, 2005

Pramod P. Khargonekar
Dean, College of Engineering

Kenneth Gerhardt
Dean, Graduate School

LD
1780
2005
.D553

UNIVERSITY OF FLORIDA
3 1262 08554 2560